

Search for Supersymmetry at the LHC in events with jets and missing energy using the α_T variable



Chris Lucas

School of Physics
University of Bristol

This dissertation is submitted for the degree of
Doctor of Philosophy

May 2015

Abstract

A search for Supersymmetry in the jets and missing energy final state is described using the CMS detector at the LHC, and the full 19.7 fb^{-1} dataset of $\sqrt{s} = 8 \text{ TeV}$ proton-proton collisions. The search makes use of the novel kinematic variable, α_T , to reduce contributions from QCD multijet processes by many orders of magnitude, down to a negligible level. Remaining background sources originate from electroweak decays of heavy bosons, and are estimated using a data-driven technique employing dedicated control regions. To maintain sensitivity to a broad range of potential Supersymmetric manifestations, the analysis categorises events in dimensions of H_T , n_{jet} and n_b . No statistically significant excess is observed and as such the results are interpreted within the context of decays of stop particles, specifically those relevant in the mass-degenerate region of Supersymmetric phase space.

Table of contents

Table of contents	5
List of figures	9
List of tables	17
Nomenclature	19
1 Introduction	21
2 Theory	25
2.1 Introduction	25
2.2 The Standard Model	25
2.2.1 Failings of the Standard Model	26
2.3 Overview of Supersymmetry	28
2.3.1 Why SUSY?	29
2.3.2 Experimental Consequences	30
2.3.3 Simplified Model Spectra	30
2.3.4 Mass-degeneracy in SUSY	31
3 The LHC and the CMS Detector	35
3.1 The Large Hadron Collider	35
3.2 Compact Muon Solenoid	37
3.3 Detector Subsystems	40
3.3.1 Tracker	40
3.3.2 Electromagenetic Calorimeter	40
3.3.3 Hadronic Calorimeter	41
3.3.4 Muon Systems	41

3.4 Trigger and Data Acquisition	42
3.4.1 Trigger system	42
4 Object Definitions	45
4.1 Introduction	45
4.2 Jets	45
4.2.1 Tagging jets from b-quarks	46
4.3 Muons	47
4.4 Photons	47
4.5 Electrons	48
4.6 Energy Sums	49
4.7 Single Isolated Tracks	50
5 Datasets and MonteCarlo samples	51
5.1 Datasets	51
5.2 MonteCarlo Background and Signal samples	51
5.3 Correcting SM sample cross sections	57
5.3.1 H_T^{parton} binned samples	57
5.3.2 HT side-band normalisation	58
6 The α_T Analysis	59
6.1 Analysis Overview	59
6.1.1 The α_T kinematic variable	59
6.2 Standard Model Backgrounds	62
6.2.1 Genuine \cancel{E}_T	62
6.2.2 Fake \cancel{E}_T	63
6.3 Signal Triggers	64
6.4 Selection Criteria	65
6.5 Residual QCD cleaning	69
6.5.1 Multiple jets below threshold	69
6.5.2 Instrumental effects	69
6.5.3 Heavy-flavour jet decays	71
6.6 Predicting high- n_b event yields	73
6.7 Example distributions and cutflow	75

Table of contents

7

7 Background Estimation	77
7.1 Overview of Electroweak background prediction method	77
7.2 Control samples	79
7.2.1 μ +jets	80
7.2.2 $\mu\mu$ +jets	82
7.2.3 γ +jets	83
7.3 Background control and systematic uncertainties on SM background predictions	85
7.3.1 Closure tests	85
7.3.2 Background systematic uncertainty summary	88
8 Results	91
8.1 Likelihood Model	91
8.1.1 Hadronic Signal Region	91
8.1.2 Electroweak Background Contribution	91
8.1.3 Signal Contribution	93
8.1.4 Total Likelihood	94
8.2 Fit Results	94
8.2.1 Fit without Signal region	95
8.2.2 Fit with Signal region	97
8.2.3 Pulls and p-values	99
9 Interpretation	117
9.1 Signal Acceptance	117
9.1.1 T2cc	117
9.1.2 T2_4body	120
9.1.3 ISR Corrections to compressed spectra MC signal samples . . .	120
9.2 Systematic Uncertainties on Signal Acceptance	123
9.2.1 Jet energy scale	123
9.2.2 Initial State Radiation	124
9.2.3 Btag scale factors	125
9.2.4 PDF	125
9.2.5 H_T/\mathbb{E}_T cleaning cut	126
9.2.6 Dead ECAL Filter	126
9.2.7 Generator Level Partons	127
9.2.8 Luminosity Measurement	128

9.2.9	Summary	128
9.3	Limits on models of Supersymmetry	129
9.3.1	Overview of limit setting procedure	129
9.3.2	Limits	130
9.4	Interpretation of excesses	131
10	Conclusion	133
10.1	Conclusion	133
References		135
Appendix A	Signal Model Systematics Plots	141
Appendix B	$\Delta\phi_{min}^*$ requirement in the signal region	157
B.1	Simulation	157
B.2	Effect on signal models	157

List of figures

2.1	Quantum self-corrections to the Higgs mass from a fermionic top quark loop.	28
2.2	Quantum self-corrections to the Higgs mass from a bosonic stop loop.	29
2.3	Feynman diagrams of the two SMS models considered.	32
2.4	Distributions of the generator level quarks produced in the two-body (left) and four-body (right) decays, prior to any event selection.	32
2.5	Current limits on direct stop production from the CMS (2.5a)[1] and ATLAS (2.5b)[2] experiments as a function of the $m_{\tilde{t}}$ vs. $m_{\tilde{\chi}^0}$ mass plane.	33
3.1	Schematic diagram of the CERN accelerator complex, showing the various accelerators and storage rings, ultimately feeding the Large Hadron Collider.	36
3.2	Schematic diagram of the Large Hadron Collider, indicating the positions of the four collision points and their corresponding detector experiments.	36
3.3	The peak instantaneous luminosity for each day throughout 2012 (a), and the integrated luminosity delivered to and recorded at CMS (b) from [3].	37
3.4	The average Pileup distribution as seen by the CMS detector throughout Run I, taken from [3].	38
3.5	Diagram of the Compact Muon Solenoid taken from [4].	39
3.6	Cross section of the CMS detector in the y - z plane, showing the three muon systems as well as other interior sub-detector systems.	42
3.7	Schematic overview of the Level-1 hardware trigger system of CMS. η coverage is shown in red and the data-flow indicated by arrow direction.	43

4.1	The Combined Secondary Vertex b-tagging algorithm discriminator distribution (left) and the b-tagging efficiency (right) as measured in both data and simulation. MC scale factors are shown in the lower plot of 4.1b.	46
5.1	Generator level H_T^{parton} distributions from the inclusive DY + jets and the H_T^{parton} binned Z($\nu\nu$) + jets samples.	57
6.1	Plots showing the correlation between \mathbb{H}_T and ΔH_T for QCD, $Z \rightarrow \nu\bar{\nu}$ and an example SUSY signature T2cc ($m_{\tilde{t}} = 250$ GeV, $m_{\tilde{\chi}^0} = 240$ GeV). Contours of constant α_T are shown in black. Each axis is normalised according to the event H_T <i>show all three?</i>	61
6.2	The correlation between H_T and \mathbb{H}_T for different α_T values, with the assumption of $\Delta H_T = 0$	62
6.3	The breakdown of the total electroweak background into component processes as a function of n_{jet} and n_b , for $H_T > 200$ GeV.	63
6.4	Differential (left) and Cumulative (right) efficiency turn-on curves for the signal triggers, for the three lowest H_T bins and $2 \leq n_{jet} \leq 3$	67
6.5	Differential (left) and Cumulative (right) efficiency turn-on curves for the signal triggers, for the three lowest H_T bins and $n_{jet} \geq 4$	68
6.6	The $\mathbb{H}_T/\mathbb{E}_T$ distribution of MC events following the hadronic selection criteria, minus the $\mathbb{H}_T/\mathbb{E}_T$ requirement. The MC yields are stacked, with the QCD contribution shown in cyan. The plot is for a fully inclusive selection of $n_b \geq 0$, $n_{jet} \geq 2$ and $H_T > 200$ GeV.	70
6.7	Distribution of jets in (η, ϕ) -space that are responsible for an event satisfying the requirement $\Delta\phi^* < 0.3$, with (a,b) and without (c,d) the “dead ECAL filter” requirement applied as part of the signal region selection.	71
6.8	Data (black points) against the EWK background prediction (stacked, yellow and purple) as a function of $\Delta\phi_{min}^*$. The expected yield from QCD MC (cyan) is stacked on top of the EWK prediction. The plot represents the QCD control study region, with $n_b \geq 0$, $n_{jet} \geq 2$, $H_T > 775$ GeV and $\alpha_T > 0.507$	73

6.9	The α_T distribution for events with no $\Delta\phi^*$ requirement (red circles) and with the $\Delta\phi^* > 0.3$ requirement (blue circles) as determined from QCD multijet simulation (left column) or data (right column) and the exclusive $n_{\text{jet}} = 3$ (top row) or $n_{\text{jet}} = 4$ (bottom row). The QCD control study region requirements have been applied, $H_T > 775$ GeV and $\alpha_T > 0.507$, with $n_b \geq 0$	74
6.10	MC distributions for the full hadronic signal selection. The sum of the individual sample contributions is shown in green. Plots are for $H_T > 200$ GeV, $n_{\text{jet}} \geq 2, n_b \geq 0$	76
7.1	Comparison of data with MC for the $\mu+\text{jets}$ control selection. Plots are for $H_T > 200$ GeV, $n_{\text{jet}} \geq 2, n_b \geq 0$	81
7.2	Comparison of data with MC for the $\mu\mu+\text{jets}$ control selection. Plots are for $H_T > 200$ GeV, $n_{\text{jet}} \geq 2, n_b \geq 0$	83
7.3	Efficiency turn-on curves for the photon trigger, based on the $\gamma+\text{jets}$ selection, for $H_T > 375$ GeV, with $2 \leq n_{\text{jet}} \leq 3$ (Left) and $n_{\text{jet}} \geq 4$ (Right).	84
7.4	Comparison of data with MC for the $\gamma+\text{jets}$ control selection. Plot is for $H_T > 200$ GeV, $n_{\text{jet}} \geq 2, n_b \geq 0$	84
7.5	The results of the eight core closure tests (open symbols), shown over the systematic uncertainty bands for each of the five H_T regions (shaded grey), for the two jet multiplicity regions (a) $2 \leq n_{\text{jet}} \leq 3$ and (b) $n_{\text{jet}} \geq 4$ separately.	86
7.6	The results of the eight core closure tests (open symbols), shown over the systematic uncertainty bands for each of the five H_T regions (shaded grey), for the two jet multiplicity regions (a) $2 \leq n_{\text{jet}} \leq 3$ and (b) $n_{\text{jet}} \geq 4$ separately. Included are zeroeth order (left column, blue) and first order (right column, red) fits to each individual closure test.	88
8.1	Pulls and pvalues	99
8.2	Observations in data for the various signal and control regions in the analysis, compared to the result of the full likelihood model simultaneous fit, when the hadronic data observations are not considered. The plots are for the $2 \leq n_{\text{jet}} \leq 3, n_b = 0$ analysis category.	101

8.3	Observations in data for the various signal and control regions in the analysis, compared to the result of the full likelihood model simultaneous fit, when the hadronic data observations are not considered. The plots are for the $2 \leq n_{\text{jet}} \leq 3, n_b = 1$ analysis category.	102
8.4	Observations in data for the various signal and control regions in the analysis, compared to the result of the full likelihood model simultaneous fit, when the hadronic data observations are not considered. The plots are for the $2 \leq n_{\text{jet}} \leq 3, n_b = 2$ analysis category.	103
8.5	Observations in data for the various signal and control regions in the analysis, compared to the result of the full likelihood model simultaneous fit, when the hadronic data observations are not considered. The plots are for the $n_{\text{jet}} \geq 4, n_b = 0$ analysis category.	104
8.6	Observations in data for the various signal and control regions in the analysis, compared to the result of the full likelihood model simultaneous fit, when the hadronic data observations are not considered. The plots are for the $n_{\text{jet}} \geq 4, n_b = 1$ analysis category.	105
8.7	Observations in data for the various signal and control regions in the analysis, compared to the result of the full likelihood model simultaneous fit, when the hadronic data observations are not considered. The plots are for the $n_{\text{jet}} \geq 4, n_b = 2$ analysis category.	106
8.8	Observations in data for the various signal and control regions in the analysis, compared to the result of the full likelihood model simultaneous fit, when the hadronic data observations are not considered. The plots are for the $n_{\text{jet}} \geq 4, n_b = 3$ analysis category.	107
8.9	Observations in data for the various signal and control regions in the analysis, compared to the result of the full likelihood model simultaneous fit, when the hadronic data observations are not considered. The plots are for the $n_{\text{jet}} \geq 4, n_b \geq 4$ analysis category.	108
8.10	Observations in data for the various signal and control regions in the analysis, compared to the result of the full likelihood model simultaneous fit. The plots are for the $2 \leq n_{\text{jet}} \leq 3, n_b = 0$ analysis category. . .	109
8.11	Observations in data for the various signal and control regions in the analysis, compared to the result of the full likelihood model simultaneous fit. The plots are for the $2 \leq n_{\text{jet}} \leq 3, n_b = 1$ analysis category. . .	110

8.12	Observations in data for the various signal and control regions in the analysis, compared to the result of the full likelihood model simultaneous fit. The plots are for the $2 \leq n_{\text{jet}} \leq 3, n_b = 2$ analysis category.	111
8.13	Observations in data for the various signal and control regions in the analysis, compared to the result of the full likelihood model simultaneous fit. The plots are for the $n_{\text{jet}} \geq 4, n_b = 0$ analysis category.	112
8.14	Observations in data for the various signal and control regions in the analysis, compared to the result of the full likelihood model simultaneous fit. The plots are for the $n_{\text{jet}} \geq 4, n_b = 1$ analysis category.	113
8.15	Observations in data for the various signal and control regions in the analysis, compared to the result of the full likelihood model simultaneous fit. The plots are for the $n_{\text{jet}} \geq 4, n_b = 2$ analysis category.	114
8.16	Observations in data for the various signal and control regions in the analysis, compared to the result of the full likelihood model simultaneous fit. The plots are for the $n_{\text{jet}} \geq 4, n_b = 3$ analysis category.	115
8.17	Observations in data for the various signal and control regions in the analysis, compared to the result of the full likelihood model simultaneous fit. The plots are for the $n_{\text{jet}} \geq 4, n_b \geq 4$ analysis category.	116
9.1	Signal efficiency times acceptance of the $\text{pp} \rightarrow \widetilde{t}\widetilde{t}^* \rightarrow c\widetilde{\chi}^0 \bar{c}\widetilde{\chi}^0$ simplified model, for the hadronic selection (left) and the $\mu+\text{jets}$ selection (right), shown for the four most sensitive analysis categories with an inclusive selection on H_T	119
9.2	Data to MC comparisons for an enriched $Z \rightarrow l\bar{l}$ selection, with the vectorial sum of lepton p_T 's (left) and of the recoil jets (right) [5].	121
9.3	Signal efficiency times acceptance of the $\text{pp} \rightarrow \widetilde{t}\widetilde{t}^* \rightarrow bff'\widetilde{\chi}^0 bff'\widetilde{\chi}^0$ simplified model, for the hadronic selection (left) and the $\mu+\text{jets}$ selection (right), shown for the four most sensitive analysis categories with an inclusive selection on H_T	122
9.4	The expected limit (red dashed line) with central band (thick red) and $\pm 1\sigma$ and $\pm 2\sigma$ uncertainty bands (thin red), and the observed limit (thick black) for the T2cc model. The limit is calculated with an include $H_T > 200$ GeV selection, and the analysis categories ($n_b = 0, 2 \leq n_{\text{jet}} \leq 3$), ($n_b = 1, 2 \leq n_{\text{jet}} \leq 3$), ($n_b = 0, n_{\text{jet}} \geq 4$), ($n_b = 1, n_{\text{jet}} \geq 4$)	130

9.5	The expected limit (red dashed line) with central band (thick red) and $\pm 1\sigma$ and $\pm 2\sigma$ uncertainty bands (thin red), and the observed limit (thick black) for the <code>T2degen</code> model. The limit is calculated with an include $H_T > 200$ GeV selection, and the analysis categories ($n_b = 0, 2 \leq n_{jet} \leq 3$), ($n_b = 1, 2 \leq n_{jet} \leq 3$), ($n_b = 0, n_{jet} \geq 4$), ($n_b = 1, n_{jet} \geq 4$) . . .	131
A.1	The relative change in acceptance times signal efficiency for the <code>T2cc</code> model for downwards (left) and upwards (middle) fluctuations of all jet energies by the uncertainty of the jet energy scale, and the derived systematic values (right). Each set of plots corresponds to one of the four most sensitive analysis categories (n_b, n_{jet}), with the inclusive requirement $H_T > 200$ GeV.	142
A.2	PDF uncertainties as a function of the <code>T2cc</code> scan plane, calcualted using a PDF4LHC ‘envelope’ calculation to determine a central band (A.2b), and $\pm 1\sigma$ variations (A.2a and A.2c). Plots are a for a fully inclusive selection on H_T , n_{jet} and n_b	143
A.3	The relative change in acceptance times signal efficiency for the <code>T2cc</code> model for downwards (left) and upwards (middle) fluctuations of the global event weight equal to the magnitude of the ISR corrections, and the derived systematic values (right). Each set of plots corresponds to one of the four most sensitive analysis categories (n_b, n_{jet}), with the inclusive requirement $H_T > 200$ GeV.	144
A.4	The relative change in acceptance times signal efficiency for the <code>T2cc</code> model for downwards (left) and upwards (middle) fluctuations of global event weight according to the uncertainties of the Btag scale factors, and the derived systematic values (right). Each set of plots corresponds to one of the four most sensitive analysis categories (n_b, n_{jet}), with the inclusive requirement $H_T > 200$ GeV.	145
A.5	The acceptance of the $\mathcal{H}_T/\mathcal{E}_T$ cut as a function of the <code>T2cc</code> mass plane. Each plot represents one of the four most sensitive analysis cateogires (n_b, n_{jet}), with the inclusive requirement $H_T > 200$ GeV.	146
A.6	The acceptance of the DeadECAL cut as a function of the <code>T2cc</code> mass plane. Each plot represents one of the four most sensitive analysis cateogires (n_b, n_{jet}), with the inclusive requirement $H_T > 200$ GeV.	147

A.7 The total systematic uncertainty as a function of the T2cc scan plane, where all individual systematic contributions are summed in quadrature. Each plot represents one of the four most sensitive analysis categories (n_b , n_{jet}), with the inclusive requirement $H_T > 200$ GeV.	148
A.8 The relative change in acceptance times signal efficiency for the T2Degen model for downwards (left) and upwards (middle) fluctuations of all jet energies by the uncertainty of the jet energy scale, and the derived systematic values (right). Each set of plots corresponds to one of the four most sensitive analysis categories (n_b , n_{jet}), with the inclusive requirement $H_T > 200$ GeV.	150
A.9 The relative change in acceptance times signal efficiency for the T2Degen model for downwards (left) and upwards (middle) fluctuations of the global event weight equal to the magnitude of the ISR corrections, and the derived systematic values (right). Each set of plots corresponds to one of the four most sensitive analysis categories (n_b , n_{jet}), with the inclusive requirement $H_T > 200$ GeV.	151
A.10 The relative change in acceptance times signal efficiency for the T2Degen model for downwards (left) and upwards (middle) fluctuations of global event weight according to the uncertainties of the Btag scale factors, and the derived systematic values (right). Each set of plots corresponds to one of the four most sensitive analysis categories (n_b , n_{jet}), with the inclusive requirement $H_T > 200$ GeV.	152
A.11 The acceptance of the $\cancel{H}_T/\cancel{E}_T$ cut as a function of the T2degen mass plane. Each plot represents one of the four most sensitive analysis categories (n_b , n_{jet}), with the inclusive requirement $H_T > 200$ GeV.	153
A.12 The acceptance of the DeadECAL cut as a function of the T2Degen mass plane. Each plot represents one of the four most sensitive analysis categories (n_b , n_{jet}), with the inclusive requirement $H_T > 200$ GeV.	154
A.13 The total systematic uncertainty as a function of the T2Degen scan plane, where all individual systematic contributions are summed in quadrature. Each plot represents one of the four most sensitive analysis categories (n_b , n_{jet}), with the inclusive requirement $H_T > 200$ GeV.	155

B.1	The change in acceptance of the <code>T2cc</code> model when applying the $\Delta\phi_{min}^*$ > 0.3 requirement. Plots are shown for the four relevant categories used for interpretation, with an inclusive selection of $H_T > 200$ GeV	158
B.2	The change in acceptance of the <code>T2degen</code> model when applying the $\Delta\phi_{min}^* > 0.3$ requirement. Plots are shown for the four relevant categories used for interpretation, with an inclusive selection of $H_T > 200$ GeV	159
B.3	An event display of a typical heavy flavour QCD event, with a jet decaying leptonically with high- p_T neutrinos and therefore considerable generator-level \cancel{E}_T	160

List of tables

4.1	Criteria for the “loose” jet ID working point.	46
4.2	Muon identification (Tight working point).	47
4.3	Photon identification (Tight working point).	48
4.4	Electron identification (Loose working point).	48
4.5	\cancel{E}_T filters employed in the analysis, as recommended by the MET <i>POG</i>	49
4.6	Single Isolated Track identification.	50
5.1	8 TeV Datasets.	51
5.2	MC samples for Standard Model processes.	54
5.3	MC samples for Simplified Model Spectra.	56
5.4	Correction factors determined as the ratio of yields in data to those in MC, for a sideband region of $150 < H_T < 200$ GeV. Factors are calculated for process-specific MC samples by choosing a selection enriched in the relevant process, and applied as a global correction.	58
6.1	H_T bin lower bounds used for each n_{jet} and n_b category.	60
6.2	Signal triggers, the L1 seed triggers and their efficiencies measured for per H_T and n_{jet} category.	64
6.3	Jet E_T thresholds per H_T bin.	66
6.4	The cutflow of the hadronic selection in data. The subscript ‘fail’ indicates an object which did not meet all ID requirements, and so is not considered as a ‘common object’. The event selection follows an inclusive selection in data of $H_T > 375$ GeV, $n_{\text{jet}} \geq 2$ and $n_b \geq 0$	75
7.1	The control samples used to produce SM background predictions for each analysis category (n_b , n_{jet}).	79
7.2	Muon trigger efficiencies (%) for the μ +jets selection listed by H_T bin and n_{jet} category.	81

7.3	Muon trigger efficiencies (%) for the $\mu\mu + \text{jets}$ selection listed by H_T bin and n_{jet} category.	82
7.4	Results of zeroeth (i.e. constant) and first order (i.e. linear) fits for five sets of closure tests, performed in the $2 \leq n_{\text{jet}} \leq 3$ category.	87
7.5	Results of zeroeth (i.e. constant) and first order (i.e. linear) fits for five sets of closure tests, performed in the $2 \leq n_{\text{jet}} \leq 3$ category.	87
7.6	Results of zeroeth (i.e. constant) and first order (i.e. linear) fits for the three sets of closure tests probing the accuracy of jet multiplicity modelling in MC, for each control sample.	88
7.7	Summary of the magnitude of systematic uncertainties (%) derived from the eight core closure tests, for each n_{jet} category and H_T region.	89
8.1	Summary of likelihood nuisance parameters.	94
8.2	Summary of the “a posteriori” fit.	96
8.3	Summary of the “a priori” fit.	98
9.1	Cutflow table for two mass points ($m_{\tilde{t}} = 250$ GeV, $m_{\tilde{\chi}^0} = 240$ GeV and $m_{\tilde{t}} = 250$ GeV, $m_{\tilde{\chi}^0} = 170$ GeV) of the T2cc signal model. The selection represents the hadronic signal region for the $H_T > 375$ GeV region.	118
9.2	Cutflow table for two mass points ($m_{\tilde{t}} = 250$ GeV, $m_{\tilde{\chi}^0} = 240$ GeV and $m_{\tilde{t}} = 250$ GeV, $m_{\tilde{\chi}^0} = 170$ GeV) of the T2Degen signal model. The selection represents the hadronic signal region for the $H_T > 375$ GeV region.	121
9.3	Correction factors for MADGRAPH based signal samples to account for MC over-prediction of ISR.	123
9.4	Systematic factors for MADGRAPH based signal samples to determine ISR modelling related systematics.	124
9.5	Efficiencies of the H_T/\cancel{E}_T requirement cut for the $\mu + \text{jets}$ selection in data ϵ_{data} and MC ϵ_{MC} , as well as the ratio of both. Efficiencies are shown for the two n_{jet} categories and the four lowest H_T bins, with an inclusive requirements are made of n_b	126
9.6	Efficiencies of the dead ECAL cut for the $\mu + \text{jets}$ selection in data ϵ_{data} and MC ϵ_{MC} , as well as the ratio of both. Efficiencies are shown for the two n_{jet} categories and the four lowest H_T bins, with an inclusive requirements are made of n_b	127

9.7	Relative change in efficiency times acceptance for the 2-parton and 3-parton scans in the signal region, with an inclusive selection on n_b and $H_T > 200$ GeV. The scan points are $m_{\tilde{t}} = 200$ GeV and $m_{\tilde{\chi}^0} = (120, 190)$ GeV.	128
9.8	Representative ranges for each contribution to the total systematic uncertainty on the signal efficiency times acceptance for each relevant event category for the T2cc interpretation.	128
9.9	Representative ranges for each contribution to the total systematic uncertainty on the signal efficiency times acceptance for each relevant event category for the T2Degen interpretation.	129

Chapter 1

Introduction

Our instinctive method of understanding is reductive - the typical image of a young inventor attempting to make sense of the things around them, is that of endless toasters, clocks radios, or even gearboxes broken down into their smallest constituent parts to better understand what they're made of and, ultimately, what's happening inside of them. This simple idea translates perfectly to explain the work Particle Physicists have been undertaking with not simple everyday household objects, but the Universe.

Since the beginnings of the field, physicists have questioned what is around us, and what it's made of. From Fermi developing his ground-breaking model of the atom, to Rutherford discovering it's structure, the basic building blocks of the universe have been searched for. For Particle Physicists, this is the ultimate goal - a complete understanding of the nature of the Universe at it's most fundamental level. If a description can be written of the smallest possible building blocks of nature and how they interact, then ultimately we can understand the Universe from the ground up.

Currently, our best attempt comes from the intersection of two very different fields: Quantum Mechanics, the study of microscopic objects, and Relativity, the study of very fast objects. The combination of these two contrasting worlds gave birth to the field of Relativistic Quantum Mechanics, and ultimately, the Standard Model.

First proposed in the 1960s, the Standard Model attempts to describe the properties of the fundamental constituents of matter, and outline their interactions through three of the four fundamental forces of nature. Through it's accurate description and predictions of not only particles but also fundamental constants of nature, the Standard Model has exceptionally proven itself to be a triumph of modern physics.

Despite it's continued accuracy in the face of substantial scrutiny, however, the Standard Model fails to significant observations, for example the absent description

¹ of gravity and the ‘other’ 96% of particles in the Universe. As such, the SM is widely
² considered as a smaller component of some greater, all-encompassing theory. *talk more*
³ *of the problems of the standard model?* This belief has led many to use this distinct
⁴ theory as a building block, on which extensions can be introduced to create Beyond
⁵ the Standard Model (BSM) theories - the goal being to fix the gaps in knowledge left
⁶ by the SM.

⁷ Of the plethora of BSM theories, one particularly well motivated extension is Super-
⁸ symmetry (SUSY). The so-called ‘Supersymmetric’ extension to the Standard Model,
⁹ introducing supersymmetric particles (or ‘sparticles’), fixes many of the original the-
¹⁰ ories problems, most notably that of the Standard Models divergent Higgs Mass and,
¹¹ crucially, provides a strong candidate particle for the elusive Dark Matter observed in
¹² abundance in the Universe.

¹³ Particle physics as a field has developed largely via a cat and mouse game, played
¹⁴ out between theorists and experimentalists. While theoreticians have developed new
¹⁵ theories and new particles, experimentalists have raced to build greater and more
¹⁶ advanced experiments with which to test them, and vice-versa. Today, thanks to the
¹⁷ incredibly hard work of thousands of physicists, engineers and other professionals, we
¹⁸ are able to test such BSM theories with the Large Hadron Collider (LHC) in Geneva,
¹⁹ Switzerland.

²⁰ Using the LHC, we can reproduce the conditions observed a short time after the Big
²¹ Bang, where the incredibly high energies present were capable of producing countless
²² particles that wouldn’t be visible in todays universe. If such exotic particles are created
²³ in the proton-proton collisions performed at the LHC, it is the goal of experiments
²⁴ such as the Compact Muon Solenoid (CMS) to detect them.

²⁵ The CMS detector is comprised of multiple sub-detector systems, each designed
²⁶ specifically to make precise measurements of the characteristics of the different par-
²⁷ ticles created. The detector is built such that it provides almost complete hermetic
²⁸ coverage to detect particles travelling in all directions from the point of collision.
²⁹ Through the study of global momentum imbalances, the presence of weakly interact-
³⁰ ing particles can be inferred - a key technique for searches for SUSY.

³¹ If sparticles were to be produced at the LHC they would immediately decay to
³² many well-understood SM particles, and finally the weakly interacting ‘Lightest Su-
³³ persymmetric Particle’ (LSP), the theory’s Dark Matter candidate. *motivate why*
³⁴ *jets+MET is the best channel - high branching fractions? early discovery - blunt,*
³⁵ *quick, simple*

The work described in this thesis consists of such a search for SUSY particles
1
decaying to a jets and missing-energy final state. The biggest obstacle to searching for
2
hadronic signatures of new physics, is dealing with the huge (better word) hadronic
3
backgrounds from Quantum Chromodynamics (QCD). In this analysis a powerful
4
kinematic variable, α_T , is used to differentiate between QCD and potential signal
5
events. The remaining SM sources of background are estimated using a data-driven
6
transfer technique from dedicated control samples, orthogonal to the search region.
7

Given the vast number of potential manifestations of SUSY, many different forms
8
could theoretically be realised in nature. Accordingly, this analysis categorises events
9
into dimensions of three different event-level variables. Specific analysis categories can
10
therefore be used to produce targetted interpretations of different potential final states,
11
thereby maintaining a broad sensitivity to SUSY production, however it presents itself.
12
In this thesis, interpretations are shown for two different decay channels of the \tilde{t}
13
sparticle, and limits produced in terms of the \tilde{t} mass.
14

*intersection of cosmology (huge stuff) and us (tiny stuff) is becoming more and
15
more apparent.*
16

*little more here... We find ourselves in a historically familiar position in that,
17
thanks to the LHC, we are at the edge of the energy frontier, peering into the unknown.
18
Whatever we see, it's going to be exciting.*
19

Chapter 2

Theory

2.1 Introduction

The Standard Model (SM), proposed in 1960s, has long been the most prominent and successful description of fundamental particles and their interactions at the energies currently experimentally accessible. Its power has been proven with the theoretical prediction of particles such as the charm and top quarks, and the W and Z bosons, prior to their experimental observation. Furthermore, precision electroweak measurements have shown impressive levels of agreement with SM predictions [6].

However, despite it's great success, it is known to be valid only for low energies, and is missing significant details of both experimentally observed and theoretically predicted physical phenomena. As such, extensions to the SM have been extensively studied, assuming the SM to be the low-energy regime of some greater theory. One such strongly theoretically motivated extension to the SM is Supersymmetry (SUSY).

This chapter outlines the SM model, including it's particle content and basic mechanisms, before describing it's shortcomings - the theoretical motivation for theories Beyond the Standard Model (BSM). SUSY will then be introduced, before describing its simplest incarnations, along with a discussion of the specific models and frameworks used for interpretation within this analysis.

2.2 The Standard Model

The Standard Model is a renormalisable Quantum Field Theory describing fundamental matter particles and their interactions via the strong, weak and electromagnetic

¹ forces. It was collaboratively developed throughout the 1960s [7–11], with it’s current
² Lagrangian based formalism being finalised in the mid-1970s [12].

³ Requiring local gauge invariance of the SM Lagrangian, \mathcal{L}_{SM} , under transforma-
⁴ tions generated by universal space-time symmetry groups, interactions can be de-
⁵ scribed via conserved quantities. The $SU(3)$ group describes strong force interactions
⁶ via colour charge, and $SU(2)$ and $U(1)$ to describe electroweak interactions via weak
⁷ isospin and hypercharge respectively.

⁸ Matter particles are described by spin 1/2 fermions, divided into the six quarks and
⁹ six leptons. The quarks, are arrange into three generations: the up(u) and down(d),
¹⁰ the charm(c) and strange(s), and the top(t) and bottom(b), each couplet carrying
¹¹ individual electric charges of +2/3 and -1/2 respectively. The quarks also carry colour
¹² charge, where combinations of quarks form colour-neutral composite hadron particles
¹³ as seen in nature.

¹⁴ The leptons are similarly arranged into three generations, constructed from $SU(2)$
¹⁵ doublets of weak isospin, $(\nu_L, l)_L$, of left-handed chiral states, and singlets, l_R , of
¹⁶ right-handed chiral states, where l represents either the electron (e), muon (μ) or tau
¹⁷ (τ), each carrying a -1 electrical charge, and ν_L being their corresponding electrically
¹⁸ neutral neutrinos.

¹⁹ Interactions between the fermions are mediated by spin-1 bosons. The strong force,
²⁰ $SU(3)$, is represented by eight electrically neutral, massive gluons (g), each carrying
²¹ a colour charge. The electroweak force, $SU(2) \times U(1)$ is mediated by the electrically
²² neutral, massless photon (γ), the massive, neutral Z^0 , and the massive, electrically
²³ charged W^\pm bosons.

²⁴ Following the enforcement of local gauge invariance after an $SU(2) \times U(1)$ trans-
²⁵ formation, the bosonic mediator of the $U(1)$ symmetry, the γ , remains massless as
²⁶ expected, however so do the W^\pm and Z^0 , in disagreement with their experimentally
²⁷ observed masses. To remedy this, the $SU(2) \times U(1)$ symmetry undergoes Electroweak
²⁸ Symmetry Breaking (EWSB) via the Higgs Mechanism [13–15], leading to the Higgs,
²⁹ H^0 , a massive, electrically neutral, spin-0 scalar particle, thereby completing the for-
³⁰ malism of the Standard Model.

³¹ 2.2.1 Failings of the Standard Model

³² While the Standard Model has provided many accurate predictions and descriptions
³³ which have been extensively experimentally verified, the theory is considered incom-
³⁴ plete due to gaps in it’s description of the Universe.

The SM provides a QFT description of how the strong, weak and electromagnetic forces work on a quantum level, however it fails to include any description of the final fundamental force, gravity. A quantum description of gravity has long been sought after by particle theorists, in particular to provide an explanation for it's relative weakness at the EWK scale with respect to the other fundamental forces.

Following the Big Bang it is believed matter and anti-matter were created in equal amounts, however given that we exist in a matter dominated universe, there must exist some physical process by which an asymmetry came to be between the two types of matter - the so-called ‘Baryogenesis’ process. This could be described by violation of the Charge-Parity (CP) symmetry, however the amount of CP violation described by the Standard Model does not appear to be significant enough to achieve this REF.

In the SM, following the local gauge invariance requirement of the electroweak sector, $SU(2) \times U(1)$, the $SU(2)$ doublets contain massless neutrino particles. However, experimental observations of neutrino oscillation between their various flavours indicating them to have mass [16, 17], and therefore be mixing between different mass eigenstates. This is only described by extending the Standard Model to include neutrino mixing, described by the PMNS matrix [18].

Furthermore, and of particular relevance to the work in this thesis, are the Hierarchy Problem and the existence of Dark Matter - both of which will be described in further detail in the following sections.

The Hierarchy Problem

Particles couple to the Higgs field according to the Yukawa couplings, λ_f , proportionally to the mass of a the particle. For fermions, the Lagrangian interaction term is

$$\mathcal{L}_{\text{Yukawa}} = -\lambda_f \bar{\Psi} H \Psi, \quad (2.1)$$

where Ψ is a spin-1/2 Dirac field, and H the Higgs field. It can be shown that Higgs mass corrections due to beyond tree-level interactions with fermion fields (shown in figure 2.1) can be shown to be

$$\Delta m_H^2 \propto -|\lambda_f|^2 \Lambda_{\text{cut}}^2, \quad (2.2)$$

where Λ_{cut} is the cut-off energy scale, up to which the SM is valid, typically taken to be the Planck scale. This therefore leads to a quadratically divergent correction to m_H . Such corrections cause significant tension between the theoretically calculated

¹ value of m_H and the experimentally measured value, $m_H \simeq 125$ GeV [19, 20], requiring
² significant ‘fine-tuning’ to bring into agreement. This disagreement is known as the
³ Hierarchy Problem.

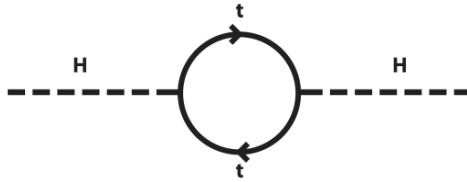


Fig. 2.1 Quantum self-corrections to the Higgs mass from a fermionic top quark loop.

⁴ Dark Matter

⁵ Significant amounts of so called ‘Dark Matter’ (DM) has been indirectly observed via
⁶ cosmological methods through the study of galaxy rotation curves and gravitational
⁷ lensing [21, 22]. For such a large relative abundance to be present, DM must be
⁸ massive and weakly interacting. No candidate particle exists in the SM to describe
⁹ such matter.

¹⁰ 2.3 Overview of Supersymmetry

¹¹ At its core, Supersymmetry is a new space-time symmetry between fermions and
¹² bosons [23–28] . An operator of SUSY acting on a fermion (resp. boson) state acts
¹³ to change the spin by a 1/2, producing a super-partner boson (resp. fermion) state,
¹⁴ maintaining electric charge, colour charge and weak isospin. A theory invariant under
¹⁵ such transformations is said to be supersymmetric.

¹⁶ As a consequence of this new symmetry, SUSY introduces a rich phenomenology
¹⁷ of new particles (sparticles). The simplest implementation of SUSY is the Minimally
¹⁸ Supersymmetric Standard Model (MSSM) [29] - a so-called ‘complete’ model, con-
¹⁹ taining 100 free-parameters representing sparticle masses, phases and mixing angles
²⁰ [30]. Within the MSSM, the SU(2) doublets and singlets, $(\nu_L, l)_L$ and l_R , have super-
²¹ partners $(\tilde{\nu}_L, \tilde{l})_L$ and \tilde{l}_R . Similarly for SU(3), $(q, q')_L$ and q_R , have super-partners
²² $(\tilde{q}_L, \tilde{q}')_L$ and \tilde{q}'_R . The spin-1 SM gauge bosons have spin-1/2 gaugino partners, the
²³ gluino, winos and bino, \tilde{g} , \tilde{W}^\pm , \tilde{W}^0 , \tilde{B}^0 . Following EWSB, five higgsinos remain,
²⁴ h^0 , H^0 , A^0 and H^\pm . Finally, the gauginos and the neutral higgsinos mix to give the

2.3 Overview of Supersymmetry

29

neutralinos, $\tilde{\chi}_{i=1-4}^0$, and the winos and charged higgsinos mix to give the charginos, $\tilde{\chi}_{i=1-2}^\pm$.

Given the lack of experimental evidence for SUSY, sparticles must have higher masses than their SM partners, implying that Supersymmetry is not an exact symmetry and therefore must be broken by some mechanism, of which many exist [31, 32].

2.3.1 Why SUSY?

The Supersymmetric extension to the SM provides solutions to many of the original theory's issues, for example the predicted unification of the running gauge couplings at higher energy scales. Arguably two of the most important described in the following two sections.

Hierarchy Problem

While in the SM the Higgs gains corrections to its mass from fermion-loop induced self-interactions, the presence of bosonic super-partners to these fermions in SUSY provides additional diagrams (figure 2.2), which contribute oppositely signed corrective terms,

$$\Delta m_H^2 \propto +\lambda_S \Lambda_{\text{cut}}^2 \quad (2.3)$$

where λ_S is bosonic super-partner's Yukawa coupling. The introduction of these super-partners, and therefore their additional corrective terms, provides an elegant solution to the hierarchy problem, where quadratic divergences to m_H are effectively cancelled by sparticle loop contributions.



Fig. 2.2 Quantum self-corrections to the Higgs mass from a bosonic stop loop.

Dark Matter

20

- ¹ In most supersymmetric theories, a new conserved quantum number R_P is introduced
² in order to conserve lepton and baryon number [33], defined as

$$\text{³} \quad R_P = (-1)^{3B+L+2s} \left(\begin{array}{c} = +1 \text{ for SM particles} \\ = -1 \text{ for SUSY particles} \end{array} \right) \quad (2.4)$$

- ⁴ where B is Baryon number, L is Lepton number and s is spin. SM particles have
⁵ $R_P = +1$, whereas SUSY particles have $R_P = -1$. R_P is a multiplicative quantum
⁶ number, therefore sparticles can only be pair-produced. The subsequent sparticle
⁷ decay will therefore consist of a cascade-type decay, with each sparticle decaying to
⁸ a final state containing a lighter, kinematically accessible sparticle. This process will
⁹ continue until the lightest supersymmetric particle (LSP) is reached, and is therefore
¹⁰ stable. It is the LSP that, within R-Parity conserving models, provides a stable,
¹¹ weakly interacting dark matter candidate [34].

¹² *WHAT IS ELECTROWEAK BARYOGENESIS?*

¹³ **2.3.2 Experimental Consequences**

- ¹⁴ In order for SUSY to provide an adequate solution to the hierarchy problem, sparticle
¹⁵ masses are required to be around the TeV scale [31, 32, 35]. This fact, coupled with
¹⁶ strong experimental bounds on constrained models and the discovery of the Higgs in a
¹⁷ compatible mass-region of the MSSM, have led interest towards ‘Natural’ SUSY mod-
¹⁸ els. Such models negate the limits imposed by experimental constraints by assuming
¹⁹ the first and second generation squarks to be very heavy, while the third generation be
²⁰ around 1 TeV in order to solve the hierarchy problem without significant fine-tuning
²¹ [36].

²² **2.3.3 Simplified Model Spectra**

- ²³ While ‘complete’ supersymmetric models offer a full description of all aspects of a
²⁴ given theory (e.g. mass spectra and mixing angles), the large number of free parame-
²⁵ ters becomes unmanageable for interpretations of experimental observations. Even in
²⁶ ‘compressed’ models, such as the Compressed-MSSM (CMSSM) with 5 free parameters
²⁷ [37], the interpretation phase-space is vast.

²⁸ In an effort to make interpretations of experimental data simpler for experimental-

²⁹ ists, while remaining universally of use to theorists, Simplified Model Spectra (SMS) models were developed [38, 39]. SMS models consist of simplified decay scenarios which can later be considered within complete models. Typically SMS models consist of either squark or gluino pair-production, with a subsequent decay to a given final state with a 100% branching fraction, effectively moving experimental searches away from ‘model-specific’ interpretations and towards more ‘signature-specific’ interpretations [40].

SMS models generally contain only two free parameters, normally the mass of a produced mother particle, m_{mother} , and the mass of the LSP, m_{LSP} . Therefore interpretations can be made over a simple 2-dimensional parameter space, making for trivial experimental comparisons.

SMS models prove to be an excellent tool for the interpretation of results within the bounds of naturalness. Many SMS models consider third generation squark production, allowing for direct limits to be placed on the dominant decays of stop and sbottom squarks.

2.3.4 Mass-degeneracy in SUSY

SUSY models with mass hierarchies spanning a small mass range are said to be ‘compressed’. When considered in terms of a simplified model scenario, this implies the pair-produced mother particle is close in mass to that of the LSP. The smaller the mass difference, Δm ($= m_{\text{mother}} - m_{LSP}$), the greater the experimental challenge, as visible decay products become softer and typically out of analysis acceptance.

In general, decay channels of the \tilde{t} are dominated by $\tilde{t} \rightarrow bW\tilde{\chi}^\pm$ and $\tilde{t} \rightarrow t\tilde{\chi}^0$. However, when $\Delta m < W$ -boson mass and a present W would become off-shell, \tilde{t} decay branching fractions become dominated by the two-body decay $\tilde{t} \rightarrow c\tilde{\chi}^0$, and the four-body decay $\tilde{t} \rightarrow bff'\tilde{\chi}^\pm$ [41]. In this region, these two decay channels can provide a dark-matter relic density consistent with cosmological observations (e.g. from WMAP [42]), where annihilation cross sections (*of what?*) are mediated by co-annihilation with the light stop proposed by naturalness [43, 44].

This analysis will therefore focus on the two \tilde{t} decays, relevant in this highly-compressed region of SUSY phase space, namely T2cc ($\text{pp} \rightarrow \tilde{t}\tilde{t}^* \rightarrow c\tilde{\chi}^0\bar{c}\tilde{\chi}^0$) and T2degen ($\text{pp} \rightarrow \tilde{t}\tilde{t}^* \rightarrow bff'\tilde{\chi}^0 bff'\tilde{\chi}^0$), shown in figure 2.3.

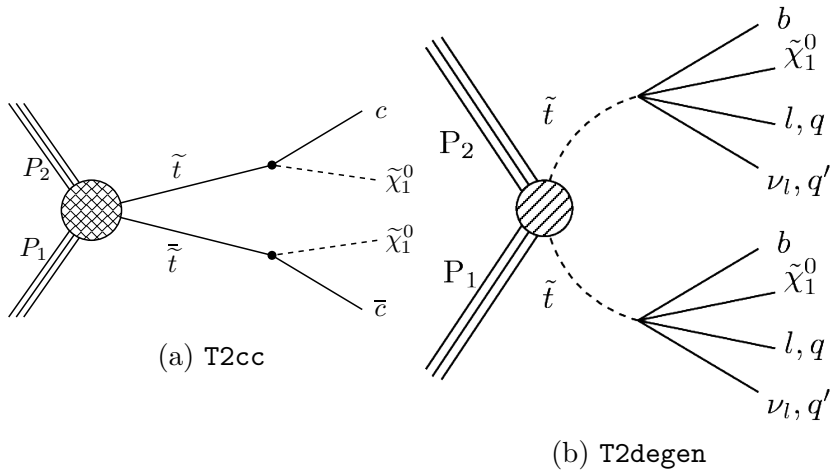


Fig. 2.3 Feynman diagrams of the two SMS models considered.

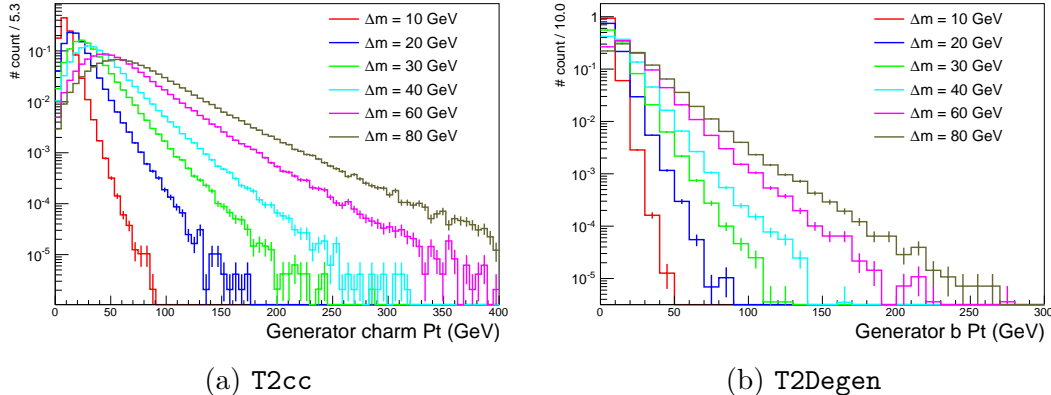


Fig. 2.4 Distributions of the generator level quarks produced in the two-body (left) and four-body (right) decays, prior to any event selection.

Phenomenology

31

- ¹ In the compressed region, characterised by small values of Δm , decay products of the
² \tilde{t} pair have very low momenta given the minimal amounts of energy available following
³ the production of the $\tilde{\chi}^0$. For example, figure 2.4a shows the transverse momentum
⁴ of the generator level charm quark originating from the decay of the \tilde{t} getting smaller
⁵ with decreasing values of Δm . The same observation is made for the p_T of the b-quark
⁶ present from the decay of the \tilde{t} in the 4-body decay, as shown in figure 2.4b.

The very low event kinematics of the small Δm region present considerable experimental challenges, and as such this region in the past has typically not been considered for interpretations. The acceptance of such models in this region is heavily reliant on

2.3 Overview of Supersymmetry

33

- ¹⁰ initial state particles radiated from the incoming partons, thereby boosting the soft SUSY decay system, as discussed later in chapter 9.

Current Experimental Limits

2

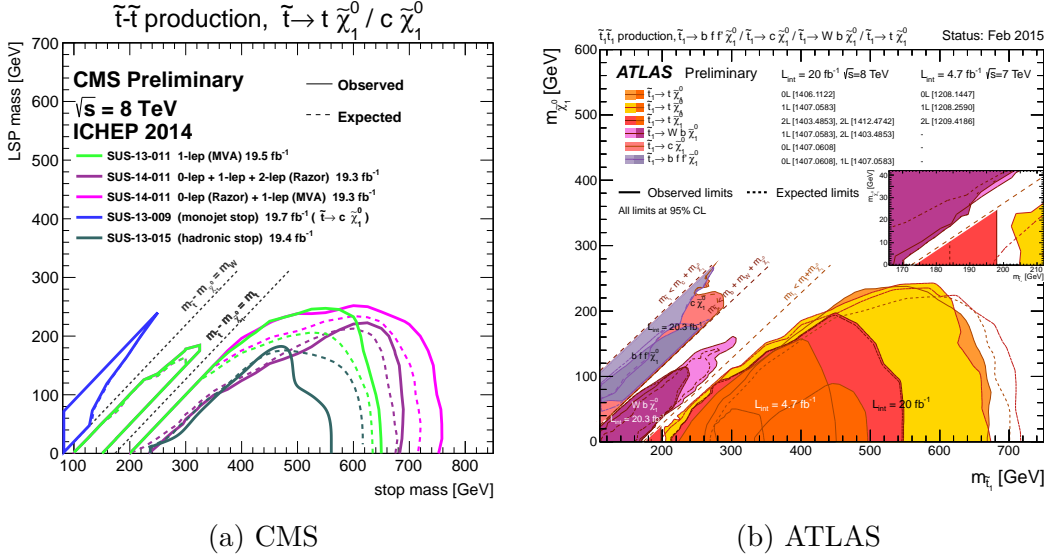


Fig. 2.5 Current limits on direct stop production from the CMS (2.5a)[1] and ATLAS (2.5b)[2] experiments as a function of the $m_{\tilde{t}}$ vs. $m_{\tilde{\chi}_1^0}$ mass plane.

Given the current lack of experimental evidence, limits for direct \tilde{t} production are shown in figure 2.5, with observed limits reaching up to $m_{\tilde{t}} = 275$ GeV for the charm decay, and a similar reach for the 4-body decay.

3

4

5

Chapter 3

The LHC and the CMS Detector

3.1 The Large Hadron Collider

The Large Hadron Collider (LHC) is a 27 km circumference proton-proton synchrotron with maximum design centre of mass energy of $\sqrt{s} = 14$ TeV, described in detail elsewhere [45]. It is the highest energy component of the CERN accelerator complex, which is shown in figure 3.1. The LHC accelerates counter-rotating beams of protons using 400 MHz radio frequency (RF) cavities, focusses the beam using multiple quadrupole and higher order magnets, and maintains the beam trajectory using superconducting, niobium-titanium dipole magnets, capable of producing an 8.4 T magnetic field. Such a high magnetic field is achieved by cooling the magnets to 1.9 K using super-fluid helium, and applying a 11.85 kA electric current.

The beams, consisting of approximately up to 1380 bunches of $\mathcal{O}(10^{11})$ protons, are brought into collision at four points around the LHC ring within specialised detector systems, as shown in figure 3.2. During the first run of the LHC, ‘Run I’, bunches were spaced in 50 ns intervals, giving a bunch crossing rate of 20 MHz. Collisions proceed for a number of hours, while collision rates are maintained by scanning the transverse beam positions, until such a time when proton numbers are depleted and the beam recycled so that the fill process can be repeated.

The rate of collisions at each interaction point is described by the instantaneous Luminosity, given by the equation:

$$L_{inst.} = \frac{f_{orbit} n_B N_p^2}{A_{eff}} \quad (3.1)$$

where f_{orbit} is the orbital frequency of bunches in the LHC, n_B is the number of

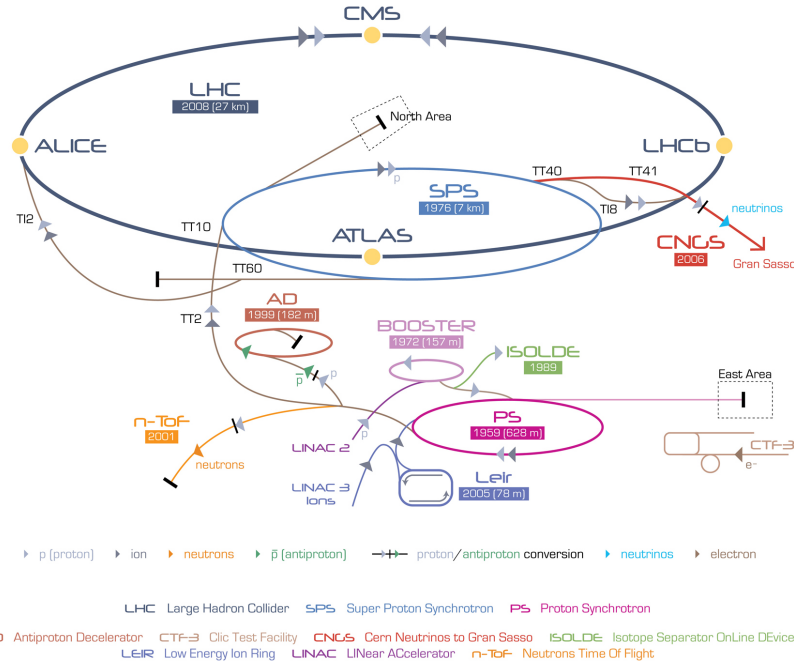


Fig. 3.1 Schematic diagram of the CERN accelerator complex, showing the various accelerators and storage rings, ultimately feeding the Large Hadron Collider.

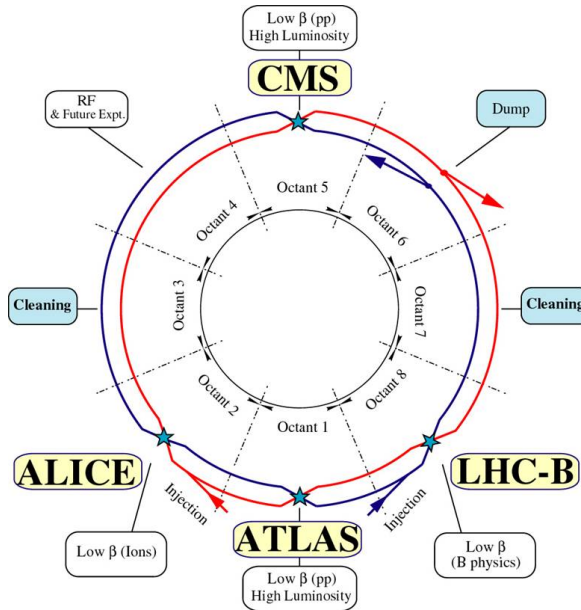


Fig. 3.2 Schematic diagram of the Large Hadron Collider, indicating the positions of the four collision points and their corresponding detector experiments.

bunches in the machine, N_p is the number of protons per bunch, and A_{eff} is the 23

3.2 Compact Muon Solenoid

¹ effective area overlap between colliding bunches. The peak L_{inst} per day for CMS is shown in figure 3.3a and the integral over time is shown in figure 3.3, both for the full run period throughout 2012.

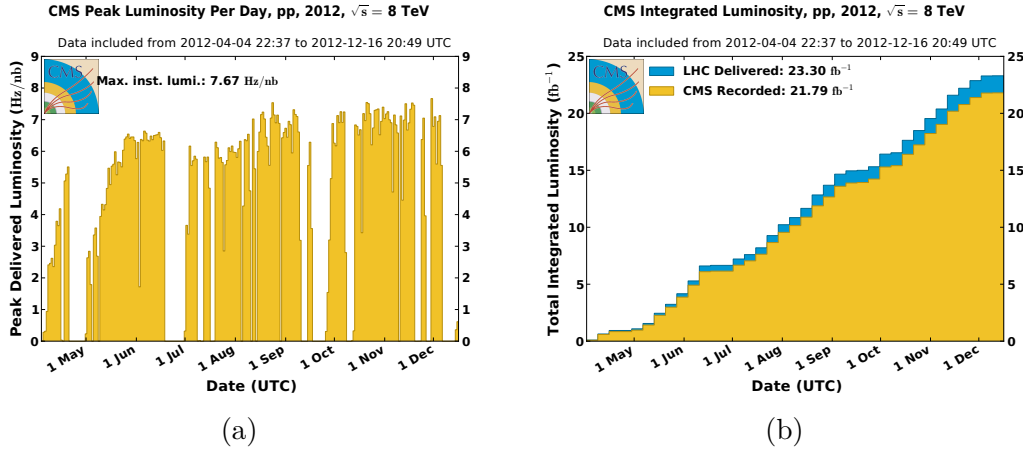


Fig. 3.3 The peak instantaneous luminosity for each day throughout 2012 (a), and the integrated luminosity delivered to and recorded at CMS (b) from [3].

Simultaneous interactions happening at the time of each bunch crossing are referred to as in-time pile up (PU), as opposed to overlapping particle decays from previous bunch crossings called out-of-time pile up (PU). Both phenomena cause significant experimental challenges for detector readout and event reconstruction. The average Pileup distribution for Run I is shown in figure 3.4

3.2 Compact Muon Solenoid

The Compact Muon Solenoid (CMS), is a hermetic detector system (figure 3.5) optimised for the study on high- p_T objects and their decays [46]. It is designed to make accurate measurements of the positions and momenta of physics objects such as electrons, muons, taus, photons and jets. Owing to an almost complete 4π solid angle coverage, CMS is capable of also making accurate measurements of global momentum imbalances due to the presence of weakly interacting particles.

The cylindrical detector is 28 m in length, 15 m in diameter and has a mass of around 14,000 tonnes. The z-axis is taken to be the longitudinal dimension along the beamline, the x-axis the perpendicular direction pointing towards the centre of the LHC ring, and the y-axis pointing skywards, perpendicular to these forming a right-

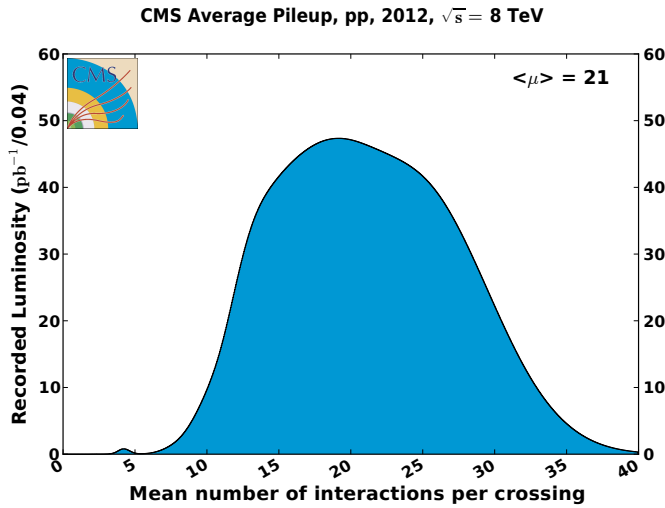


Fig. 3.4 The average Pileup distribution as seen by the CMS detector throughout Run I, taken from [3].

handed co-ordinate system. The transverse plane is taken to be the plane of the x and
1 y axes.

2 Directions relative to the CMS detector are described with the variables ϕ , the
3 angular direction in the transverse plane with the range $[-\pi, \pi]$, and the lorentz-
4 invariant quantity ‘pseudo-rapidity’, η , describing an angle with respect to the z-axis,
5 defined as:

$$\eta = -\ln \tan\left(\frac{\theta}{2}\right) \quad (3.2)$$

7 where θ is the polar angle between the particle trajectory and the beam pipe in the
8 y-z plane. Differences in these two variables, namely $\Delta\phi$ and $\Delta\eta$, are invariant un-
9 der Lorentz boosts, and so can be used to construct a furthermore Lorentz-invariant
10 angular separation between particles:

$$\Delta R = \sqrt{(\Delta\eta)^2 + (\Delta\phi)^2} \quad (3.3)$$

12 CMS is arranged in a layered configuration of sub-detectors, structured as a cylindrical
13 barrel, completed by two end-caps. The barrel contains a super-conducting solenoid
14 magnet capable of producing a 3.8 T magnetic field. Operated at 4.5 K, with a 18.5
15 kA current, the longitudinal field produced bends the trajectories of charged particles
16 allowing for precise charge and momenta measurements.

3.2 Compact Muon Solenoid

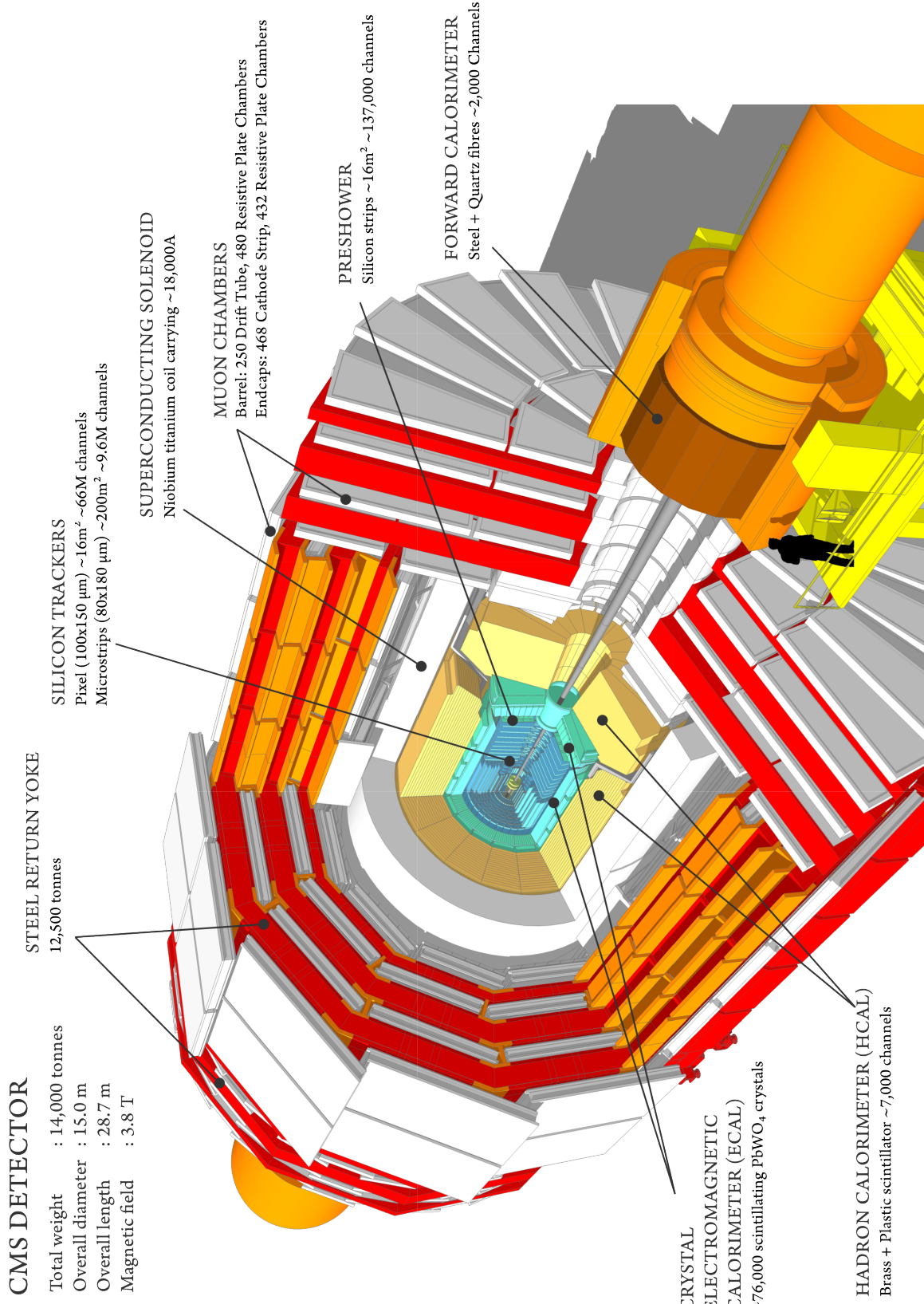


Fig. 3.5 Diagram of the Compact Muon Solenoid taken from [4].

¹⁷ 3.3 Detector Subsystems

¹ The layered structure of the CMS subsystems exists in both the barrel and end-cap
² regions. The following describe each of the subsystems in more detail.

³ 3.3.1 Tracker

⁴ The silicon tracker system consists of inner pixel-based and outer microstrip- based
⁵ detectors.

⁶ The pixel detector consists of three layers of silicon pixel sensors situated as close as
⁷ 4 cm from the beamline, capable of producing 2D hit information of charged particles
⁸ for use in vertex finding with a spatial resolution of $\sim 10\text{-}20\mu\text{m}$. The barrel section
⁹ is accompanied by two end-cap pixel detector disks. Each sensor contains a 52 x 80
¹⁰ grid of $100\ \mu\text{m} \times 150\ \mu\text{m}$ pixels, mounted to a lightweight mechanical substrate along
¹¹ with front-end readout electronics.

¹² A further 10 layers of silicon microstrip detectors are used to accurately reconstruct
¹³ the track path of charged particles. The sensors collectively cover an area of over 200
¹⁴ m^2 , are of p-in-n type, and range from $320\ \mu\text{m}$ to $500\ \mu\text{m}$ in thickness and pixel
¹⁵ pitch ranging between $80\ \mu\text{m}$ and $205\ \mu\text{m}$, depending on distance from the beamline.
¹⁶ The track path can be used to determine both the charge and momentum of charged
¹⁷ particles, the latter with a $\Delta p_{\text{T}}/p_{\text{T}}$ of $\sim 1\text{-}2\%$ for a 100 GeV particle.

¹⁸ All silicon detectors situated so close to the interaction point receive high-doses of
¹⁹ radiation, eventually ageing due to the damage inflicted. Subsequently, radiation hard
²⁰ sensor and front-end electronics materials and designs have been selected to mitigate
²¹ the effects of ageing due to radiation damage.

²² 3.3.2 Electromagnetic Calorimeter

²³ The Electromagnetic Calorimeter (ECAL) system provides accurate measurements of
²⁴ energy deposits and the identification of electromagnetically interacting particles, and
²⁵ can also produce spatial measurements when used in conjunction with data from the
²⁶ tracker system. The detector consists of scintillating lead-tungstate (PbWO_4) crystals,
²⁷ each of dimension 0.017×0.017 ($\Delta\eta \times \Delta\phi$) and 23 cm in length, corresponding to
²⁸ around 26 radiation lengths and providing a Molière radius of 2.2 cm. In both the
²⁹ barrel and the end-cap regions, individual crystals are clustered into super-towers, to
³⁰ match with towers in the trigger system (the calorimeter trigger system is described

3.3 Detector Subsystems

41

³¹ later in section 3.4).

Scintillation light produced in each crystal is collected by either avalanche photo-diodes in the barrel and vacuum photo-triodes in the endcap. The detectors are required to be both radiation hard and capable of operating within the strong magnetic environment of CMS.

The ECAL system is measured as having a $\Delta E/E$ resolution for a 100 GeV particle of $\sim 0.5\%$, exceeding it's technical design requirements.

3.3.3 Hadronic Calorimeter

The Hadronic Calorimeter (HCAL) system measures the energy of hadronic showers originating from single-quarks and gluons (i.e. jets). It is constructed from layers of alternating brass absorber and plastic scintillator, of which there are 17 in the barrel and 19 in the endcaps. The latter are spatially divided into towers measuring 0.087×0.087 in the barrel and end-caps. Hadronic showers of particles deposit energy as scintillation light in the plastic layers, which is transmitted via wavelength shifting fibres to be measured in hybrid photo-diodes. The energy resolution of the HCAL system is calculated with respect to π -meson energy reconstruction, and is measured to be $\sim 90\%/\sqrt{E}$ in the barrel, and $\sim 100\%/\sqrt{E}$ in the endcap.

3.3.4 Muon Systems

The muon system provides identification and precision measurements of muon position and momenta. Energy deposits in the muon systems can be combined with corresponding information from the tracker to improve momentum resolution significantly. It is designed to have an energy resolution, $\Delta p_T/p_T$ of $\sim 10\%$ on it's own, and $\sim 2\%$ when combined with tracker information, both measured for muons with $p_T < 100$ GeV.

Muons are detected in the outer layers of the detector, with the muon system comprised of three different gaseous detector technologies each with different pseudo-rapidity coverage, shown in figure 3.6. The central barrel region, $|\eta| < 1.2$ is equipped with Drift Tube (DT) detectors - a traditional detector technology, optimised for low-occupancy measurements. Cathode Strip Chambers (CSC) cover the forward region, $0.9 < |\eta| < 2.4$, and dual-layered Resistive Plate Chambers (RPC) cover $|\eta| < 2.1$ - both CSC and RPC detectors being optimised for operation in the presence of both high magnetic field and neutron background environments.

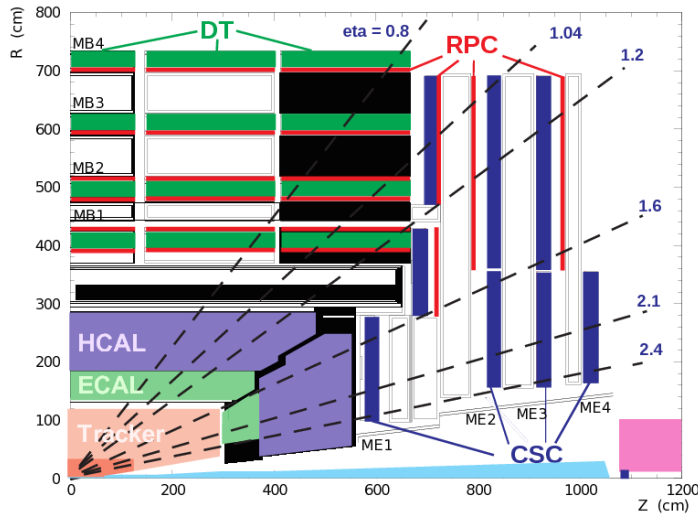


Fig. 3.6 Cross section of the CMS detector in the y - z plane, showing the three muon systems as well as other interior sub-detector systems.

3.4 Trigger and Data Acquisition

32

3.4.1 Trigger system

Events of interest are selected using a dedicated triggering system [47], split into two distinct stages: the hardware-based Level-1 Trigger (L1) and the software-based High-Level Trigger (HLT).

Level-1 Hardware Trigger

The L1 system consists of a staged, modular design of custom built hardware electronics subsystems, as shown in figure 3.7. The L1 trigger reconstructs energy deposits in the calorimeter and muon systems into coarse ‘trigger-primitive’ physics objects. Regional information is gathered by separate modules before being combined in the Global Calorimeter Trigger (GCT) and Global Muon Trigger (GMT) systems, where physics objects are sorted according to energy. Finally, event objects are passed on to the Global Trigger (GT) where a ‘Level-1 Accept’ (L1A) signal is issued or not, dependent on the event meeting one of up to 128 simple object threshold and multiplicity based requirements.

The L1 system is required to run at 40 MHz, equal to the maximal bunch-crossing rate within CMS, with a L1A decision required within a latency of $3 \mu s$. The maximum available output bandwidth of the L1 system is 100 kHz, but typically is maintained

3.4 Trigger and Data Acquisition

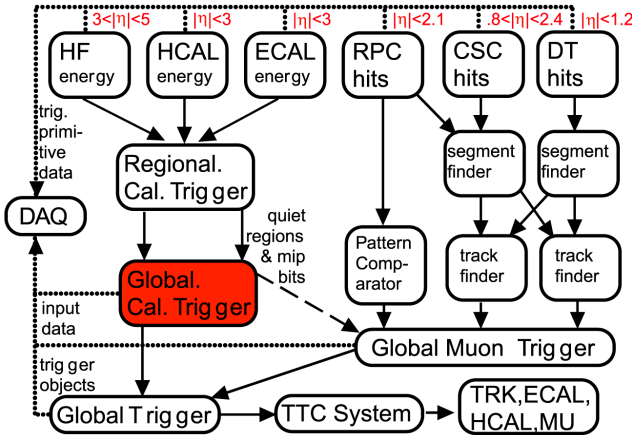


Fig. 3.7 Schematic overview of the Level-1 hardware trigger system of CMS. η coverage is shown in red and the data-flow indicated by arrow direction.

¹⁸ at a lower value to allow for stochastic rate fluctuations.

High-level Trigger

Following a L1A signal, candidate events are optically transmitted to the HLT system, consisting of a large computer farm of server PCs. Due to the increase in available processing time of up to 50 ms, events can be reconstructed in greater detail allowing for a closer emulation of offline reconstruction techniques. Complex analyst-designed trigger rules are used, which can employ more sophisticated event-level variables such as α_T (described in detail later in chapter 6).

The HLT reduces the event rate further by around two orders of magnitude, producing an output event rate of up to 1 kHz. Events passing the HLT are transmitted to Grid system [48] for full offline reconstruction.

Chapter 4

11

Object Definitions

1

4.1 Introduction

2

Physics objects are observed as energy deposits in the various detector subsystems throughout the CMS detector. Specific definitions for the different objects are provided by the Physics Object Groups (*POGs*) and are used in this analysis. The following sections describe the objects used.

3

4

5

6

4.2 Jets

7

Jets are produced when a single quark or gluon is produced, subsequently hadronizing and showering throughout the calorimeter systems. Energy deposits in the hadronic calorimeter are clustered using the anti- k_T algorithm [49] with a $R = 0.5$ cone size parameter. The raw energy measurements are subject to effects from overlapping pp collisions (PU), therefore corrections are made to account for this [50, 51]. Clustered jets are also corrected to establish a uniform response in η and p_T [52]. Table 4.1 summarises the ID requirements used in this analysis, which correspond to the “Loose” working point [53]. Energy deposits clustered into jet objects are corrected to ensure a good translation between measured energy and parton energy. Jets therefore have the following sequential corrections [54] [55] applied:

8

9

10

11

12

13

14

15

16

17

L1 To remove energy coming from PU events, therefore removing any dependence on luminosity across a dataset.

18

19

L2 To ensure a flat energy response in η across the calorimeter.

20

L3 To ensure a flat response according to the p_T of the deposit. 21

- L2L3** Final, additional corrections to bring data and MC into agreement.

Table 4.1 Criteria for the “loose” jet ID working point.

Requirement	Description
$f_{HPD} < 0.98$	Fractional contribution from the “hottest” Hybrid Photo Diode.
$f_{EM} > 0.01$	Minimum electromagnetic fractional component.
$N_{\text{hits}}^{90} \geq 2$	Number of HCAL channels containing at least 90% of total energy

4.2.1 Tagging jets from b-quarks

Jets originating from b-quarks can be identified using information from the vertex detector due to their increased lifetime with respect to light flavour quarks (u, d, s) and charm quarks. B-tagging algorithms are designed to determine the probability that a jet originates from a b-quark, given, amongst other properties, track displacement from the primary vertex (PV). Each algorithm calculates a value used to discriminate between a jet originating from a b-quark and a light or c-quark.

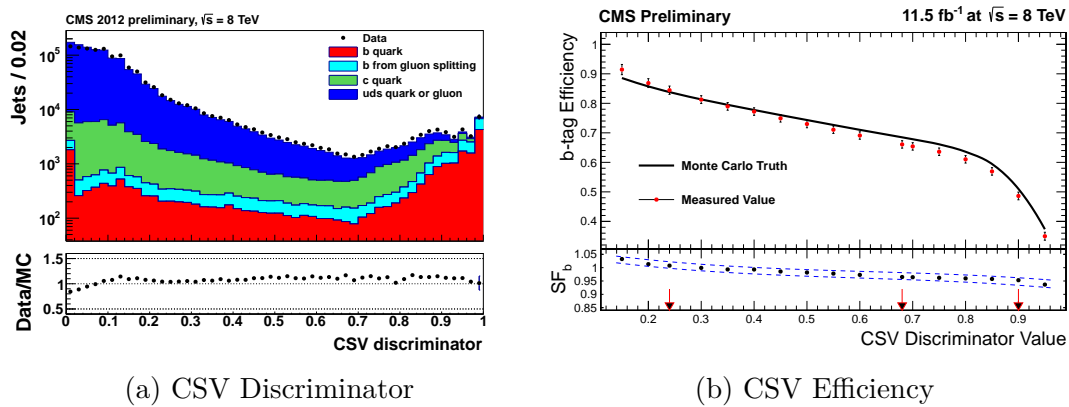


Fig. 4.1 The Combined Secondary Vertex b-tagging algorithm discriminator distribution (left) and the b-tagging efficiency (right) as measured in both data and simulation. MC scale factors are shown in the lower plot of 4.1b.

The Combined Secondary Vertex (CSV) algorithm [56] is used in this analysis. The tagging algorithm calculates a discriminator value for each jet, the distribution being

¹¹ shown in figure 4.1a. The “Medium” working point, or a discriminator threshold of > 0.679 , is used in this analysis. This working point corresponds to a mistag rate for gluons/light-quarks of 1%, and a pT dependent efficiency in the range of 60-70%, as shown in figure 4.1b. Also shown in figure 4.1b are the MC scale factors, SF_b , defined as the ratio of the CSV b-tagging algorithm efficiency in data and MC, to be applied to MC samples.

4.3 Muons

Muons are identified from energy deposits predominantly in the muon systems and the tracker using the muon *POG*’s Tight working point definition [57], as summarised in table 4.2. This definition is used in both muon selection in the μ +jets and $\mu\mu$ +jets control regions, and the muon veto in the hadronic signal region.

Table 4.2 Muon identification (Tight working point).

Variable	Requirement	Description
Global Muon	True	Muon object is reconstructed from both hits in the muon systems and matched hits in the silicon tracker
PFMuon	True	Muon object reconstructed with multiple subsystems using Particle Flow techniques
$\chi^2/ndof$ of fit	< 10	Goodness of fit of the global muon track fit. Suppresses hadronic punch-through and muons decaying in flight.
Muon chamber hits	> 0	At least 1 hit in a muon chamber. Suppresses hadronic punch-through and muons decaying in flight.
Muon station hits	> 1	Muon hits in at least 2 muon stations. Suppresses punch-through and accidental track-to-segment matches. Also makes consistent with trigger muon requirements.
Transverse impact d_{xy}	< 0.2 mm	Tracker track is close to Primary Vertex in the x-y plane. Helps suppress cosmic ray muons and muons from decays in flight.
Longitudinal dist d_z	< 0.5 mm	Tracker track is close to Primary Vertex in z-direction. Suppresses muons from cosmic rays, decays in flight and PU.
Pixel hits	> 0	At least 1 pixel hit. Suppresses muons from decays in flight.
Track layer hits	> 5	Guarantees good p_T measurement.
PF Isolation (PU corrected)	< 0.12	Particle Flow based isolation, based on a cone size of $\Delta R < 0.4$, with “ $\Delta\beta$ ” PU corrections applied.

4.4 Photons

Photons definitions are made relative to their position in the ECAL, either in the barrel or the endcap, as summarised in table 4.3. This Tight working point ID is defined by the *POG* group [58] and used for both photon selection in the γ +jets control sample and as a veto in the hadronic signal region.

Table 4.3 Photon identification (Tight working point).

Categories	Barrel	EndCap	Description
Single Tower H/E	< 0.05	< 0.05	Ratio of energy deposited in the HCAL towers within $\Delta R < 0.15$ of the ECAL supercluster, and the ECAL supercluster itself.
$\sigma_{in\eta}$	< 0.11	< 0.31	The cluster shape covariance of the ECAL supercluster in the η dimension.
PF charged hadron isolation	< 0.70	< 0.50	PF-based isolation
PF neutral hadron isolation	$< 0.4 + 0.04 \times p_T^\gamma$	$< 1.5 + 0.04 \times p_T^\gamma$	requirements to ensure no hadronic or electromagnetic activity with a cone defined by $\Delta R < 0.3$. The isolation is corrected for PU effects.
PF photon isolation	$< 0.5 + 0.005 \times p_T^\gamma$	$< 1.0 + 0.005 \times p_T^\gamma$	

4.5 Electrons

16

- ¹ The Electron *POGs* Loose working point ID [59] is used in this analysis to veto electrons from all areas of the analysis. This cut based identification is defined separately for the barrel and endcap regions of the detector, uses in formation from the calorimeter systems as well as the tracker, and is summarised in table 4.4. The final two requirements are specifically for the rejection of electrons originating from photons converted into e^-e^+ pairs.

Table 4.4 Electron identification (Loose working point).

Categories	Barrel	EndCap	Description
$\Delta\eta_{In}$	< 0.007	< 0.009	The difference between the track and ECAL supercluster in the η dimension.
$\Delta\phi_{In}$	< 0.15	< 0.10	The difference between the track and ECAL supercluster in the ϕ dimension.
$\sigma_{in\eta}$	< 0.01	< 0.03	The cluster shape covariance of the ECAL supercluster in the η dimension.
H/E	< 0.12	< 0.10	Ratio of energy deposited in the HCAL towers within $\Delta R < 0.15$ of the ECAL supercluster, and the ECAL supercluster itself.
d0 (vtx)	< 0.02	< 0.02	The transverse distance of the track from the PV.
dZ (vtx)	< 0.2	< 0.20	The longitudinal distance of the track from the PV.
$ (1/E_{ECAL} - 1/p_{trk}) $	< 0.05	< 0.05	Comparison of the ECAL supercluster energy and the track p_T . Suppresses low p_T fakes.
PF relative isolation	< 0.15	0 < .15	PF based isolation calculated from particle activity within a cone of $\Delta R < 0.3$.
Vertex fit probability	10^{-6}	10^{-6}	Probability of fit to potential conversion tracks.
Missing hits	≤ 1	≤ 1	Number of missing tracker hits due to possible conversion.

4.6 Energy Sums

Physics objects are combined in the form of kinematic variables known as energy sums.
 These are calculated on the fly in the analysis using identified objects, with the exception of \cancel{E}_T which is constructed from PF objects and subject to type-I corrections (jets used for \cancel{E}_T calculation are subject to prescribed Jet Energy Corrections themselves).
 1
 2
 3
 4

The definitions of the energy sum variables are:
 5

$$\begin{aligned} E_T &= \sum_i |\vec{p}_{Ti}| \\ \cancel{E}_T &= -\left| \sum_i \vec{p}_{Ti} \right| \\ H_T &= \sum_i^{\text{jets}} |\vec{p}_{Ti}| \\ \cancel{H}_T &= -\left| \sum_i^{\text{jets}} \vec{p}_{Ti} \right| \end{aligned} \quad (4.1) \quad 6$$

A full set of \cancel{E}_T filters are defined by the MET *POG* as summarised in table 4.5. The filters account for various physics and detector effects which can give un-physical or spurious \cancel{E}_T signals.
 7
 8
 9

Table 4.5 \cancel{E}_T filters employed in the analysis, as recommended by the MET *POG*.

Filter Name	Description
Beam Halo CSC ID	Beam interactions with residual gases in the beam pipe or with mechanical appertures, causing secondary particle production. Events are vetoed if an event contains a positive beam halo ID from the CSC detectors.
HBHE Noise	Noise originating from instrumentation issues with the HCAL's Hybrid Photo Diodes (HPDs) or the Readout Boxes (RBXs). Events are vetoed if they contain isolated cluster of noisy cells in either the barrel or endcap.
Tracking Failure	Significant energy deposits in the calorimeter systems with no corresponding tracks due to tracker algorithm failure. Events are vetoed if the summed p_T of all tracks in the event is equal to less than 10% of the H_T .
HCAL Laser Misfire	Calibration lasers being accidentally fired through the HCAL during bunch crossings (as opposed to abort gaps). Events are removed that contain such accidental laser firings.
DeadECAL Cell TP	Dead or damaged ECAL crystals which cannot read out energy deposits correctly. Trigger primitives are checked to determine how much energy was lost, and events are appropriately masked.

4.7 Single Isolated Tracks

10

¹ Single Isolated Tracks are used to identify hadronically decaying τ leptons and leptonically decaying W bosons where the corresponding lepton has been unidentified for whatever reason. Summarised in table 4.6, the selection is based on particle flow candidates - objects which have been constructed from energy deposits in various detector subsystems according to ‘particle flow’ algorithms. This ID is used as a veto in all selections, with the selected ‘tag’ lepton ignored in the μ +jets and $\mu\mu$ +jets control selections. The ID definition is taken from [60].

Table 4.6 Single Isolated Track identification.

Variable	Requirement	Description
Charge	$\neq 0$	Candidate is charged.
Track p_T	$> 10 \text{ GeV}$	Track transverse momentum requirement.
$\Delta z(\text{track}, \text{PV})$	$< 0.05 \text{ cm}$	Longitudinal distance of track from primary vertex.
Relative Track Isolation	< 0.1	Isolation relative to other PF candidate tracks in cone of $\Delta R < 0.3$

⁸ Chapter 5

Datasets and MonteCarlo samples

5.1 Datasets

The datasets used in this analysis are listed in Table 5.1. These include the primary signal sample datasets, named ‘HTMHTParked’, and other datasets containing events from triggers used for background estimation.

Table 5.1 8 TeV Datasets.

Dataset	Luminosity (fb^{-1})
/HTMHTParked/Run2012B-22Jan2013-v1/AOD	4.41
/HTMHTParked/Run2012C-22Jan2013-v1/AOD	6.80
/HTMHTParked/Run2012D-22Jan2013-v1/AOD	7.29
Total	18.49
/JetHT/Run2012B-22Jan2013-v1/AOD	4.39
/JetHT/Run2012C-22Jan2013-v1/AOD	6.80
/JetHT/Run2012D-22Jan2013-v1/AOD	7.29
Total	18.48
/SingleMu/Run2012A-22Jan2013-v1/AOD	0.69
/SingleMu/Run2012B-22Jan2013-v1/AOD	4.40
/SingleMu/Run2012C-22Jan2013-v1/AOD	6.77
/SingleMu/Run2012D-22Jan2013-v1/AOD	7.27
Total	19.13
/Photon/Run2012A-22Jan2013-v1/AOD	0.68
/SinglePhoton/Run2012B-22Jan2013-v1/AOD	4.40
/SinglePhoton/Run2012C-22Jan2013-v1/AOD	6.77
/SinglePhotonParked/Run2012D-22Jan2013-v1/AOD	7.27
Total	19.12

5.2 MonteCarlo Background and Signal samples

The full list of MonteCarlo (MC) samples used in this analysis are listed in Table 5.2 along with the number of events, next-to-next-to-leading order (NNLO) cross section

and an effective integrated luminosity for each.

The Parton Density Functions (PDF) of colliding protons are modelled according to the CTEQ6L1 distribution, the matrix-element level hard-scatter performed by MADGRAPH5 or PYTHIA6, with outgoing partons showered in PYTHIA6. The produced generator level particles are then put through a full detector simulation in GEANT, and detector hits ‘digitized’ in order to simulate the response of detector electronics. Prior to digitization, a number of ‘MinimumBias’ events are over-layed in order to reproduce LHC run conditions. Event-level weights are applied to each simulated sample such that both the PU and equivalent integrated luminosity are matched to a given data sample.

Additional corrections are made to simulated event samples in order to correct the efficiency of b-tagging algorithms to match that seen in data. Corrections are determined as a function of jet-flavour (light/c/b), defined as:

$$SF_{light,c,b} = \frac{\epsilon_{light,c,b}^{data}(p_T, \eta)}{\epsilon_{light,c,b}^{MC}(p_T, \eta)} \quad (5.1)$$

where $\epsilon_{light,c,b}^X$ represents p_T and η dependent b-tagging efficiencies measured in data and MC.

5.2 MonteCarlo Background and Signal samples**53**

Table 5.2 MC samples for Standard Model processes.

Sample	N _{event}	Cross section (pb)	Corrected	Cross section (pb)	Luminosity (fb ⁻¹)
/NJetsToMu_TuneZ2star_8TeV-madgraph-tarball/Summer12_DR53X_PU_S10_START53_VTA-v1/AODSIM	57661905	37569.0		34133.2	1.5
/NJetsToMu_HF-150to200_8TeV-madgraph/Summer12_DR53X_PU_S10_START53_VTC-v1/AODSIM	21414209	253.8		234.53	84.4
/NJetsToMu_HF-200to250_8TeV-madgraph/Summer12_DR53X_PU_S10_START53_VTC-v1/AODSIM	9895771	116.5		103.94	84.9
/NJetsToMu_HF-250to300_8TeV-madgraph/Summer12_DR53X_PU_S10_START53_VTC-v1/AODSIM	4924990	57.6		51.34	85.5
/NJetsToMu_HF-300to400_8TeV-madgraph_v2/Summer12_DR53X_PU_S10_START53_VTC-v1/AODSIM	5141023	48.4		42.41	106.2
/NJetsToMu_HF-400toInf_8TeV-madgraph_v2/Summer12_DR53X_PU_S10_START53_VTC-v1/AODSIM	4923847	30.8		26.36	159.9
/2JetsToLnu_50_HT_100_8TeV-madgraph_C/Summer12_DR53X_PU_S10_START53_VTA-v1/AODSIM	23743998	452.8		405.21	52.4
/2JetsToLnu_100_HT_200_TuneZ2star_8TeV-madgraph_C/Summer12_DR53X_PU_S10_START53_VTA-v1/AODSIM	9876059	190.4		173.76	51.9
/2JetsToLnu_200_HT_400_TuneZ2star_8TeV-madgraph_C/Summer12_DR53X_PU_S10_START53_VTA-v1/AODSIM	9649619	45.1		42.41	214.0
/2JetsToLnu_400_HT_inf_TuneZ2star_8TeV-madgraph_C/Summer12_DR53X_PU_S10_START53_VTA-v1/AODSIM	5079710	6.26		5.81	811.5
/TT_C10_TuneZ2star_8TeV-powheg-tauola/Summer12_DR53X_PU_S10_START53_VTA-v1(v2)/AODSIM	27144	234.0		215.8	115.8
/TTJets_8TeV-madgraph_v2/Summer12_DR53X_PU_S10_START53_VTA-v1(AODSIM	210160	0.172		0.172	1221.9
/T_t-channel_TuneZ2star_8TeV-powheg-tauola/Summer12_DR53X_PU_S10_START53_VTA-v1/AODSIM	3710227	56.4		56.4	65.8
/Tbar_t-channel_TuneZ2star_8TeV-powheg-tauola/Summer12_DR53X_PU_S10_START53_VTA-v1/AODSIM	1935072	30.7		30.7	63.0
/T_s-channel_TuneZ2star_8TeV-powheg-tauola/Summer12_DR53X_PU_S10_START53_VTA-v1/AODSIM	243961	3.79		3.79	64.4
/T_tW-channel_Dr_TuneZ2star_8TeV-powheg-tauola/Summer12_DR53X_PU_S10_START53_VTA-v1/AODSIM	139974	1.76		1.76	79.5
/T_tW-channel_Dr_TuneZ2star_8TeV-powheg-tauola/Summer12_DR53X_PU_S10_START53_VTA-v1/AODSIM	497658	11.1		11.1	44.8
/Tbar_tW-channel_1Dr_TuneZ2star_8TeV-powheg-tauola/Summer12_DR53X_PU_S10_START53_VTA-v1/AODSIM	493460	11.1		11.1	44.5
/DijetsToLL_M-10to60filter_8TeV-madgraph/Summer12_DR53X_PU_S10_START53_VTA-v1/AODSIM	7116223	13124.1		1205.4	0.5
/DijetsToLL_M-50_TuneZ2star_8TeV-madgraph-tarball/Summer12_DR53X_PU_S10_START53_VTA-v1/AODSIM	30171503	3503.7		3268.45	8.6
/DijetsToLL_M-50_TuneZ2star_8TeV-madgraph_taus/Summer12_DR53X_PU_S10_START53_VTA-v1/AODSIM	6892777	24.3		22.24	283.7
/DijetsToLL_M-50_TuneZ2star_8TeV-madgraph_taus/Summer12_DR53X_PU_S10_START53_VTA-v1/AODSIM	2695789	3.36		3.31	802.3
/GJets_HF-400toInf_TuneZ2star_8TeV-madgraph/Summer12_DR53X_PU_S10_START53_VTA-v1/AODSIM	57891147	1140.8		1060.9	50.7
/GJets_HF-400toInf_8TeV-madgraph/Summer12_DR53X_PU_S10_START53_VTA-v1/AODSIM	9459562	124.7		115.97	75.9
/WW_TuneZ2star_8TeV_pythia6_tauola/Summer12_DR53X_PU_S10_START53_VTA-v1/AODSIM	9884831	57.1		57.1	173.2
/WZ_TuneZ2star_8TeV_pythia6_tauola/Summer12_DR53X_PU_S10_START53_VTA-v1/AODSIM	9841248	12.6		12.6	781.1
/ZZ_TuneZ2star_8TeV_pythia6_tauola/Summer12_DR53X_PU_S10_START53_VTA-v1/AODSIM	9751908	8.26		8.26	1180.6
/QCD_Pt-50to60_TuneZ2star_8TeV_pythia6/Summer12_DR53X_PU_S10_START53_VTA-v2	5952660	8148778 (LO)		8148778 (LO)	0.001
/QCD_Pt-60to80_TuneZ2star_8TeV_pythia6/Summer12_DR53X_PU_S10_START53_VTA-v2	5962864	1033680 (LO)		1033680 (LO)	0.006
/QCD_Pt-80to100_TuneZ2star_8TeV_pythia6/Summer12_DR53X_PU_S10_START53_VTA-v3	5985732	156293 (LO)		156293 (LO)	0.038
/QCD_Pt-100to120_TuneZ2star_8TeV_pythia6/Summer12_DR53X_PU_S10_START53_VTA-v3	20155180	34138 (LO)		34138 (LO)	0.590
/QCD_Pt-120to170_TuneZ2star_8TeV_pythia6/Summer12_DR53X_PU_S10_START53_VTA-v1(v2,v3)	23588100	1759.5 (LO)		1759.5 (LO)	13.4
/QCD_Pt-170to230_TuneZ2star_8TeV_pythia6/Summer12_DR53X_PU_S10_START53_VTA-v1(v2,v3)	3978848	113.9 (LO)		113.9 (LO)	34.9
/QCD_Pt-230to340_TuneZ2star_8TeV_pythia6/Summer12_DR53X_PU_S10_START53_VTA-v2	3964864	27.0 (LO)		27.0 (LO)	146.8
/QCD_Pt-340to470_TuneZ2star_8TeV_pythia6/Summer12_DR53X_PU_S10_START53_VTA-v2	3854633	3.55 (LO)		3.55 (LO)	1085.3
/QCD_Pt-470to600_TuneZ2star_8TeV_pythia6/Summer12_DR53X_PU_S10_START53_VTA-v2	1964088	0.738 (LO)		0.738 (LO)	2661.4
/QCD_Pt-600to1400_TuneZ2star_8TeV_pythia6/Summer12_DR53X_PU_S10_START53_VTA-v1	1988062	0.0335 (LO)		0.0335 (LO)	59345.1
/QCD_Pt-1400to1800_TuneZ2star_8TeV_pythia6/Summer12_DR53X_PU_S10_START53_VTA-v1	977586	0.00183 (LO)		0.00183 (LO)	534200
/QCD_Pt-1800_TuneZ2star_8TeV_pythia6/Summer12_DR53X_PU_S10_START53_VTA-v1	50081518	1.036E7 (LO)		1.036E7 (LO)	0.005
/QCD_Pt-470to600_TuneZ2star_8TeV_pythia6/Summer12_DR53X_PU_S10_START53_VTA-v1/AODSIM	27062078	276000 (LO)		276000 (LO)	0.1
/QCD_Pt-600to800_TuneZ2star_8TeV_pythia6/Summer12_DR53X_PU_S10_START53_VTA-v1/AODSIM	27613225	8426 (LO)		8426 (LO)	3.3
/QCD_Pt-800to1000_TuneZ2star_8TeV_pythia6/Summer12_DR53X_PU_S10_START53_VTA-v1/AODSIM	12018415	204 (LO)		204 (LO)	58.9

Interpretations are made using signal MC samples, each representing a scan in the phase space of a specific SMS model. The samples used are listed in Table 5.3. Each sample is generated at the parton level using MADGRAPH5 and then decayed using PYTHIA6. Diagrams for up to two additional partons are simulated in the initial generation step to ensure good modelling of initial state radiation (ISR), however supplementary samples were produced with up to three additional partons to allow for systematic studies into the effect on the analysis, as detailed in chapter 9.

Signal MC samples use the FASTSIM detector simulation framework in order to simulate detector and electronics responses. In comparison to the FULLSIM method used for all other MC backgrounds, FASTSIM aims to greatly reduce the processing time required to generate samples by avoiding the CPU-intensive full detector simulation using the GEANT framework, instead employing detector response parametrisations tuned using FULLSIM samples.

Table 5.3 MC samples for Simplified Model Spectra.

Model	Sample	Description
T2cc	/SMS-MadGraph_21_T2cc_NoFilter.mStop=100to230_mLSP=20to300_8TeV-Pythia6Z_Summer12-START52_V9_FSM-v1/AODSIM	Original scan
T2cc	/SMS-T2cc_2J_mFilter.mStop=175to240_mLSP=95to240_8TeV-Pythia6Z_Summer12-START52_V9_FSM-v1/AODSIM	Original scan
T2cc	/SMS-T2cc_2J_mStop=250to350_mLSP=195to340_8TeV-madgraph-tauola/Summer12-START53_V19_FSM-v2/AODSIM	Scan extension
T2cc	/SMS-8TeV_Pythia6Z_T2cc_3jets.mStop=200_mLSP=120/Summer12-START52_V9_FSM-v1/AODSIM	3-parton sample
T2dgen	/SMS-T2Dgeneratoratstop_21_mStop=100to150_mLSP=20to0140_TuneZ2star_8TeV-madgraph-tauola/app/Summer12-START53_V19_FSM-v1/AODSIM	3-parton sample
T2dgen	/SMS-T2Dgeneratoratstop_21_mStop=175to225_mLSP=95to215_TuneZ2star_8TeV-madgraph-tauola/app/Summer12-START53_V19_FSM-v1/AODSIM	Original scan
T2dgen	/SMS-T2Dgeneratoratstop_21_mStop=280to300_mLSP=170to290_TuneZ2star_8TeV-madgraph-tauola/app/Summer12-START53_V19_FSM-v1/AODSIM	Original scan
T2dgen	/SMS-T2Dgeneratoratstop_21_mStop=325to375_mLSP=24to365_TuneZ2star_8TeV-madgraph-tauola/app/Summer12-START53_V19_FSM-v1/AODSIM	Original scan
T2dgen	/SMS-T2Dgeneratoratstop_21_mStop=400_mLSP=320to390_TuneZ2star_8TeV-madgraph-tauola/app/Summer12-START53_V19_FSM-v1/AODSIM	Original scan

5.3 Correcting SM sample cross sections

5.3.1 H_T^{parton} binned samples

In order to increase statistics this analysis makes use of MC samples binned in parton-level H_T (H_T^{parton}). Leading order (LO) cross-sections are provided with these samples, which are translated into next-to-next-to-leading order (NNLO) cross-sections using translation-factors (k-factors) derived from corresponding inclusive sample cross-sections. However, recent CMS studies (REF) have shown that the provided LO cross-sections for H_T^{parton} binned samples can be incorrect by up to 10%. This is shown in figure 5.1a, where un-physical steps are present in the ratio between the $Z(\nu\nu) + \text{jets}$ binned sample and the DY + jets inclusive sample.

Two of the binned samples have corresponding inclusive samples to allow for this comparison to be made, namely W + jets and DY + jets. For these two cases, the derivation of corrections for each H_T^{parton} binned sample is simple. However, for $Z(\nu\nu) + \text{jets}$ and $\gamma + \text{jets}$, no such inclusive samples exist. These binned samples are compared with the inclusive DY + jets sample, where the overall normalisation is set according to the relative branching fraction of $Z \rightarrow \nu\bar{\nu}$ and GAMMA to $Z \rightarrow \ell\ell$, set as 0.505 and VALUE, respectively. An example ratio plot is shown in figure 5.1b, where a constant ratio between the samples is found.

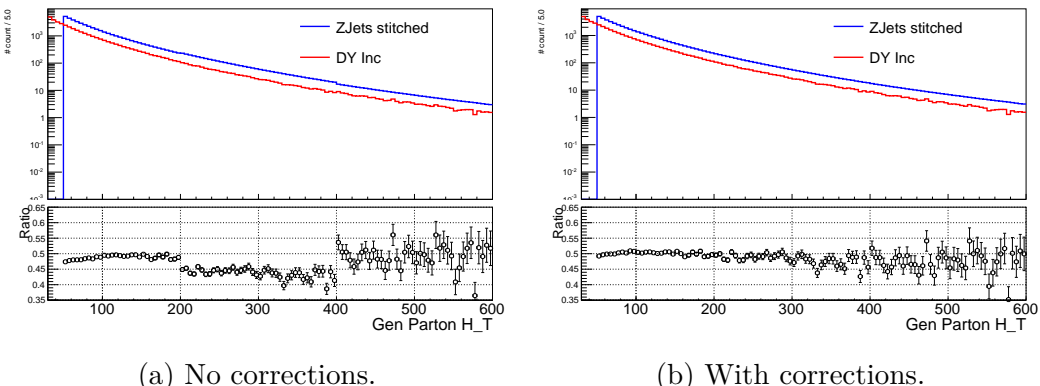


Fig. 5.1 Generator level H_T^{parton} distributions from the inclusive DY + jets and the H_T^{parton} binned $Z(\nu\nu) + \text{jets}$ samples.

5.3.2 HT side-band normalisation

18

As mentioned previously in section 5.3, absolute MC normalisation is not well modelled in the high- \cancel{E}_T region of phase-space in which many SUSY analyses search. As such, data and MC appear to disagree using standard MC samples and cross-sections. While data and MC comparisons are not explicitly used in this analysis, ratios of MC yields are, and so cross-section correction factors for the main MC processes are determined. These are measured as the data to MC ratio in the $150 \leq H_T < 200$ GeV side-band region, in a given control sample with a targetted selection, designed to yield a pure sample of a background process. A summary of the selections and their relevant purities are given in table 5.4.

Table 5.4 Correction factors determined as the ratio of yields in data to those in MC, for a sideband region of $150 < H_T < 200$ GeV. Factors are calculated for process-specific MC samples by choosing a selection enriched in the relevant process, and applied as a global correction.

Process	Selection	Purity	Correction factor
W + jets	$\mu+\text{jets}, 2 \leq n_{\text{jet}} \leq 3, n_b = 0$	0.91	0.93 ± 0.01
Z($\rightarrow \mu\mu$) + jets	$\mu\mu+\text{jets}, 2 \leq n_{\text{jet}} \leq 3, n_b = 0$	0.98	0.94 ± 0.04
t \bar{t}	$\mu+\text{jets}, n_{\text{jet}} \geq 2, n_b \geq 2$	0.87	1.21 ± 0.05

These derived correction factors are tested in the closure tests performed following their application (section 7.3.1).

¹² Chapter 6

The α_T Analysis

6.1 Analysis Overview

Analyses searching in the jets and \cancel{E}_T final state encounter significant backgrounds from SM sources of both genuine and fake \cancel{E}_T . Genuine \cancel{E}_T originates from W and Z boson production, decaying with one or more neutrinos in the final state. In this analysis background predictions are made for these processes using extrapolations into the signal region from independent, process-specific control samples, as described in chapter 7. Fake \cancel{E}_T predominantly is found due to mismeasurements of QCD multijet (MJ) events, which is the dominant process in the hadronic environment and phase space considered in this analysis due to it's very large cross section. Small inconsistencies in the handling of such large backgrounds or rare detector effects can therefore have a significant impact on an analysis. This background is reduced to an entirely negligible level using the dimensionless kinematic variable, α_T (described in section 6.1.1).

In this analysis events are binned in exclusive categories of H_T , and the multiplicity of jets and b-tagged jets, n_{jet} and n_b , as summarised in table 6.1. Such binning allows for targeted interpretations across the vast array of possible simplified model final states, while reducing background yields to a minimum.

The main analysis signal region is described in the remainder of this chapter.

6.1.1 The α_T kinematic variable

Attempting to accurately measure the QCD contribution to the total background is made very difficult given the hadronic environment of the LHC, and the lack of precise

Table 6.1 H_T bin lower bounds used for each n_{jet} and n_b category.

(n_{jet}, n_b)	H_T bins (GeV)										
(2-3,0)	200	275	325	375	475	575	675	775	875	975	>1075
(2-3,1)	200	275	325	375	475	575	675	775	875	975	>1075
(2-3,2)	200	275	325	375	475	575	675	775	>875		
(\geq 4,0)	200	275	325	375	475	575	675	775	875	975	>1075
(\geq 4,1)	200	275	325	375	475	575	675	775	875	975	>1075
(\geq 4,2)	200	275	325	375	475	575	675	775	>875		
(\geq 4,3)	200	275	325	375	475	575	675	775	>875		
(\geq 4, \geq 4)	200	275	325	>375							

measurements and calculations of the large multijet cross sections. As an alternative approach, the goal of this analysis is to reduce QCD down to an entirely negligible level through the use of the dimensionless kinematic variable, α_T . The di-jet variable α was first proposed by Randall et al. in 2008 [61], and later translated into the transverse plane for use with LHC analyses [62, 63]. α_T is defined for di-jets as:

$$\alpha_T = \frac{\sqrt{E_T^{j_2}/E_T^{j_1}}}{\sqrt{2(1 - \cos(\Delta\phi))}} \quad (6.1)$$

where $E_T^{j_1}$ and $E_T^{j_2}$ are the reconstructed transverse energies of the first and second jets respectively, and $\Delta\phi$ is the separation between the two jets in the ϕ plane.

A perfectly measured di-jet event containing back to back jets in ϕ of equal energy will have an α_T value of 0.5, whereas events with \cancel{E}_T originating from jet energy mismeasurements will have values of $\alpha_T < 0.5$. Only events containing sources of genuine \cancel{E}_T , whether from SM or BSM sources, can have values of $\alpha_T > 0.5$.

The α_T variable can be generalised to an n-jet case by considering the event as a pseudo-di-jet system, constructing each pseudo-jet such that the difference in H_T between each pseudo-jet system, ΔH_T , is minimised. α_T then takes the form:

$$\alpha_T = \frac{1}{2} \times \frac{H_T - \Delta H_T}{\sqrt{H_T^2 - \cancel{E}_T^2}} = \frac{1}{2} \times \frac{1 - \frac{\Delta H_T}{H_T}}{\sqrt{1 - \left(\frac{\cancel{E}_T}{H_T}\right)^2}}. \quad (6.2)$$

The α_T variable introduces a correlation between the two variables of \cancel{E}_T and ΔH_T . This relationship is demonstrated in figure 6.1 by the black contours of constant α_T . The different physics sources will populate various regions of this plane. Most

6.1 Analysis Overview

61

¹⁹ notably QCD exhibits a strong correlation between the two variables at low α_T values (figure 6.1a), while processes with real E_T break this correlation, sitting also at higher values of α_T (figures 6.1b and 6.1c).

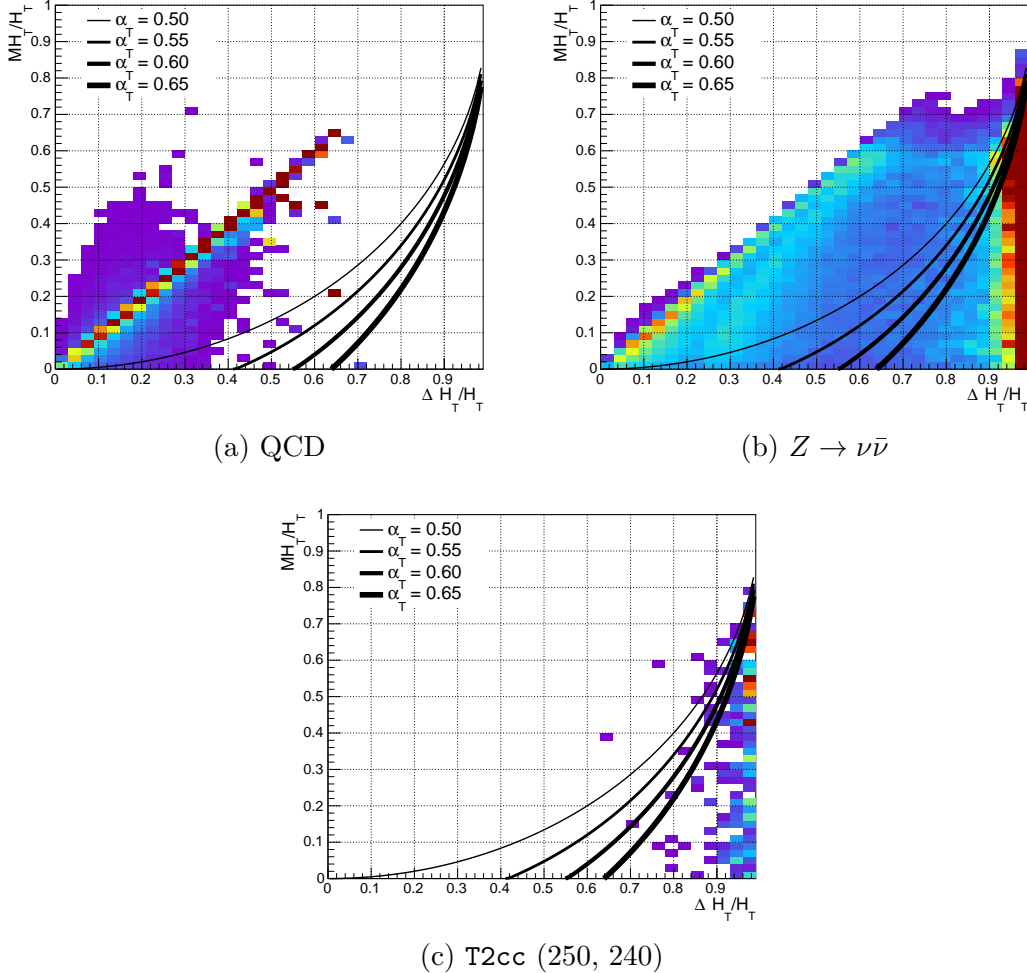


Fig. 6.1 Plots showing the correlation between H_T and ΔH_T for QCD, $Z \rightarrow \nu\bar{\nu}$ and an example SUSY signature T2cc ($m_{\tilde{t}} = 250$ GeV, $m_{\tilde{\chi}^0} = 240$ GeV). Contours of constant α_T are shown in black. Each axis is normalised according to the event H_T show all three?.

Through the requirement of α_T in a given region of H_T , an implied missing energy threshold is made. Figure 6.2 shows this, for the assumption of $\Delta H_T = 0$ - an assumption which yields the minimal \mathcal{H}_T values. By lowering the α_T threshold at higher H_T , the implicit missing energy threshold can be maintained similar to that at low H_T .

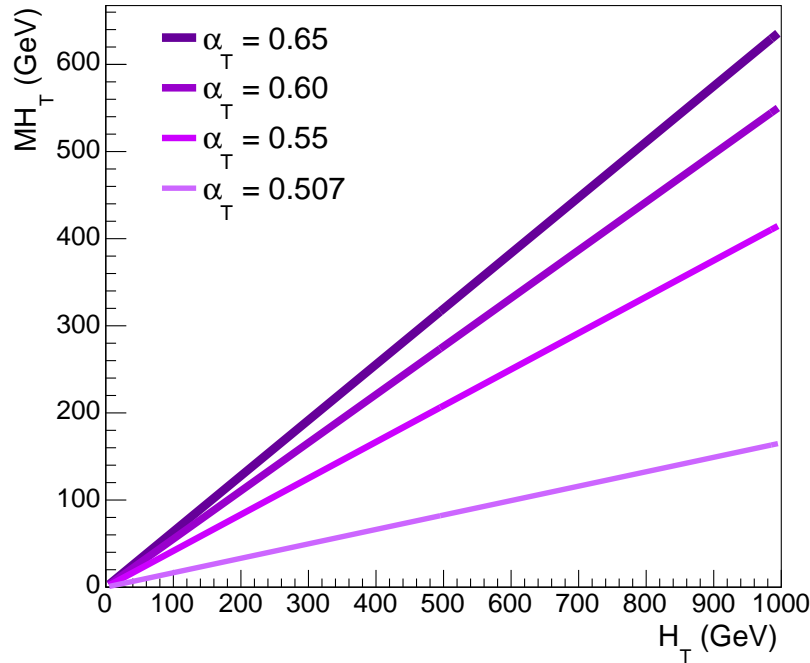


Fig. 6.2 The correlation between H_T and MHT for different α_T values, with the assumption of $\Delta H_T = 0$.

6.2 Standard Model Backgrounds

7

6.2.1 Genuine E_T

The dominant EWK source of genuine missing energy comes from Z-boson production where the Z decays to neutrinos, $Z \rightarrow \nu\bar{\nu}$, with associated jet production. This source of background is considered irreducible.

Events containing leptonic decays of W bosons, $W \rightarrow \ell\nu$, originating either from direct W production, or via the decay of a top quark from $t\bar{t}$ production, are sources of genuine missing energy, due to the presence of a weakly interacting neutrino which evades detection. Such events are vetoed in the signal region due to the presence of a lepton, however if the lepton is missed for whatever reason, leptonic W decays can pass the signal selection, forming a significant SM background.

Leptons can be ‘lost’ for a variety different reasons, but ultimately for failing the lepton ID criteria. There are numerous potential causes, the most prevalent being soft-leptons below ID threshold or non-isolated leptons which pass the ID quality cuts but fail the isolation requirement.

6.2 Standard Model Backgrounds

¹⁵ While originally designed to target hadronically decaying tau leptons, this requirement reduces the remaining lost-lepton backgrounds also.

¹ Following the hadronic selection requirements, any remaining contributions from
² SM EWK backgrounds are estimated using a fully data-driven transfer factor tech-
³ nique, described in detail in Section 7.1. A breakdown of the EWK background com-
⁴ position is shown in Figure 6.3, split into the main categories of $Z \rightarrow \nu\bar{\nu}$, $W + \text{jets}$, $t\bar{t}$
⁵ and remaining residual backgrounds, such as single top quark, diboson and Drell-Yann
⁶ processes.

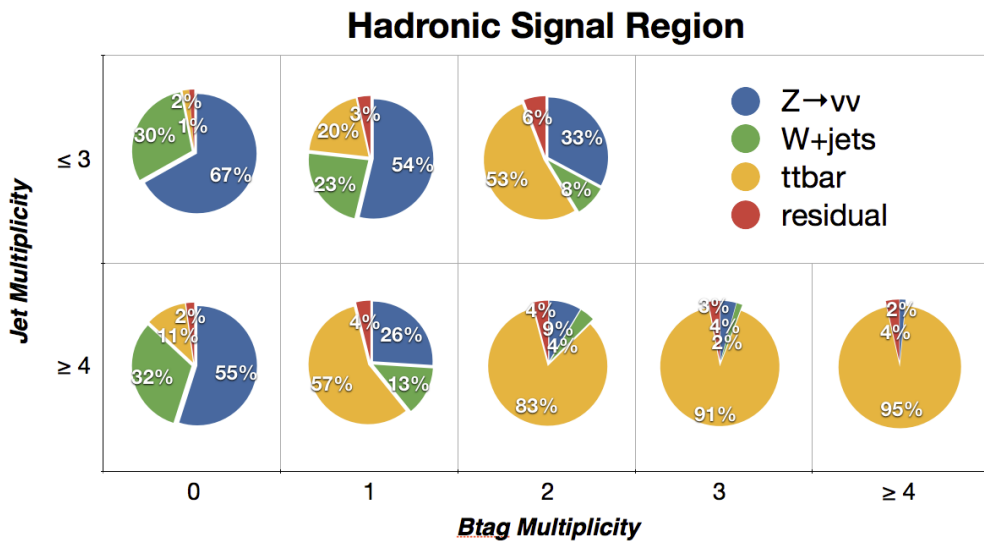


Fig. 6.3 The breakdown of the total electroweak background into component processes as a function of n_{jet} and n_b , for $H_T > 200$ GeV.

6.2.2 Fake \cancel{E}_T

As mentioned previously, the dominant source of background for analyses searching for a multijet final state is from QCD. A fully-measured QCD event would consist of multiple jets balancing each other in all planes, however in order to enter the signal region, an event must contain missing energy, \cancel{H}_T (equivalent to \cancel{E}_T in all-hadronic events).

The most common way for a balanced multijet (MJ) event to gain \cancel{H}_T is when one or more of the jets are mis-measured, such that their vectorial sum then leads to non-zero \cancel{H}_T . This can occur due to detector issues, or due to stochastic fluctuations within

the inherant jet-resolution of the detector. The former is protected against by the \cancel{E}_T filters summarised in table 4.5 and using a filter to remove events affected by non-functioning or damaged regions of the ECAL system, where events are vetoed if they contain significant energy deposits within a given distance from a known problematic region. The latter is dealt with using a cut on the α_T variable where events with fake missing energy signatures give values < 0.5 .

QCD MJ events can also appear to contain non-zero missing energy due to the threshold requirements of jets. If an event contains one or more jets below the analysis threshold, then the event is measured as imbalanced and containing \cancel{H}_T . Events such as these are largely removed with the α_T requirement, however in addition a requirement is made on the ratio $\cancel{H}_T/\cancel{E}_T$.

6.3 Signal Triggers

Events are collected at the HLT using a dedicated suite of signal triggers. For an event to pass the trigger requirements, it must exceed both a H_T and an α_T threshold. Trigger rate can be maintained by varying the threshold requirement on each of these independent requirements, as shown in Table 6.2. Each H_T bin in the analysis is seeded by a particular signal trigger, with a 25 GeV offset in online and offline H_T , with the exception of the 200 GeV bin.

Exclusively for this analysis, the additional ‘Parked’ trigger `HT200_AlphaTop57` is included, seeding the new $H_T > 200$ GeV bin. Such a low threshold allow sensitivity to be maintained for softer physics signatures, such as those expected from compressed spectra SUSY decays.

Table 6.2 Signal triggers, the L1 seed triggers and their efficiencies measured for per H_T and n_{jet} category.

Offline H_T region (GeV)	Offline α_T threshold	L1 seed (L1_?) (highest thresholds)	Trigger (HLT_?)	Efficiency (%)	
				$2 \leq n_{\text{jet}} \leq 3$	$n_{\text{jet}} \geq 4$
$200 < H_T < 275$	0.65	<code>DoubleJetC64</code>	<code>HT200_AlphaTop57</code>	$81.8^{+0.4}_{-0.4}$	$78.9^{+0.3}_{-0.4}$
$275 < H_T < 325$	0.60	<code>DoubleJetC64</code>	<code>HT200_AlphaTop57</code>	$95.2^{+0.3}_{-0.4}$	$90.0^{+1.2}_{-1.3}$
$325 < H_T < 375$	0.55	<code>DoubleJetC64 OR HTT175</code>	<code>HT300_AlphaTop53</code>	$97.9^{+0.3}_{-0.3}$	$95.6^{+0.9}_{-1.0}$
$375 < H_T < 475$	0.55	<code>DoubleJetC64 OR HTT175</code>	<code>HT350_AlphaTop52</code>	$99.2^{+0.2}_{-0.2}$	$98.7^{+0.5}_{-0.7}$
$H_T > 475$	0.55	<code>DoubleJetC64 OR HTT175</code>	<code>HT400_AlphaTop51</code>	$99.8^{+0.1}_{-0.3}$	$99.6^{+0.3}_{-0.7}$

Trigger efficiencies are measured using an unbiased single muon reference trigger, `HLT_IsoMu24_eta2p1`, using a muon tag and probe method where a single muon is

6.4 Selection Criteria

65

²⁴ selected and then subsequently ignored from the analysis when calculating event level variables such as H_T , \mathcal{H}_T and α_T . Efficiencies are measured for each H_T bin and for each n_{jet} category, as summarised in table 6.2. Example trigger ‘turn-on’ curves are shown for the 3 lowest H_T bins in figures 6.4 and 6.5. The curves are shown both differentially and cumulatively, to show the efficiency for events of a given α_T value and above an α_T threshold respectively. Across the higher H_T bins the triggers are fully efficient. Inefficiencies in the low H_T bins are understood as being due to the relatively high threshold L1 seed trigger used for this region, in order to maintain low rates in the high PU environment encountered throughout Run I. Lower efficiencies are also observed in the $n_{jet} \geq 4$ category attributed to the presence of softer jets, as an increased number of jets must equate to the same total H_T requirement of the bin.

All triggers were present throughout Run I, however the ¹¹
¹² `HLT_HT200_AlphaT0p57` trigger was used as part of the ‘Parked’ stream of data which
¹³ was reconstructed at a later date, following the active data taking period. During
¹⁴ data taking triggers may have ‘prescale’ factors applied to them such that only every
¹⁵ n triggered events are actually recorded, however all of the signal triggers remained
¹⁶ unprescaled for the entirety of the 8 TeV data taking.

6.4 Selection Criteria

Event selection requirements for the hadronic signal region are chosen with an aim to maintain sensitivity to hadronically decaying sparticle production, while rejecting as many QCD-type processes as possible. To do so, requirements are made on:

Jets Events are required to contain at least two jets with at least $H_T > 200$ GeV, to ensure the presence of significant hadronic activity. As mentioned previously, events are categorised by H_T , with jet p_T requirements on the two leading and the remaining additional jets separately. The jet p_T thresholds vary as a function of the H_T bin of the event, as shown in Table 6.3, in order to maintain a similar kinematic phase space throughout the H_T range.

Leptons Any events containing leptons are vetoed to ensure hadronic events are considered, thereby suppressing events with genuine \mathcal{E}_T from leptonic decays to neutrinos such as $W \rightarrow \ell\nu$.

Photons Events containing photons are vetoed, for similar reasons as the leptonic vetoes, in order to maintain a purely hadronic environment.

Table 6.3 Jet E_T thresholds per H_T bin.

H_T bin	200–275	275–325	325–375	>375
Lead jet	73.3	73.3	86.7	100.0
Second jet	73.3	73.3	86.7	100.0
All other jets	36.7	36.7	43.3	50.0

6.4 Selection Criteria

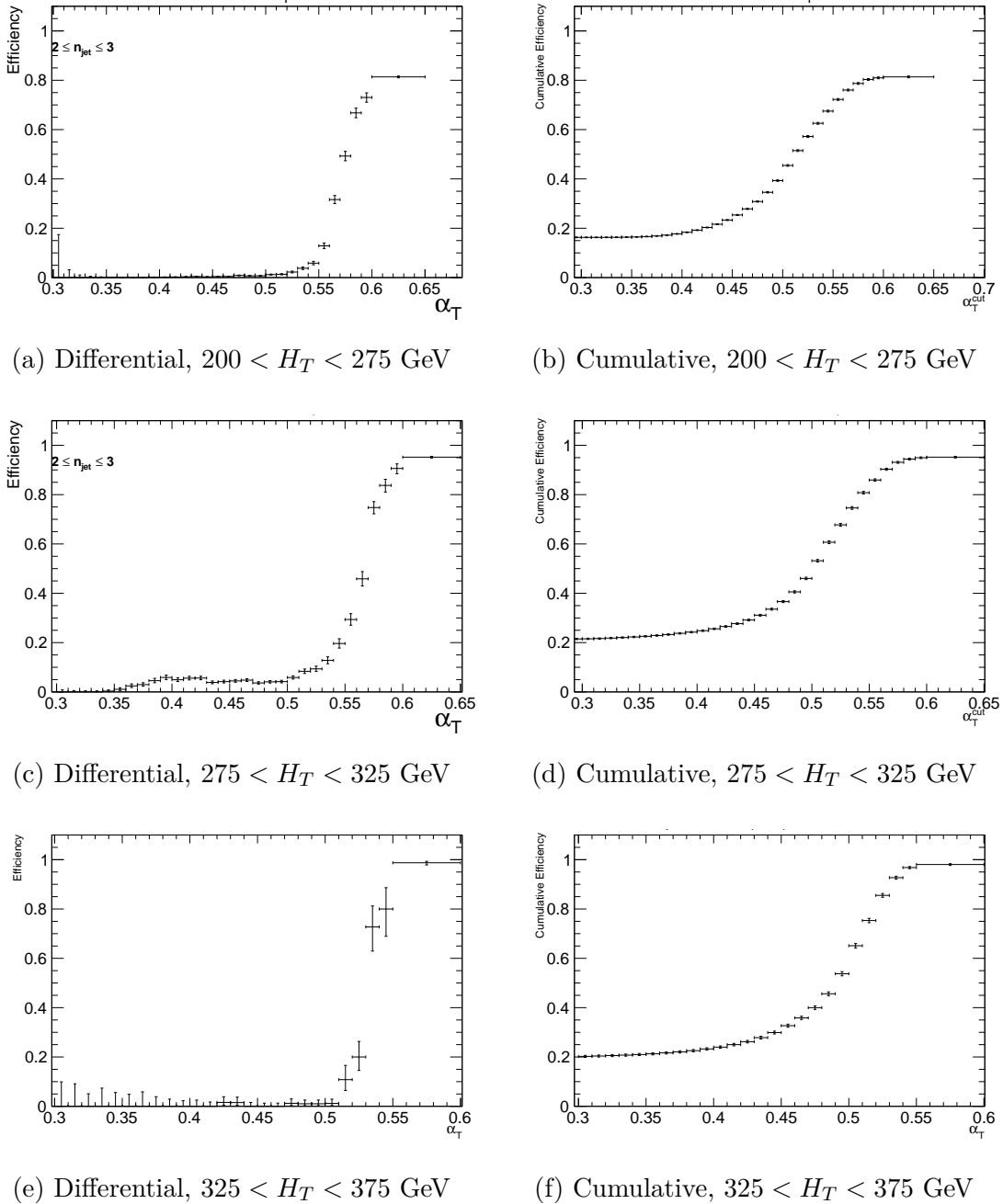


Fig. 6.4 Differential (left) and Cumulative (right) efficiency turn-on curves for the signal triggers, for the three lowest H_T bins and $2 \leq n_{\text{jet}} \leq 3$.

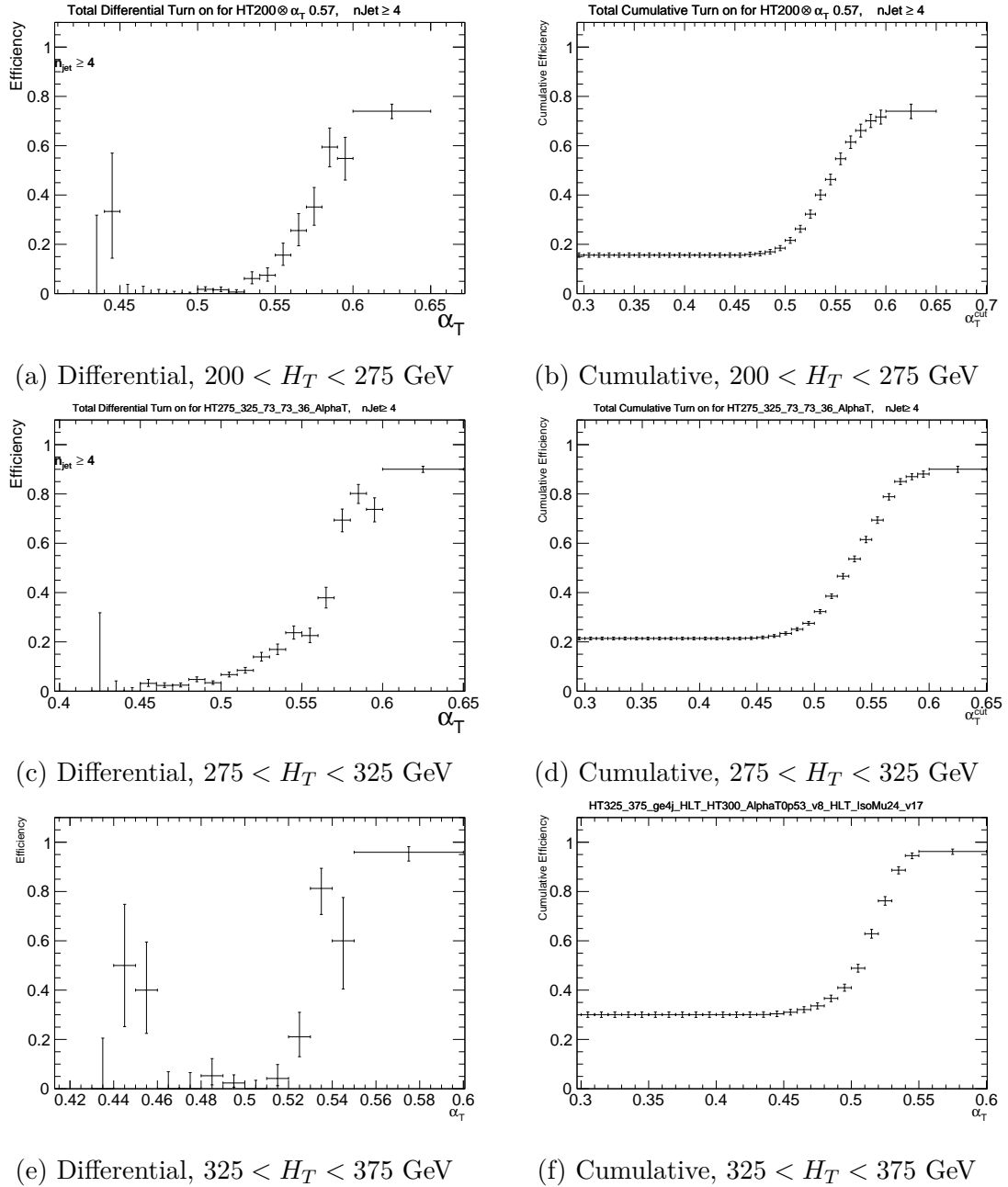


Fig. 6.5 Differential (left) and Cumulative (right) efficiency turn-on curves for the signal triggers, for the three lowest H_T bins and $n_{jet} \geq 4$.

Single Isolated Tracks Events containing a Single Isolated Track (SIT) are vetoed from the signal region. This tracker based veto is particularly useful for vetoing additional events that contain leptons which have failed our lepton ID requirements entirely, and are therefore not considered by the leptonic vetoes. Additionally, the veto also removes background contributions from single-pronged hadronical decays of τ leptons.

Event The topology of the event is required to pass a threshold of $\alpha_T > 0.55$, a requirement which itself varies as a function of the H_T category being considered, always chosen such that the signal triggers are in the efficiency plateau. While no absolute \cancel{E}_T requirement is made, the cut on α_T imposes an implied threshold, which maintains the analysis' sensitivity to very low regions of \cancel{E}_T as shown by figure 6.2.

6.5 Residual QCD cleaning

While the α_T requirement removes many order of magnitude of QCD events, there still exists scenarios in which events may pass the signal region selection. Accordingly, further requirements are made to ensure the search region is free of any residual QCD contamination.

6.5.1 Multiple jets below threshold

Events can acquire non-negligible amounts of \cancel{E}_T without the presence of real \cancel{E}_T if multiple jets are below the analysis threshold, where their configuration can conspire to give a topology passing the α_T thresholds. Such events will contain a disparity between the energy deposit based \cancel{E}_T and jet object based \cancel{E}_T variables. This effect is seen in figure 6.6 where the presence of significant QCD contamination at high values of $\cancel{H}_T/\cancel{E}_T$ is observed, despite an α_T requirement. To protect against this scenario, events are required to have a low ratio of the two variables, specifically $\cancel{H}_T/\cancel{E}_T < 1.25$.

6.5.2 Instrumental effects

Fake \cancel{E}_T may also be produced if jets overlap with areas of the calorimeter system which are damaged or known to be faulty, where jets can be mis-measured or lost as

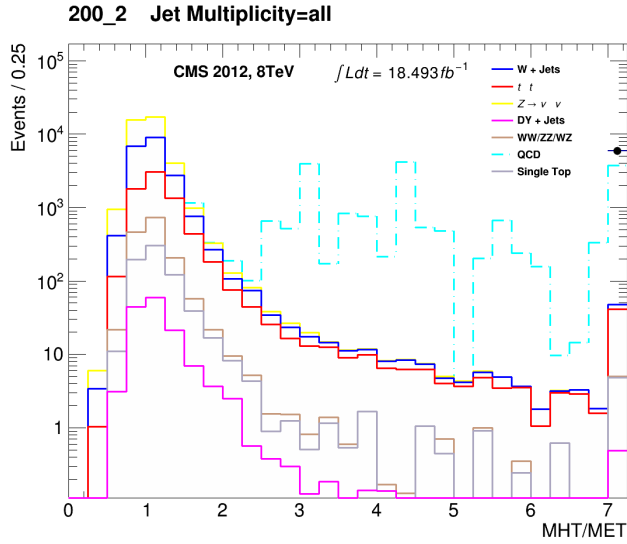


Fig. 6.6 The $\mathcal{H}_T/\mathcal{E}_T$ distribution of MC events following the hadronic selection criteria, minus the $\mathcal{H}_T/\mathcal{E}_T$ requirement. The MC yields are stacked, with the QCD contribution shown in cyan. The plot is for a fully inclusive selection of $n_b \geq 0$, $n_{jet} \geq 2$ and $H_T > 200$ GeV.

a result. To protect against this, for a given jet j , the angular separation between the event \mathcal{H}_T , calculated excluding jet j , and the jet itself is used, defined as:

$$\Delta\phi_j^* = \Delta\phi\left(\vec{p}_{Tj}, -\sum_{i \neq j} \vec{p}_{Ti}\right) \quad (6.3)$$

An advantage of this variable with respect to the often used $\Delta R(jet, MHT)$ is it's detection of spurious missing energy vectors caused by both under-measurements and over-measurements of a jet's transverse momentum. A small value of $\Delta\phi_j^*$ indicates that the momentum vector of j is aligned with the \mathcal{H}_T vector, implying the jet is mis-measured. Events are vetoed if a jet with $\Delta\phi^* < 0.5$ is within $\Delta R < 0.3$ of a known 'dead' region of the ECAL.

Multiple event filters are applied to remove any jet mismeasurements arising due to instrumental effects, however previously un-discovered and therefore rare detector effects may hypothetically be present. To check for this, the jet giving the minimum $\Delta\phi^*$ value in an event, $\Delta\phi_{min}^*$, is found, and a single entry of the η and ϕ direction of the jet's axis is entered into a map of the detector, figure 6.7. Any areas of instrumental issue would be visible as clusters of high event counts. Figures 6.7a and 6.7b shows the detector map and the 1d distribution of counts are shown before the dead ECAL filter is

6.5 Residual QCD cleaning

¹⁶ applied. Areas of potential instrumental defects are clearly visible, notably as outliers
 1 in figure 6.7b. Following the application of the dead ECAL filter the hotspot areas
 2 and the corresponding outliers removed, as seen in figures 6.7c and 6.7d, indicating
 3 there to be no remaining instrumental issues.

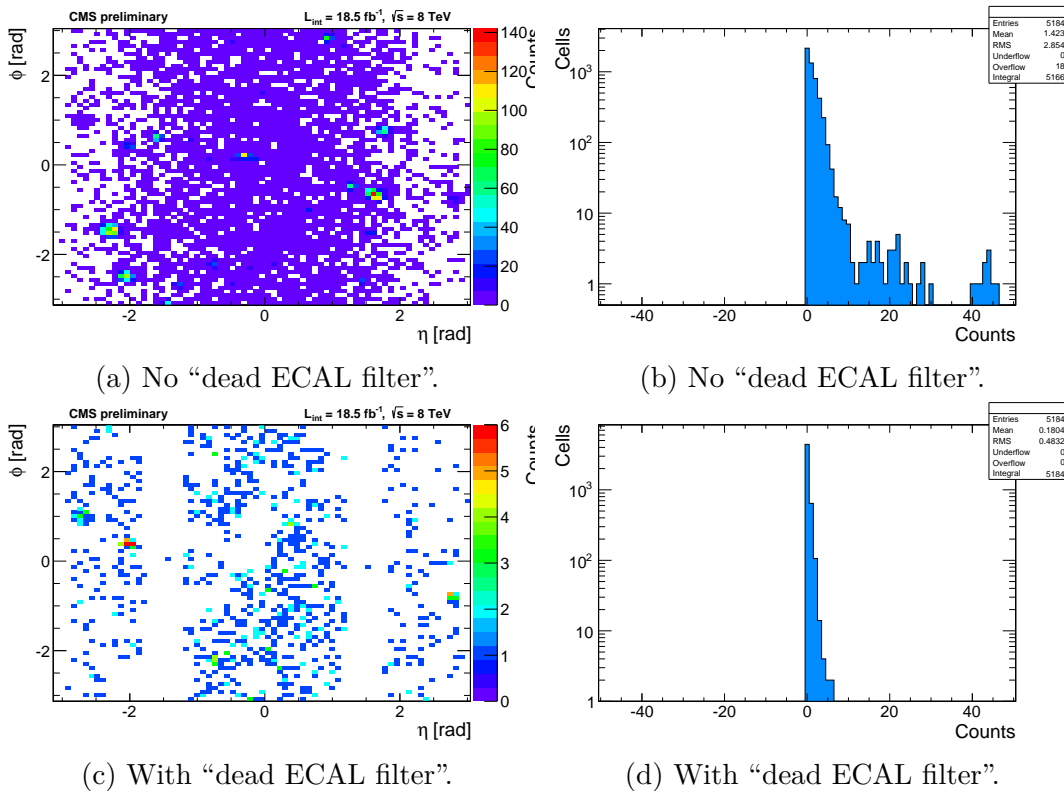


Fig. 6.7 Distribution of jets in (η, ϕ) -space that are responsible for an event satisfying the requirement $\Delta\phi^* < 0.3$, with (a,b) and without (c,d) the “dead ECAL filter” requirement applied as part of the signal region selection.

6.5.3 Heavy-flavour jet decays

This section is still a work in progress and will be updated inline with our analysis note.

Jets can also appear to be mis-measured if they contain the parton shower contains heavy flavour mesons which decay leptonically. In rare circumstances, these decays can give the largest fraction of the available momenta to the neutrino, leading to significant amounts of real \cancel{E}_T and soft-leptons which evade the lepton vetoes (see

appendix B). This effect is compounded when multiple neutrinos are produced in the shower, with a significant fraction of the jet's energy is invisible.

To better study events of this type a control sample is defined, based on using the single-object H_T trigger, HLT-HT750, which remained un-prescaled throughout Run I. As opposed to the typical signal trigger, the lack of an α_T requirement allows lower regions of α_T to be studied. The region is therefore defined by $H_T > 775$ GeV and $\alpha_T > 0.507$, where this trigger is full efficient. Due to the intrinsic correlation of H_T and \mathcal{H}_T in the α_T variable (figure 6.2), this selection leads to an effective \mathcal{H}_T requirement similar to that of the low H_T categories of the nominal analysis.

Events containing jets containing real \mathbb{E}_T sources are likely to have $\mathcal{H}_T \approx \mathbb{E}_T$, and

would therefore not be protected against by the $\mathcal{H}_T/\mathbb{E}_T$ described in section 6.5.1.

Consider the ratio of events passing and failing the $\mathcal{H}_T/\mathbb{E}_T$ requirement:

$$R_{\mathcal{H}_T/\mathbb{E}_T} = \frac{N(\mathcal{H}_T/\mathbb{E}_T < 1.25)}{N(\mathcal{H}_T/\mathbb{E}_T > 1.25)}. \quad (6.4)$$

This variable is plotted as a function of α_T with the predicted EWK background (as determined using the method outlined in chapter 7) subtracted, leaving only QCD multijet events. In the absence of events with jets containing real \mathbb{E}_T a strong exponential decrease would be expected. However, given these events populate the $\mathcal{H}_T/\mathbb{E}_T < 1.25$ region, a constant pedestal is observed REF REF, leading to the conclusion of residual QCD contamination in the signal region.

rmhtmet plots!

Jets containing a \mathbb{E}_T source appear to be mismeasured and will therefore populate a region of low $\Delta\phi^*$. Figure 6.8 shows the data compared to the EWK background prediction (this method is discussed later in chapter 7) as a function of the $\Delta\phi_{min}^*$ value of each event. The disagreement observed at low $\Delta\phi_{min}^*$ is well accounted for by the yield from QCD MC. It should be noted that while MC can be relied on for a qualitative understanding of the QCD contamination, it should not be used to determine a quantitative understanding of the phenomenon.

As motivated by figure 6.8, the residual QCD events appear to be well isolated in the region $\Delta\phi_{min}^* < 0.3$. The effect of applying this threshold in the QCD control study region is shown in figure 6.9. The $\Delta\phi^* > 0.3$ requirement removes these events entirely (CHECK!).

R(MHTMET) plots

dphistar pass/fail plots

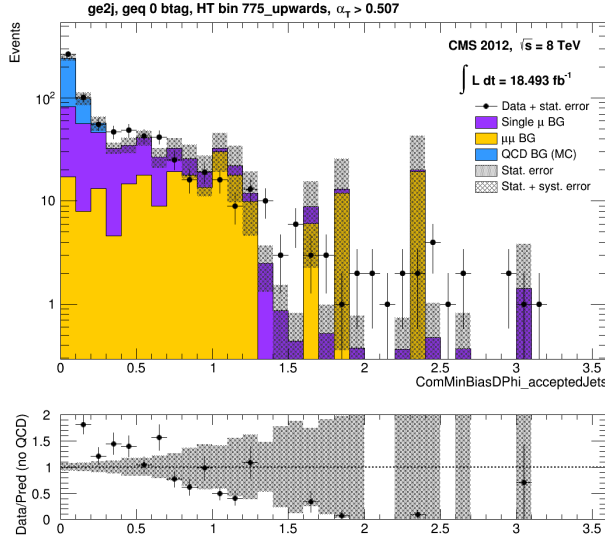


Fig. 6.8 Data (black points) against the EWK background prediction (stacked, yellow and purple) as a function of $\Delta\phi_{min}^*$. The expected yield from QCD MC (cyan) is stacked on top of the EWK prediction. The plot represents the QCD control study region, with $n_b \geq 0$, $n_{jet} \geq 2$, $H_T > 775 \text{ GeV}$ and $\alpha_T > 0.507$.

³³ Events are required to have $\Delta\phi^* > 0.3$, in order to clean any remaining events with jets containing sources of genuine \cancel{E}_T jet (see appendix B).

6.6 Predicting high- n_b event yields

Determining yields for high- n_b analysis categories directly from simulation becomes inherently reliant on not only MC modelling, but also on the physics distribution of jet-flavours. For EWK samples, given the underlying abundance of low b-jet multiplicity events, high- n_b categories become dominated by mis-tagging of light-flavour jets, leading to large statistical uncertainties. In order to reduce this reliance on direct MC yields, a method has been developed REF using flavour tagging efficiencies and the underlying quark flavour distribution, both measured directly from simulation in order to statistically determine more precise yields, particularly for the high- n_b categories.

This method and it's validation are described in detail in REF. The approach can

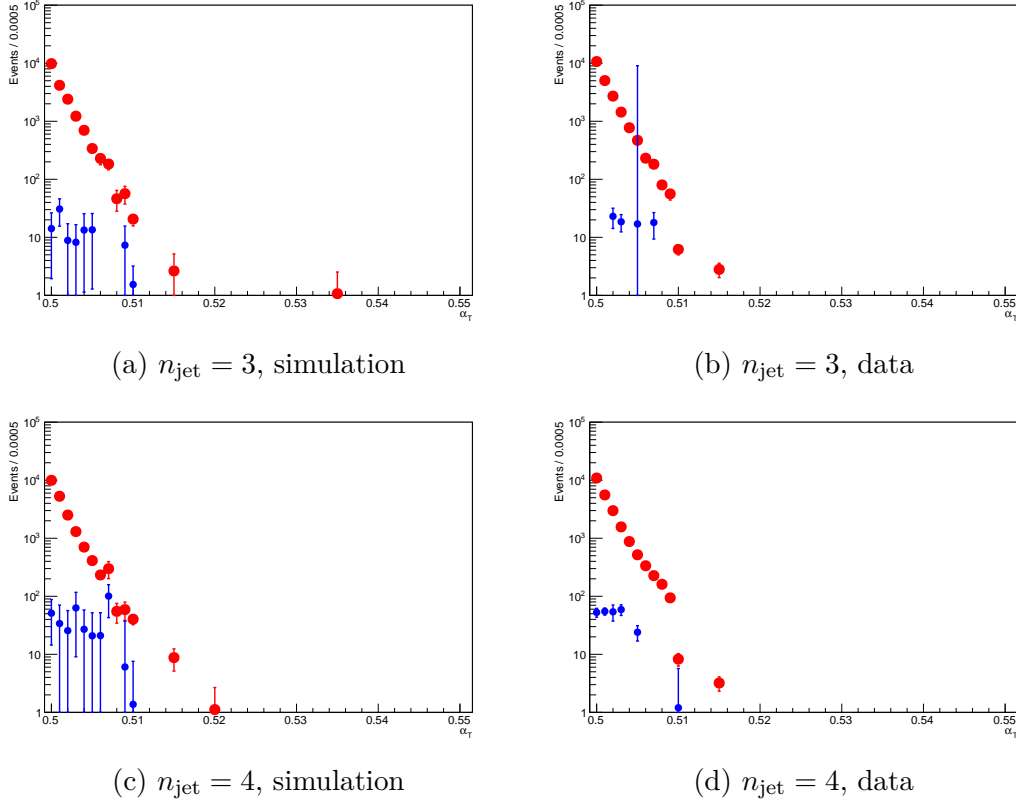


Fig. 6.9 The α_T distribution for events with no $\Delta\phi^*$ requirement (red circles) and with the $\Delta\phi^* > 0.3$ requirement (blue circles) as determined from QCD multijet simulation (left column) or data (right column) and the exclusive $n_{\text{jet}} = 3$ (top row) or $n_{\text{jet}} = 4$ (bottom row). The QCD control study region requirements have been applied, $H_T > 775$ GeV and $\alpha_T > 0.507$, with $n_b \geq 0$.

be summarised by:

$$N(n) = \sum_{n_b^{gen} + n_c^{gen} + n_{light}^{gen} = n_{jet}^{cat}} \sum_{n_b^{tag} + n_c^{tag} + n_{light}^{tag} = n} N(n_b^{gen}, n_c^{gen}, n_q^{gen}) \times \\ P(n_b^{tag}, n_b^{gen}, \epsilon_b) \times P(n_c^{tag}, n_c^{gen}, \epsilon_c) \times P(n_{light}^{tag}, n_{light}^{gen}, \epsilon_{light}) \quad (6.5)$$

where $N(n)$ is represents the predicted yield of n b-tagged events for a given analysis category and H_T bin. The jet-flavour tagging probability terms $P(n_b^{tag}, n_b^{gen}, \epsilon_b)$, $P(n_c^{tag}, n_c^{gen}, \epsilon_c)$ and $P(n_{light}^{tag}, n_{light}^{gen}, \epsilon_{light})$ are measured for each H_T bin and analysis category for each simulated sample, including the flavour tagging efficiencies ϵ_b , ϵ_c and ϵ_{light} as also measured from each sample. Finally, $N(n_b^{gen}, n_c^{gen}, n_q^{gen})$ represents the distribution of actual generator-level jet flavours in the events.

 6.7 Example distributions and cutflow

8 In the large-statistic sample limit this technique would not be necessary, as enough
 1 high- n_b events would be present to sufficiently reduce statistical uncertainties. How-
 2 ever, in the absence of this un-feasible scenario, this technique makes uses of all events
 3 in a sample, thereby reducing the uncertainties and ultimately delivering more precise
 4 yields from simulation.

6.7 Example distributions and cutflow

Example distributions from MC simulations of α_T , H_T , \mathcal{H}_T and jet p_T are shown in
 6 figure 6.10.
 7

The cutflow yields are shown in table 6.4 for data in the $H_T > 375$ GeV region,
 8 with an inclusive selection on n_{jet} and n_b .
 9

Table 6.4 The cutflow of the hadronic selection in data. The subscript ‘fail’ indicates an object which did not meet all ID requirements, and so is not considered as a ‘common object’. The event selection follows an inclusive selection in data of $H_T > 375$ GeV, $n_{jet} \geq 2$ and $n_b \geq 0$.

Cut Name	Eff (%)	N
Event Count	100.00	161866108.00
Good Event JSON Filter	94.97	153716716.00
$n_{jet} \geq 2$	98.68	151689664.00
MET Filters	98.81	149885013.00
Vertex Noise Filter	99.91	149746017.00
DeadECAL Filter	35.44	53066597.00
Select seed Trigger	3.76	1995549.00
$n_e = 0$	98.48	1965269.00
$n_\gamma = 0$	97.70	1920124.00
$n_\mu = 0$	98.36	1888711.00
EMF_{max} for all jets > 0.1	99.99	1888576.00
Leading jet $p_T > 100$ GeV	97.83	1847501.00
Leading jet $\eta < 2.5$	97.31	1797777.00
Sub-Leading jet $p_T > 100$ GeV	81.75	1469654.00
$n_{jet,fail} = 0$	81.73	1201096.00
$\Delta R(\mu_f^i, jet^j) < 0.5$	98.77	1186370.00
$(\sum^{n_{vertices}} p_T) / H_T$	100.00	1186368.00
recHitCut	98.44	1167861.00
$n_{SIT} = 0$	85.77	1001646.00
$\Delta\phi_{min}^* > 0.3$	19.50	195361.00
$H_T > 375$ GeV	73.33	143255.00
$\mathcal{H}_T/\mathbb{E}_T < 1.25$	9.26	13263.00
$\alpha_T > 0.55$	38.25	5073.00

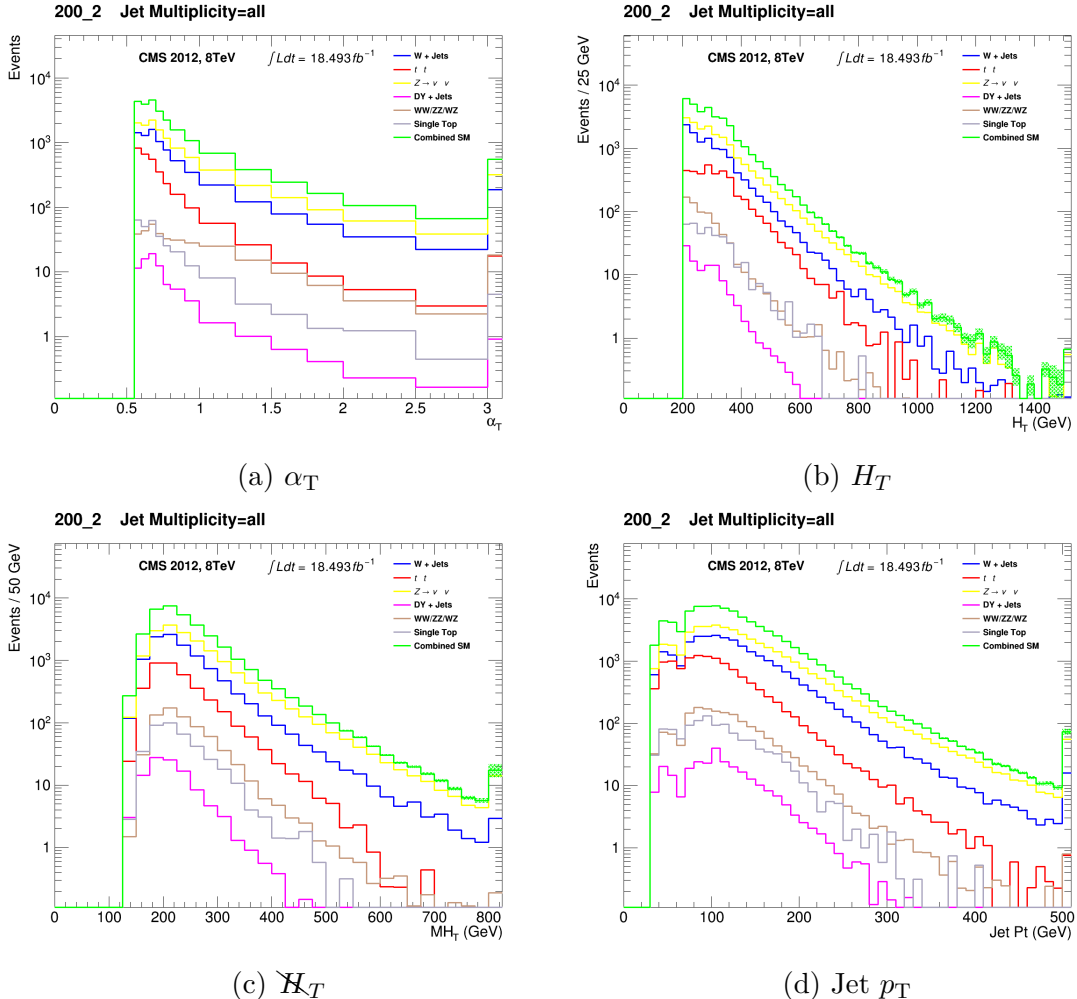


Fig. 6.10 MC distributions for the full hadronic signal selection. The sum of the individual sample contributions is shown in green. Plots are for $H_T > 200$ GeV, $n_{\text{jet}} \geq 2, n_b \geq 0$.

Chapter 7

10

Background Estimation

1

Predictions of EWK SM backgrounds are made using independent, process-specific control regions. These regions are orthogonal to the signal region due to the selection of leptons or photons - particles which are subsequently ignored such that the selection kinematics of each event is kept similar to the corresponding process observed in the signal region. For each sample, Transfer Factors (TF) are constructed from yields in MC, to extract a prediction in the signal region for a given process. This process is described at length in section 7.1.

2

3

4

5

6

7

8

Predictions made using this technique alone are considered as “primitive” predictions and are used only in analysis development and the derivation of background systematics. In order to determine final yields for interpretation and limit-setting, a fit is made across all signal and control regions, using the likelihood model, described later in chapter 8. The derived transfer factors and individual yields enter as terms in the likelihood, where all related systematics, potential correlations and signal contamination are accounted for.

9

10

11

12

13

14

15

7.1 Overview of Electroweak background prediction method

16

17

Contributions from Standard Model background processes are estimated using a data-driven prediction technique, employing dedicated control samples. A transfer factor is constructed from MC samples as the ratio of the MC yield in the signal region, $N_{MC}^{signal}(H_T, n_{jet}, n_b)$, and the MC yield of a given control region, $N_{data}^{control}(H_T, n_{jet}, n_b)$, as a function of the analysis binning, H_T , n_{jet} and n_b , defined

18

19

20

21

22

as:

$$TF = \frac{N_{MC}^{signal}(H_T, n_{jet}, n_b)}{N_{MC}^{control}(H_T, n_{jet}, n_b)} \quad (7.1)$$

- For a given H_T , n_{jet} and n_b bin, the TF is used to extrapolate a yield in data from the control region, $N_{data}^{control}(H_T, n_{jet}, n_b)$ to the signal region $N_{pred}^{signal}(H_T, n_{jet}, n_b)$, using:

$$N_{pred}^{signal}(H_T, n_{jet}, n_b) = N_{data}^{control}(H_T, n_{jet}, n_b) \times TF \quad (7.2)$$

- The control samples are statistically independent and each used for predicting specific background processes, the details of which are described in section 7.2.

MC yields are defined by process from the following samples: W + jets (N_W), $t\bar{t}$ + jets ($N_{t\bar{t}}$), DY + jets (N_{DY}), γ + jets (N_γ), single top + jets (N_{top}), WW + jets, WZ + jets and ZZ + jets ($N_{di\text{-boson}}$), and $Z \rightarrow \nu\bar{\nu}$ + jets ($N_{Z \rightarrow \nu\bar{\nu}}$).

The denominator of each transfer factor is constructed using the sum of *all* MC sample yields, for a given control region selection and analysis category:

$$N_{MC}^{control}(H_T, n_{jet}, n_b) = N_W + N_{t\bar{t}} + N_{DY} + N_\gamma + N_{top} + N_{di\text{-boson}} + N_{Z \rightarrow \nu\bar{\nu}} \quad (7.3)$$

The numerator is constructed according to the b-tag multiplicity being considered. For $n_b \leq 1$, the μ +jets control region is used to predict lost-lepton background, e.g. $t\bar{t}$ + jets and W + jets. All MC samples are therefore used with the exception of $Z \rightarrow \nu\bar{\nu}$:

$$N_{MC}^{signal}(H_T, n_{jet}, n_b \leq 1) = N_W + N_{t\bar{t}} + N_{DY} + N_\gamma + N_{top} + N_{di\text{-boson}} \quad (7.4)$$

The $Z \rightarrow \nu\bar{\nu}$ + jets component of the background is predicted using the $\mu\mu$ +jets and $\gamma\gamma$ +jets control samples, using only the $Z \rightarrow \nu\bar{\nu}$ MC yields:

$$N_{MC}^{signal}(H_T, n_{jet}, n_b \leq 1) = N_{Z \rightarrow \nu\bar{\nu}} \quad (7.5)$$

For $n_b \geq 2$, the μ +jets sample is used to produce a prediction for all SM processes, including $Z \rightarrow \nu\bar{\nu}$, and therefore the numerator of the TF is defined as:

$$N_{MC}^{signal}(H_T, n_{jet}, n_b \geq 2) = N_W + N_{t\bar{t}} + N_{DY} + N_\gamma + N_{top} + N_{di\text{-boson}} + N_{Z \rightarrow \nu\bar{\nu}} \quad (7.6)$$

7.2 Control samples

²⁴ or equivalently:

$$N_{MC}^{signal}(H_T, n_{jet}, n_b \geq 2) = N_{MC}^{signal}(H_T, n_{jet}, n_b \leq 1) + N_{Z \rightarrow \nu\bar{\nu}} \quad (7.7)$$

The $\mu\mu$ +jets and γ +jets control samples are not used beyond the $n_b \leq 1$ categories due to the statistical limitations of such samples at high b-tag multiplicities. A full summary of the control regions used for predictions per analysis category is shown in table 7.1.

Again, it should be noted here that although two separate control samples are used to estimate the $Z \rightarrow \nu\bar{\nu}$ background contribution, the result of each is considered by the global fit to produce the final background prediction.

Table 7.1 The control samples used to produce SM background predictions for each analysis category (n_b , n_{jet}).

n_{jet}	n_b	Control samples
2–3	0	μ +jets, $\mu\mu$ +jets, γ +jets
2–3	1	μ +jets, $\mu\mu$ +jets, γ +jets
2–3	2	μ +jets
≥ 4	0	μ +jets, $\mu\mu$ +jets, γ +jets
≥ 4	1	μ +jets, $\mu\mu$ +jets, γ +jets
≥ 4	2	μ +jets
≥ 4	3	μ +jets
≥ 4	≥ 4	μ +jets

By employing a technique that uses a ratio of MC yields, direct dependence on MC modelling is greatly reduced. Sources of error inherent to MC samples, such as mismodelling effects, will cancel in the ratio. These errors can potentially include kinematic mismodelling, which would affect analysis acceptance, and mismodelling of instrumental effects, which could affect object reconstruction efficiencies. However, any remaining systematics such as these and others are probed using dedicated Closure Tests (CT), described in detail in section 7.3.1.

7.2 Control samples

Control sample definitions are designed such that they are kinematically similar to the signal region, with the exception of a selected ‘tag’ muon or photon. The ‘tagged’ particle is then subsequently ignored for the calculation of all analysis variables, such

as H_T , \cancel{E}_T , α_T etc. Other differences include mass-window and minor kinematic cuts, aimed at enriching the control samples in certain processes. In order to increase statistics in the $\mu+\text{jets}$ and $\mu\mu+\text{jets}$ samples, the α_T requirement is removed. The samples themselves are statistically independent, and orthogonal to the signal region due to the selection of the tagged lepton or photon minimising any possible signal contamination. However, a full treatment of the signal-contamination and sample cross-correlation is taken into account in the background fit and final limit-setting.

7.2.1 $\mu+\text{jets}$

The $\mu+\text{jets}$ control sample is constructed by selecting a single muon with associated jets. This region is used to predict backgrounds from processes such as $W + \text{jets}$ and $t\bar{t} + \text{jets}$. This covers not only the leptonic decays of such productions, where the lepton is not identified for whatever reason, but also the hadronic decays of tau leptons [from high- p_T W bosons]. The event selection therefore is optimised to select W bosons decaying to a muon and a neutrino in the phase-space of the signal.

Triggers

Events are collected using the loosely-isolated, η -restricted `HLT_IsoMu24_eta2p1` trigger, which was in place throughout the 8 TeV data taking period. The efficiency of this trigger was measured by the muon *POG* using a tag-and-probe method [REF], in bins of the muon p_T and η , as summarised in table 7.2. Statistical uncertainties are at the per-mille level, and systematics are assumed to be 1%.

Selection Criteria

A single tight isolated muon is selected, with $p_T > 30$ GeV and $|\eta| < 2.1$. The transverse mass of the W , reconstructed by the μ and the \cancel{E}_T (originating from the ν_μ), is required to be in a loose window around m_W , $30 < M(\mu, \cancel{E}_T) < 125$ GeV. Events are vetoed if $\Delta R(\mu, \text{jet}_i) < 0.5$, for all jets i in the event. To keep the selection as close to the signal region as possible, other cuts such as the single isolated track veto and $\cancel{H}_T/\cancel{E}_T$ cuts are also applied.

Specifically for the $\mu+\text{jets}$ (and $\mu\mu+\text{jets}$) control samples, no α_T requirement is made in order to increase the statistics and therefore the predictive power of the samples. This is possible as other requirements, in particular the requirement of a single muon and a specific invariant mass window, greatly reduce any potential

7.2 Control samples

81

Table 7.2 Muon trigger efficiencies (%) for the μ +jets selection listed by H_T bin and n_{jet} category.

H_T (GeV)	2-3	≥ 4
150–200	87.2	88.1
200–275	87.5	88.1
275–325	87.8	88.2
325–375	87.9	88.4
375–475	88.1	88.6
475–575	88.2	88.8
575–675	88.4	88.9
675–775	88.5	89.0
775–875	88.6	89.1
875–975	88.8	89.0
975–1075	88.7	89.0
>1075	88.4	89.6

³¹ contamination from QCD MJ events. The viability of this is specifically tested by a dedicated closure test, described later in section 7.3.1.

Example distributions of μp_T and μ -corrected \cancel{E}_T for this selection are shown in figure 7.1.

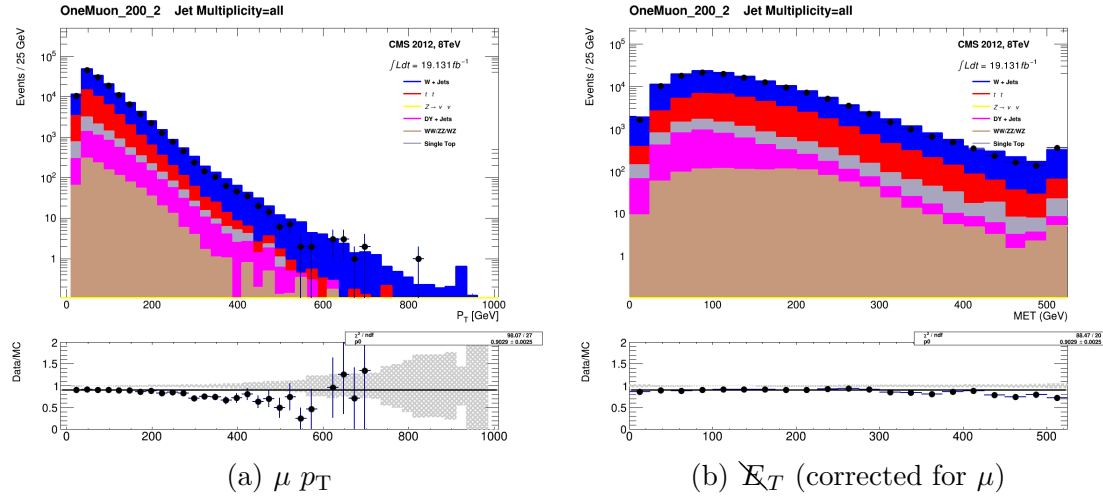


Fig. 7.1 Comparison of data with MC for the μ +jets control selection. Plots are for $H_T > 200$ GeV, $n_{\text{jet}} \geq 2$, $n_b \geq 0$.

7.2.2 $\mu\mu+\text{jets}$

4

- ¹ The $\mu\mu+\text{jets}$ sample is constructed to predict background contributions from $Z \rightarrow \nu\bar{\nu}$
² decays, mimicking this decay via the kinematically similar $Z \rightarrow \mu\mu+\text{jets}$ process where
³ both muons are subsequently ignored. The sample is used to provide low H_T coverage
⁴ for the $Z \rightarrow \nu\bar{\nu}$ background prediction, where the $\gamma+\text{jets}$ sample (section 7.2.3) is
⁵ unable to do so.

6 Triggers

- ⁷ The trigger used is the same as for the $\mu+\text{jets}$ sample, as described in section 7.2.1.
⁸ Trigger efficiencies are significantly improved for the dimuon selection given that either
⁹ of the muons can cause a positive trigger decision, as shown in table 7.3. Relative errors
¹⁰ are considered the same as for the $\mu+\text{jets}$ trigger efficiencies.

Table 7.3 Muon trigger efficiencies (%) for the $\mu\mu+\text{jets}$ selection listed by H_T bin and n_{jet} category.

H_T (GeV)	2-3	≥ 4
150–200	98.4	98.4
200–275	98.5	98.4
275–325	98.5	98.4
325–375	98.6	98.6
375–475	98.6	98.5
475–575	98.6	98.6
575–675	98.6	98.6
675–775	98.7	98.6
775–875	98.6	98.6
875–975	98.7	98.6
975–1075	98.7	98.8
>1075	98.7	98.7

11 Selection Criteria

- ¹² The selection for the $\mu\mu+\text{jets}$ sample is very similar to that of the $\mu+\text{jets}$ sample,
¹³ described in section 7.2.1, with differences chosen to enrich the sample in Z bosons
¹⁴ decaying to pairs of muons in the kinematic phase space of the signal region. Two tight
¹⁵ isolated muons are selected, each with $p_T > 30$ GeV and $|\eta| < 2.1$. Their invariant
¹⁶ mass is chosen to be tight around m_Z , $m_Z - 25 < M_{\mu_1\mu_2} < m_Z + 25$ GeV. Furthermore,

7.2 Control samples

83

- ¹⁷ a veto is made on events satisfying $\Delta R(\mu_i, \text{jet}_j) < 0.5$, for every muon i and every jet j . Similarly as in the $\mu+\text{jets}$ sample selection, no α_T requirement is made.

Example distributions of $M_T(\mu\mu)$ and $\mu_2 p_T$ for this selection are shown in figure 7.2.

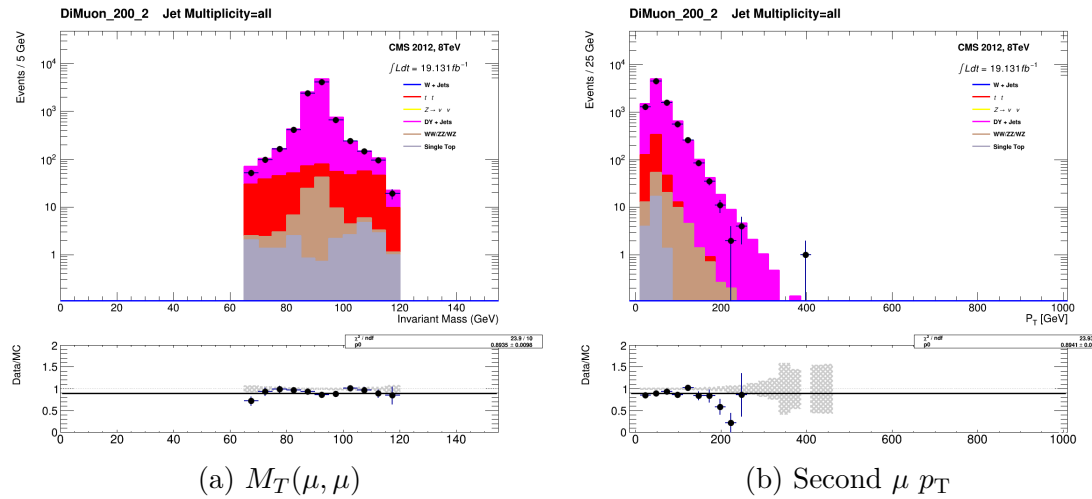


Fig. 7.2 Comparison of data with MC for the $\mu\mu+\text{jets}$ control selection. Plots are for $H_T > 200$ GeV, $n_{\text{jet}} \geq 2$, $n_b \geq 0$.

7.2.3 $\gamma+\text{jets}$

The $\gamma+\text{jets}$ sample is used to predict the $Z \rightarrow \nu\bar{\nu}$ background contribution, given it's similar kinematics when the γ is ignored from the event, and larger production cross section relative to $\mu\mu+\text{jets}$. Due to trigger thresholds, the $\gamma+\text{jets}$ sample cannot make predictions for $H_T < 375$ GeV, and so is complimentary to the $\mu\mu+\text{jets}$ sample prediction.

Triggers

Events are collected using the HLT_Photon150 trigger. The trigger's efficiency is measured using the HLT_Photon90 trigger as a reference and is found to be 100% efficient for $E_T^{photon} > 165\text{GeV}$ and $H_T > 375$ GeV, as shown by the turn on curves in figure 7.3.

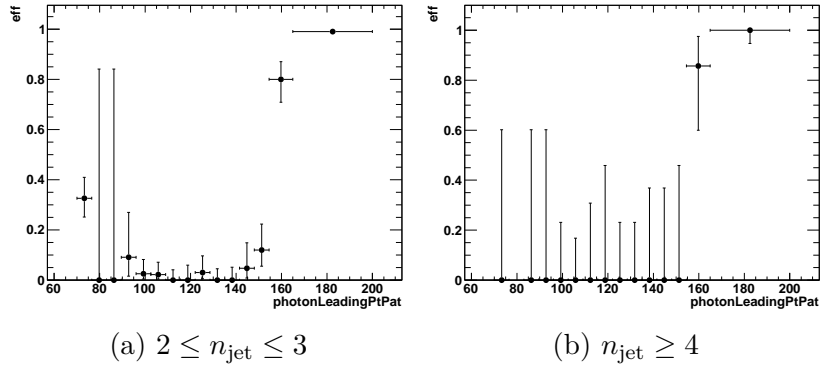


Fig. 7.3 Efficiency turn-on curves for the photon trigger, based on the $\gamma + \text{jets}$ selection, for $H_T > 375$ GeV, with $2 \leq n_{\text{jet}} \leq 3$ (Left) and $n_{\text{jet}} \geq 4$ (Right).

Selection Criteria

14

- ¹ Exactly one photon satisfying tight isolation criteria is required, with $p_T > 165$ GeV
² and $|\eta| < 1.45$. In addition, events are vetoed if $\Delta R(\gamma, \text{jet}_i) < 1.0$ is satisfied, for all
³ of the events i jets.

⁴ An example distribution of the γp_T for this selection is shown in figure 7.4.

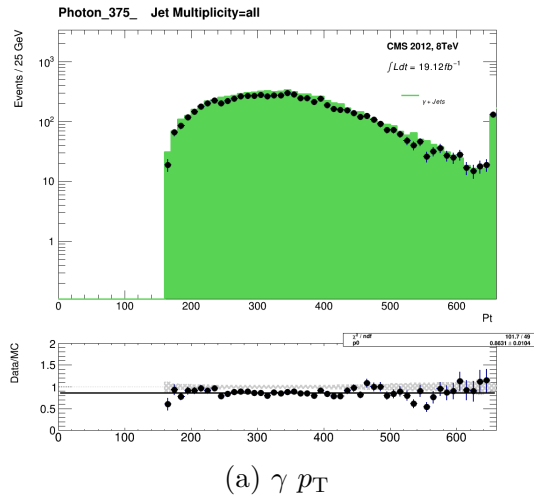


Fig. 7.4 Comparison of data with MC for the γ +jets control selection. Plot is for $H_T > 200$ GeV, $n_{\text{jet}} \geq 2, n_b \geq 0$.

⁵ 7.3 Background control and systematic uncertainties on SM background predictions ¹

In order to probe the levels at which the transfer factors are sensitive to relevant ² uncertainties, a statistically powerful ensemble of Closure Tests (CT's) have been ³ designed. The CT method works by constructing a TF to extrapolate from one sub- ⁴ region of a particular control sample into another control sample sub-region. In doing ⁵ so, tests can be designed to specifically probe any potential sources of bias in the ⁶ transfer factors. ⁷

7.3.1 Closure tests ⁸

Closure tests are performed as a function of H_T , in the two n_{jet} categories, $2 \leq n_{\text{jet}} \leq$ ⁹ 3 and $n_{\text{jet}} \geq 4$. The level of closure represents the statistical consistency between ¹⁰ predicted and observed yields for each test, in the absence of any assumed systematic ¹¹ uncertainty. The test statistic is defined as $(N_{\text{obs}} - N_{\text{pred}})/N_{\text{pred}}$, with any bias being ¹² observed as a statistically significant deviation from zero, or a trend in H_T . ¹³

Figure 7.5 shows a summary of the eight closure tests considered as ‘core’ tests for ¹⁴ the analysis, split into both $2 \leq n_{\text{jet}} \leq 3$ (figure 7.5a) and $n_{\text{jet}} \geq 4$ (figure 7.5b). It ¹⁵ should be noted that numerous other tests are also considered, but that these eight ¹⁶ represent those deemed most important to the background prediction uncertainty. ¹⁷

The first test, represented by open circles, tests the modelling of the α_T variable ¹⁸ in the $\mu + \text{jets}$ control sample. In the analysis a prediction is made between the $\mu + \text{jets}$ ¹⁹ sample, which has no α_T requirement, and the signal region, with its tight α_T requirement. ²⁰ This particular test probes the validity of predicting between the ‘bulk’ of the α_T ²¹ distribution in the control sample and the ‘tail’ of the distribution in the signal ²² region. A similar test, not shown here, is performed for the $\mu\mu + \text{jets}$ control sample. ²³

The next two tests, represented by crosses and open squares, probe the different b- ²⁴ tag multiplicities in the $\mu + \text{jets}$ control sample. The b-tag requirements greatly change ²⁵ the relative admixture of, for example, $W + \text{jets}$ ($n_b = 0$) and $t\bar{t} + \text{jets}$ ($n_b = 1$) events. ²⁶ It is important to note that this test is considered conservative, given that the admixture ²⁷ of $W + \text{jets}$ to $t\bar{t} + \text{jets}$ events varies minimally between control and signal regions, ²⁸ where this extrapolation is made in the analysis. Given the focus on b-tagging, these ²⁹ tests also investigate the modelling of b-quark jets in the simulated data. ³⁰

A similar test is made for the relative admixture of $Z(\nu\nu) + \text{jets}$ to $W + \text{jets}$ and ³¹

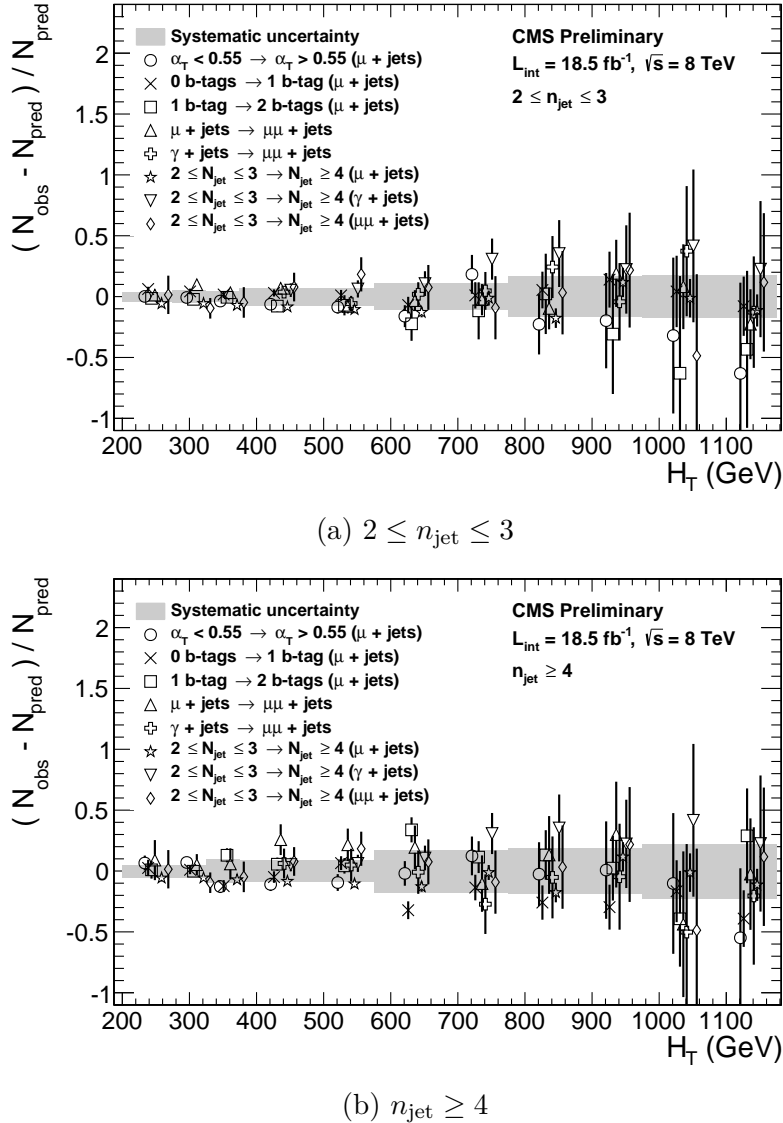


Fig. 7.5 The results of the eight core closure tests (open symbols), shown over the systematic uncertainty bands for each of the five H_T regions (shaded grey), for the two jet multiplicity regions (a) $2 \leq n_{\text{jet}} \leq 3$ and (b) $n_{\text{jet}} \geq 4$ separately.

$t\bar{t} + \text{jets}$, by predicting between the $\mu + \text{jets}$ and $\mu\mu + \text{jets}$ control regions, represented by open triangles. Again, this test is considered conservative, but also probes the muon reconstruction and trigger efficiencies between the different muon multiplicities. These are however already well studied by the muon POG using data-driven techniques.

As described in section 7.1, the $Z \rightarrow \nu\bar{\nu}$ prediction is made from both the $\gamma + \text{jets}$ and $\mu\mu + \text{jets}$ samples, and so a test is constructed to predict between these two or-

7.3 Background control and systematic uncertainties on SM background prediction⁸⁷

⁶ thogonal control regions, as shown by the open crosses.

The final three tests, indicated by open stars, triangles and diamonds, make predictions between the two different jet multiplicity categories in each control sample, thereby testing jet reconstruction and modelling. This test is also considered very conservative as the analysis only predicts between identical n_{jet} categories in the control and signal regions.

Summary plots of these eight tests are shown in figure 7.5, indicating that there are no statistically significant biases or H_T dependencies. Figures 7.6a and 7.6c show zeroeth order polynomial fits (blue lines) made to each individual test to assess the level of any potential bias present. In addition, first order polynomial fits (red lines) are also made to assess any potential H_T dependence present in the tests, as shown in figures 7.6b and 7.6d. The best-fit values, χ^2 and p -values obtained from both fits are summarised for each n_{jet} category in tables 7.4, 7.5 and 7.6.

As expected, the fits show no significant biases or trends, and therefore indicate good closure. The only exception is the 0 b-jets \rightarrow 1 b-jet ($\mu+\text{jets}$) test for the $n_{\text{jet}} \geq 4$ category which has a sub-optimal goodness of fit value. This is attributed to upwards and downwards fluctuations in the 475-575 GeV and 575-675 GeV bins respectively. Also shown in table 7.5, when the same fit is made after summing these two bins significantly improved fit parameters are observed. This leads to the conclusion that these two bins contain a statistical fluctuation as opposed to a systematic bias.

Table 7.4 Results of zeroeth (i.e. constant) and first order (i.e. linear) fits for five sets of closure tests, performed in the $2 \leq n_{\text{jet}} \leq 3$ category.

Closure test	Symbol	Constant fit			Linear fit	
		Best fit value	χ^2	d.o.f.	p -value	Slope (10^{-4})
$\alpha_T < 0.55 \rightarrow \alpha_T > 0.55 (\mu+\text{jets})$	Circle	-0.02 ± 0.01	11.3	10	0.34	-2.9 ± 1.1
0 b-jets \rightarrow 1 b-jet ($\mu+\text{jets}$)	Times	0.04 ± 0.01	5.8	10	0.83	-1.5 ± 0.9
1 b-jet \rightarrow 2 b-jets ($\mu+\text{jets}$)	Square	-0.03 ± 0.02	5.3	10	0.87	-3.0 ± 1.7
$\mu+\text{jets} \rightarrow \mu\mu+\text{jets}$	Triangle	0.03 ± 0.02	12.3	10	0.27	-1.3 ± 1.1
$\gamma+\text{jets} \rightarrow \mu\mu+\text{jets}$	Cross	-0.02 ± 0.03	3.0	7	0.88	0.0 ± 2.7

Table 7.5 Results of zeroeth (i.e. constant) and first order (i.e. linear) fits for five sets of closure tests, performed in the $2 \leq n_{\text{jet}} \leq 3$ category.

Closure test	Symbol	Constant fit			Linear fit	
		Best fit value	χ^2	d.o.f.	p -value	Slope (10^{-4})
$\alpha_T < 0.55 \rightarrow \alpha_T > 0.55 (\mu+\text{jets})$	Circle	-0.02 ± 0.02	17.6	10	0.06	-3.1 ± 1.7
0 b-jets \rightarrow 1 b-jet ($\mu+\text{jets}$)	Times	-0.06 ± 0.02	31.2	10	0.00	-4.1 ± 1.2
0 b-jets \rightarrow 1 b-jet ($\mu+\text{jets}$) [†]	Times	-0.05 ± 0.02	13.4	9	0.15	-3.9 ± 1.3
1 b-jet \rightarrow 2 b-jets ($\mu+\text{jets}$)	Square	0.06 ± 0.02	13.7	10	0.19	2.5 ± 1.6
$\mu+\text{jets} \rightarrow \mu\mu+\text{jets}$	Triangle	0.11 ± 0.05	4.8	10	0.90	0.4 ± 2.7
$\gamma+\text{jets} \rightarrow \mu\mu+\text{jets}$	Cross	-0.00 ± 0.07	2.3	7	0.94	-5.3 ± 4.7

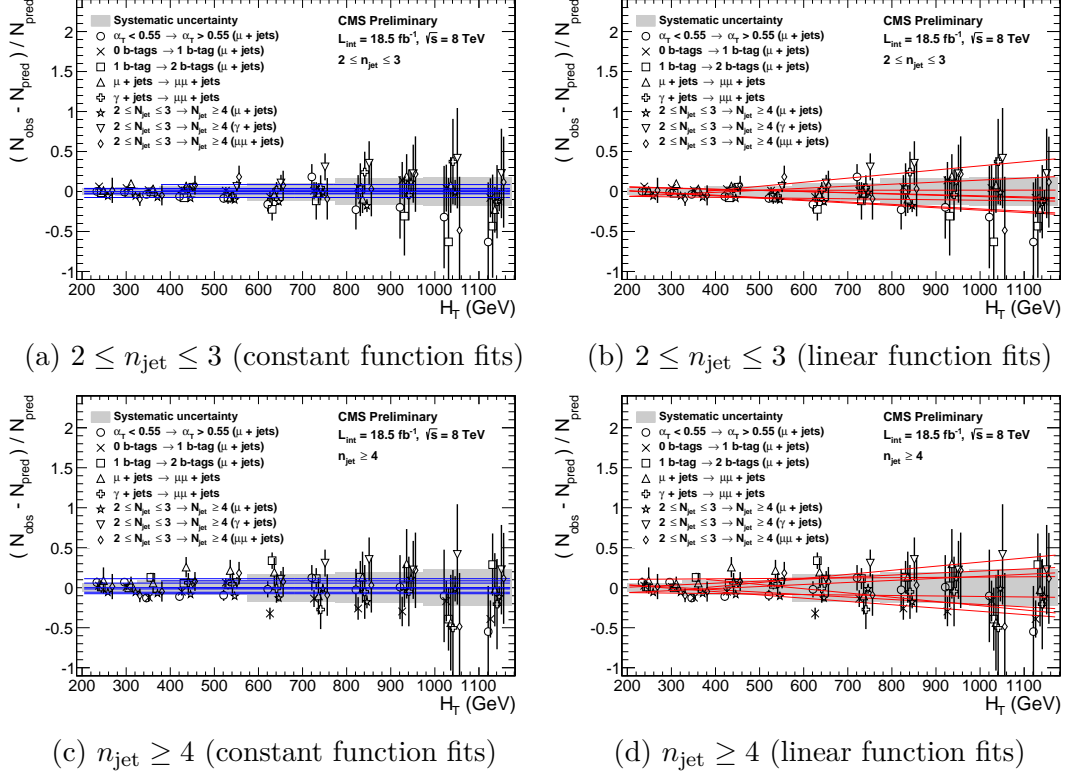


Fig. 7.6 The results of the eight core closure tests (open symbols), shown over the systematic uncertainty bands for each of the five H_T regions (shaded grey), for the two jet multiplicity regions (a) $2 \leq n_{\text{jet}} \leq 3$ and (b) $n_{\text{jet}} \geq 4$ separately. Included are zeroeth order (left column, blue) and first order (right column, red) fits to each individual closure test.

Table 7.6 Results of zeroeth (i.e. constant) and first order (i.e. linear) fits for the three sets of closure tests probing the accuracy of jet multiplicity modelling in MC, for each control sample.

Sample	Symbol	Constant fit				Linear fit	
		Best fit value	χ^2	d.o.f.	p-value	Slope (10^{-4})	p-value
$\mu + \text{jets}$	Star	-0.08 ± 0.01	9.3	10	0.50	0.6 ± 0.7	0.48
$\gamma + \text{jets}$	Inverted triangle	0.09 ± 0.04	3.7	7	0.82	5.1 ± 3.2	0.98
$\mu\mu + \text{jets}$	Diamond	-0.00 ± 0.05	4.7	10	0.91	2.5 ± 2.9	0.92

7.3.2 Background systematic uncertainty summary

20

- ¹ Under the assumption of closure for the eight core tests, systematic errors are derived
- ² for each n_{jet} category in seven regions of H_T . Values are calculated by summing in
- ³ quadrature the weighted mean and sample variance for all eight tests in a given H_T

 7.3 Background control and systematic uncertainties on SM background prediction **89**

⁴ region. These values are summarised in table 7.7 and also in the summary plots of figure 7.5, shown as grey bands.

Table 7.7 Summary of the magnitude of systematic uncertainties (%) derived from the eight core closure tests, for each n_{jet} category and H_T region.

n_{jet}	H_T region (GeV)						
	200–275	275–325	325–375	375–575	575–775	775–975	> 975
2–3	4	6	6	8	12	17	19
≥ 4	6	6	11	11	18	20	26

Systematic values are considered as fully uncorrelated between the different analysis categories and the H_T regions, which is again considered as a conservative approach given that some correlation is to be expected, for example between adjacent H_T bins.

Chapter 8

5

Results

1

8.1 Likelihood Model

2

The likelihood is defined for each analysis category of n_b and n_{jet} as follows.

3

8.1.1 Hadronic Signal Region

4

Let n^i be the observed number of events following full selection in the i^{th} of N bins of H_T . The likelihood is constructed as:

5

6

$$L_{hadronic} = \prod_i \text{Pois}(n^i | b^i + s^i), \quad (8.1) \quad 7$$

where b^i and s^i represent the expected number of background events from SM processes and the expected number of signal events in the bin i . Pois is the Poisson distribution:

8

9

$$f(k; \lambda) = \frac{1}{k!} \lambda^k e^{-\lambda}. \quad (8.2) \quad 10$$

8.1.2 Electroweak Background Contribution

11

The background is considered to be entirely EWK in origin ($b^i = \text{EWK}^i$), as QCD is made negligible, so can be deconstructed using the relative fraction of $Z \rightarrow \nu\bar{\nu}$ events, f_{Zinv} as:

12

13

14

$$Z_{inv}^i = f_{Zinv} \times \text{EWK}^i, \quad (8.3) \quad 15$$

16

$$\text{ttW}^i = (1 - f_{Zinv}) \times \text{EWK}^i, \quad (8.4) \quad 17$$

where EWK^i is number of expected events from the total EWK background, Z_{inv}^i is the number of expected events from the $Z \rightarrow \nu\bar{\nu}$ contribution and ttW^i is the number of expect events from the W boson production and top quark decay contribution, all in the i^{th} bin. The variable $f_{Z_{\text{inv}}}$ is allowed to float between 0 and 1.

EWK backgrounds are predicted using sideband control samples and transfer factors (chapter 7). Let n_γ^i , n_μ^i and $n_{\mu\mu}^i$ be the observed event counts in the $\gamma+\text{jets}$, $\mu+\text{jets}$ and $\mu\mu+\text{jets}$ control samples, respectively, with corresponding yields in MC: MC_γ^i , MC_μ^i , $MC_{\mu\mu}^i$. These are further seperated into seperate contributions from $Z \rightarrow \nu\bar{\nu}$, $MC_{Z_{\text{inv}}}$, and ttW , $MC_{t\bar{t}+W}$. Transfer factors are defined as the inverse as those of the analysis:

$$r_\gamma^i = \frac{MC_\gamma^i}{MC_{Z_{\text{inv}}}}, \quad r_{\mu\mu}^i = \frac{MC_{\mu\mu}^i}{MC_{Z_{\text{inv}}}}, \quad r_\mu^i = \frac{MC_\mu^i}{MC_{t\bar{t}+W}}, \quad (8.5)$$

and so likelihoods are written as:

$$L_\gamma = \prod_i \text{Pois}(n_\gamma^i | \rho_{\gamma Z}^j \cdot r_\gamma^i \cdot Z_{\text{inv}}^i), \quad (8.6)$$

$$L_{\mu\mu} = \prod_i \text{Pois}(n_{\mu\mu}^i | \rho_{\mu\mu Z}^j \cdot r_{\mu\mu}^i \cdot Z_{\text{inv}}^i), \quad (8.7)$$

$$L_\mu = \prod_i \text{Pois}(n_\mu^i | \rho_{\mu W}^j \cdot r_\mu^i \cdot ttW^i + s_\mu^i). \quad (8.8)$$

Both equations 8.6 and 8.7 are used to estimate the maximum likelihood value for Z_{inv}^i , alongside equation 8.8 for ttW^i , all considered simultaneously through the relationships defined in equations 8.3 and 8.4.

The terms $\rho_{\gamma Z}^j$, $\rho_{\mu\mu Z}^j$ and $\rho_{\mu W}^j$ are correction factors accomodating the systematic uncertainties associated with the control sample based background predictions. The relative uncertainties are derived in section 7.3.1 and represented by the terms $\sigma_{\gamma Z}^j$, $\sigma_{\mu\mu Z}^j$ and $\sigma_{\mu W}^j$, their values summarised in table 7.7. Systematics enter the total likelihood as:

$$L_{\gamma \text{ syst.}} = \prod_j \text{Logn}(1.0 | \rho_{\gamma Z}^j, \sigma_{\gamma Z}^j), \quad (8.9)$$

$$L_{\mu\mu \text{ syst.}} = \prod_j \text{Logn}(1.0 | \rho_{\mu\mu Z}^j, \sigma_{\mu\mu Z}^j), \quad (8.10)$$

8.1 Likelihood Model

28

$$L_{\mu \text{ syst.}} = \prod_j \text{Logn}(1.0 | \rho_{\mu W}^j, \sigma_{\mu W}^j), \quad (8.11) \quad 1$$

where Logn is the log-normal distribution (as recommended by [64]):

$$\text{Logn}(x|\mu, \sigma) = \frac{1}{x\sqrt{2\pi}\ln k} \exp\left(-\frac{\ln^2\left(\frac{x}{\mu}\right)}{2\ln^2 k}\right); k = 1 + \sigma \quad (8.12) \quad 3$$

These terms are combined as:

$$L_{EWK \text{ syst.}} = L_{\gamma \text{ syst.}} \times L_{\mu\mu \text{ syst.}} \times L_{\mu \text{ syst.}} \quad (8.13) \quad 5$$

For $n_b \geq 2$ categories, the μ +jets control sample is used to predict $Z \rightarrow \nu\bar{\nu}$ and ttW combined, giving:

$$r_{\mu}^{i*} = \frac{MC_{\mu}^i}{MC_{t\bar{t}+W+Z_{\text{inv}}}^i}; \quad (8.14) \quad 8$$

$$L_{\mu} = \prod_i \text{Pois}(n_{\mu}^i | \rho_{\mu W}^j \cdot r_{\mu}^{i*} \cdot EWK^i + s_{\mu}^i). \quad (8.15) \quad 10$$

Terms corresponding to the $\mu\mu$ +jets and γ +jets samples are subsequently dropped.

8.1.3 Signal Contribution

Let x be the cross section of the signal model under test, which can be varied according to a multiplicative factor f (a.k.a. the “mu-factor”), and l be the luminosity of the relevant collected data sample. ϵ_{had}^i and ϵ_{μ}^i are the signal acceptances of the hadronic and muon selections, respectively, for the given signal model. Finally, let δ be the relative systematic uncertainty on that signal acceptance, and ρ_{sig} be the corrective factor to the signal yield floated to accomodate this uncertainty. Therefore the yield of signal events for the hadronic sample, s^i , and the yield of signal in the muon sample (i.e. “signal contamination”), s_{μ}^i , can be written as:

$$s^i = f \rho_{sig} x l \epsilon_{had} \quad (8.16) \quad 21$$

$$s_{\mu}^i = f \rho_{sig} x l \epsilon_{\mu} \quad (8.17) \quad 23$$

Furthermore, the signal systematic contribution to the likelihood is included as the ²⁴
term:

$$L_{signal} = \text{Logn}(1.0 | \rho_{sig}, \delta) \quad (8.18)$$

3 8.1.4 Total Likelihood

4 For a given analysis category k (n_b , n_{jet}), the total likelihood is constructed as:

$$5 L_{total}^k = L_{hadronic}^k \times L_\mu^k \times L_\gamma^k \times L_{\mu\mu}^k \times L_{EWK \text{ syst.}}^k \quad (8.19)$$

6 The number of nuisance parameters varies between different analysis categories, depen-
7 dent on the number of H_T bins and control samples, summarised in table 8.1.

Table 8.1 Summary of likelihood nuisance parameters.

Description	Categories	Nuisance Parameters
11 H_T bins, $(\mu, \mu\mu, \gamma)$	$2 \leq n_{jet} \leq 3/n_{jet} \geq 4$, $n_b = 0, 1$	$\{EWK^i, f_{Zinv}\}_{i=0}^{10}, \{\rho_{\gamma Z}^j\}_{j=3}^6, \{\rho_{\mu\mu Z}^j, \rho_{\mu W}^j\}_{j=0}^6$
8 H_T bins, (μ)	$2 \leq n_{jet} \leq 3/n_{jet} \geq 4$, $n_b = 2, 3, >4$	$\{EWK^i, f_{Zinv}\}_{i=0}^8, \{\rho_{\mu WZ}^j\}_{j=0}^6$
3 H_T bins, (μ)	$2 \leq n_{jet} \leq 3/n_{jet} \geq 4$, $n_b = 2, 3, >4$	$\{EWK^i\}_{i=0}^3, \{\rho_{\mu WZ}^j\}_{j=0}^6$

8 When considering signal an additional term is introduced:

$$9 L = L_{signal} \times \prod_k L_{total}^k \quad (8.20)$$

10 8.2 Fit Results

11 The likelihood model described in section 8.1 is used to relate the observations in
12 the signal and control samples, accomodate the calculated background systematic
13 uncertainties, and allow for the presence of any potential signal. In order to test the
14 compatibility with a Standard Model only hypothesis, signal contribution is set to zero
15 and the likelihood is maximized over all parameters using ROOFIT [65] and MINUIT
16 [66], for each analysis category of n_b and n_{jet} .

17 Uncertainties are determined by performing a number of pseudo-experiments for
18 each (n_b, n_{jet}) category and H_T bin, with the fit yields being put into a histogram,
19 appropriate quantiles taken, using their difference from the maximum likelihood (ML)
20 value taken as the fit uncertainty value.

²¹ Two different procedures are used to determine fits to observations, as described
in the following sections.
¹

8.2.1 Fit without Signal region

An “a priori” fit is made by considering only yields from the control samples, and not
data observations in the hadronic signal region. The results of this fit are shown in
figs. 8.2 to 8.3 and 8.5 to 8.9 and summarised in tabular form in table 8.3.
²
³
⁴
⁵

Table 8.2 Summary of the “a posteriori” fit.

n_{jet}	n_b	H_T (GeV)							
2-3	0	SM	200-275	275-325	325-375	375-475	475-575	575-675	675-775
2-3	0	Data	13034 ⁺⁸⁹ ₋₁₁₇	5348 ⁺⁵⁵ ₋₆₇	3351 ⁺³⁶ ₋₅₀	2351 ⁺³⁸ ₋₄₅	655 ⁺¹⁴ ₋₁₁	218 ⁺¹² ₋₁₇	68.5 ^{+4.9} _{-4.8}
2-3	1	SM	1711 ⁺³⁷ ₋₃₃	839 ⁺²¹ ₋₂₅	526 ⁺²⁰ ₋₁₇	372 ⁺¹² ₋₁₄	90.6 ^{+5.1} _{-4.6}	25.8 ^{+2.9} _{-2.6}	8.7 ^{+0.8} _{-1.4}
2-3	1	Data	1733	833	527	356	90	31	6
2-3	2	SM	184 ⁺⁵ ₋₇	117 ⁺⁷ ₋₅	99.4 ^{+5.4} _{-4.6}	60.2 ^{+3.5} _{-3.8}	12.4 ^{+1.2} _{-1.0}	3.3 ^{+0.6} _{-0.5}	0.7 ^{+0.2} _{-0.2}
2-3	2	Data	172	116	101	55	16	9	0
≥ 4	0	SM	104 ⁺⁶ ₋₈	544 ⁺²¹ ₋₁₈	407 ⁺¹⁸ ₋₁₈	337 ⁺¹⁵ ₋₁₀	202 ⁺¹⁰ ₋₈	105 ⁺⁹ ₋₇	42.5 ^{+4.5} _{-3.3}
≥ 4	0	Data	99	568	408	336	211	117	38
≥ 4	1	SM	38.9 ^{+2.2} _{-3.7}	206 ⁺¹² ₋₁₀	209 ⁺¹³ ₋₁₀	157 ⁺⁹ ₋₉	79.3 ^{+5.2} _{-4.7}	29.4 ^{+3.8} _{-2.2}	9.9 ^{+1.9} _{-1.3}
≥ 4	1	Data	38	195	210	159	83	33	7
≥ 4	2	SM	12.5 ^{+1.0} _{-1.0}	77.8 ^{+4.7} _{-4.6}	90.2 ^{+9.0} _{-6.5}	66.1 ^{+4.6} _{-4.8}	36.3 ^{+3.4} _{-2.9}	11.4 ^{+1.8} _{-1.9}	3.9 ^{+0.8} _{-0.7}
≥ 4	2	Data	16	81	88	64	43	14	5
≥ 4	3	SM	1.1 ^{+0.2} _{-0.2}	8.1 ^{+0.9} _{-0.9}	9.9 ^{+1.5} _{-1.3}	7.2 ^{+0.9} _{-0.7}	4.1 ^{+0.6} _{-0.6}	1.1 ^{+0.3} _{-0.3}	0.4 ^{+0.1} _{-0.1}
≥ 4	3	Data	0	7	5	5	6	1	1
≥ 4	≥ 4	SM	0.0 ^{+0.0} _{-0.0}	0.1 ^{+0.1} _{-0.1}	0.4 ^{+0.2} _{-0.3}	0.4 ^{+0.2} _{-0.2}	0	2	0
≥ 4	≥ 4	Data	0	0	0	0	0	0	0

¹ 8.2.2 Fit with Signal region

An “a posteriori” fit is made by considering every region, including the hadronic signal region observation in data, and is shown in figs. 8.2 to 8.3 and 8.5 to 8.9 and summarised in table 8.2.

¹
²
³

Table 8.3 Summary of the “a priori” fit.

n_{jet}	n_b	H_T (GeV)							
2-3	0	SM	200-275	275-325	325-375	375-475	475-575	575-675	675-775
2-3	0	Data	12412 ⁺³⁶⁹ ₋₄₁₂	5535 ⁺³³⁸ ₋₂₃₄	3331 ⁺¹²⁶ ₋₁₆₇	2400 ⁺¹²² ₋₉₄	663 ⁺³⁴ ₋₂₆	225 ⁺²¹ ₋₁₇	68.5 ^{+6.9} _{-6.7}
2-3	1	SM	1669 ⁺⁶⁵ ₋₆₇	853 ⁺⁵⁰ ₋₄₆	525 ⁺³⁷ ₋₂₄	391 ⁺²³ ₋₂₁	94.3 ^{+6.0} _{-5.6}	24.5 ^{+2.5} _{-3.6}	9.0 ^{+1.2} _{-1.4}
2-3	1	Data	1733	833	527	356	90	31	6
2-3	2	SM	187 ⁺⁷ ₋₈	118 ⁺⁷ ₋₇	98.7 ^{+7.1} _{-7.0}	61.3 ^{+5.9} _{-5.5}	12.3 ^{+1.7} _{-1.0}	2.8 ^{+0.5} _{-0.6}	0.7 ^{+0.2} _{-0.2}
2-3	2	Data	172	116	101	55	16	9	0
≥ 4	0	SM	108 ⁺¹⁰ ₋₁₂	497 ⁺³⁴ ₋₃₆	403 ⁺³⁶ ₋₃₃	327 ⁺²⁵ ₋₂₂	193 ⁺¹⁴ ₋₁₃	94.6 ^{+13.0} _{-10.7}	40.3 ^{+5.9} _{-4.4}
≥ 4	0	Data	99	568	408	336	211	117	38
≥ 4	1	SM	39.2 ^{+3.0} _{-3.5}	215 ⁺¹² ₋₁₆	208 ⁺²⁴ ₋₂₂	150 ⁺¹⁵ ₋₁₁	75.8 ^{+7.8} _{-6.6}	28.6 ^{+3.8} _{-3.7}	10.3 ^{+2.1} _{-1.4}
≥ 4	1	Data	38	195	210	159	83	33	7
≥ 4	2	SM	12.3 ^{+1.0} _{-1.0}	76.7 ^{+5.6} _{-5.2}	92.6 ^{+11.0} _{-9.3}	63.0 ^{+7.8} _{-5.7}	34.0 ^{+3.6} _{-3.4}	10.1 ^{+2.6} _{-1.8}	3.4 ^{+0.9} _{-0.6}
≥ 4	2	Data	16	81	88	64	43	14	5
≥ 4	3	SM	1.1 ^{+0.2} _{-0.1}	8.2 ^{+0.6} _{-0.9}	11.1 ^{+2.0} _{-1.6}	7.4 ^{+1.1} _{-1.0}	4.0 ^{+0.5} _{-0.6}	1.1 ^{+0.3} _{-0.3}	0.4 ^{+0.2} _{-0.1}
≥ 4	3	Data	0	7	5	6	1	1	0
≥ 4	≥ 4	SM	0.0 ^{+0.0} _{-0.0}	0.2 ^{+0.1} _{-0.1}	0.5 ^{+0.3} _{-0.3}	0.3 ^{+0.2} _{-0.2}	2	0	0
≥ 4	≥ 4	Data	0	0	0	0	2	0	0

8.2 Fit Results

1 8.2.3 Pulls and p-values

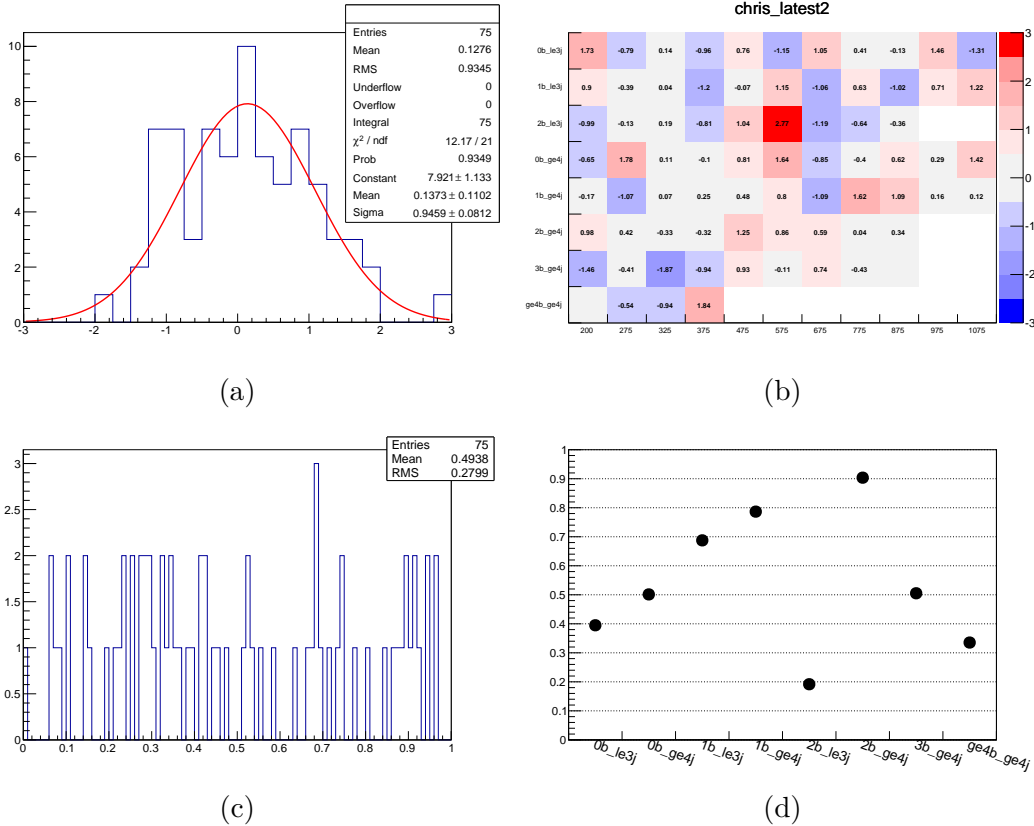


Fig. 8.1 Pulls and pvalues

Pulls are defined as DEFINITION(!), (wilk's theorem etc.). A p-value is calculated as the quantile of the distribution of maximised likelihood values for an ensemble of pseudo-experiments. Figure 8.1 summarises the distributions of these two values.

The 1D distribution of the pulls is shown in figure 8.1a, with a Gaussian fit (red) indicating good Gaussian behaviour, with mean and sigma values statistically significant with 0 and 1, respectively. Furthermore, the distribution of the esepulls as a function of the H_T bin and the analysis category (n_b , n_{jet}) is shown in figure 8.1b to be randomly distributed, with no apparent pattern to a given region.

The distribution of p-values for every bin of H_T and analysis category can be seen in figure 8.1c to be uniformly distributed between 0 and 1. The same information is shown in figure 8.1d when a single p-value is calculated for an entire H_T range, for each analysis category, where the lowest value is 0.19.

These tests indicate no significant excesses, and that all observations are compatible

with statistical fluctuations.

14

8.2 Fit Results

101

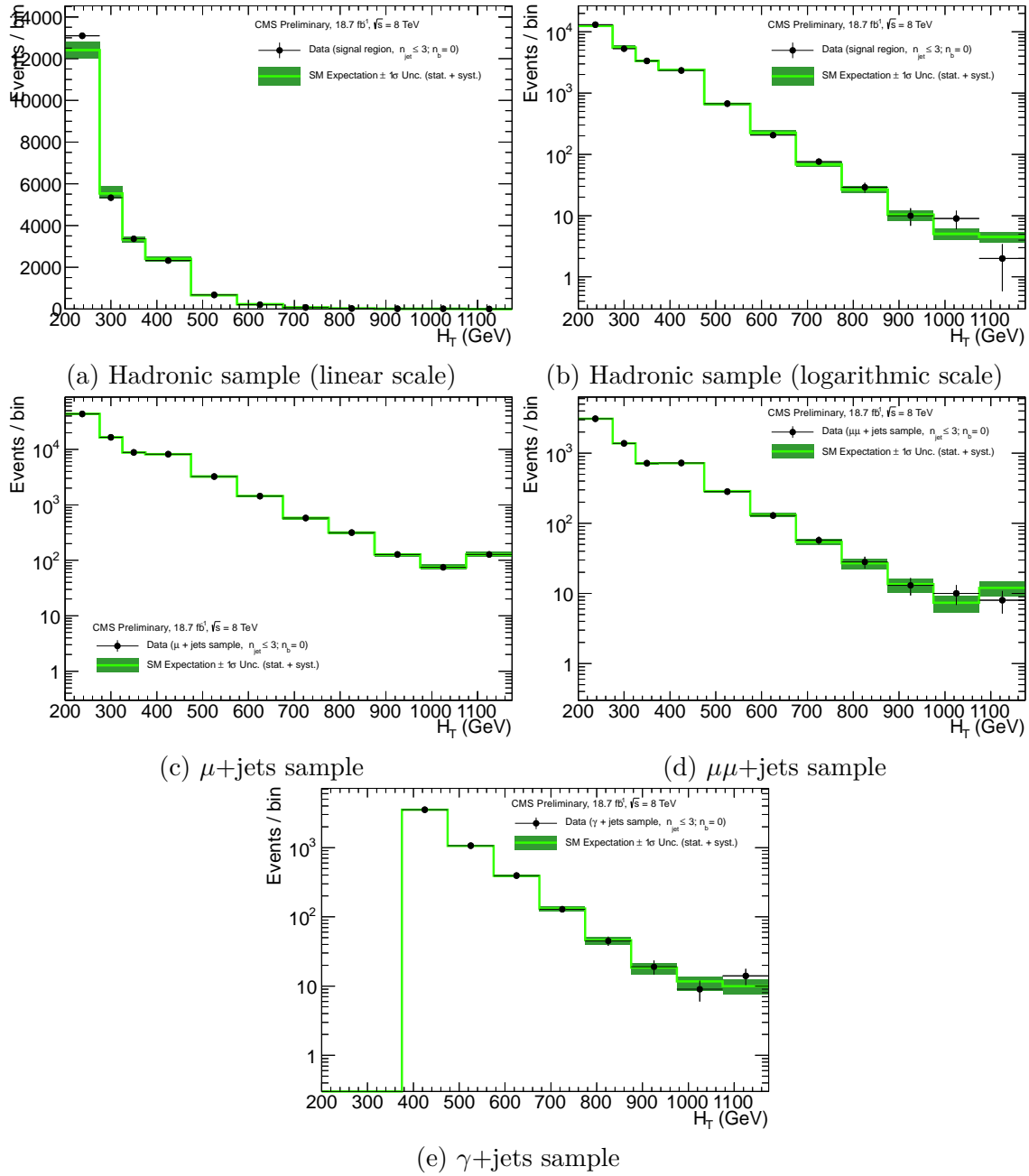


Fig. 8.2 Observations in data for the various signal and control regions in the analysis, compared to the result of the full likelihood model simultaneous fit, when the hadronic data observations are not considered. The plots are for the $2 \leq n_{\text{jet}} \leq 3, n_b = 0$ analysis category.

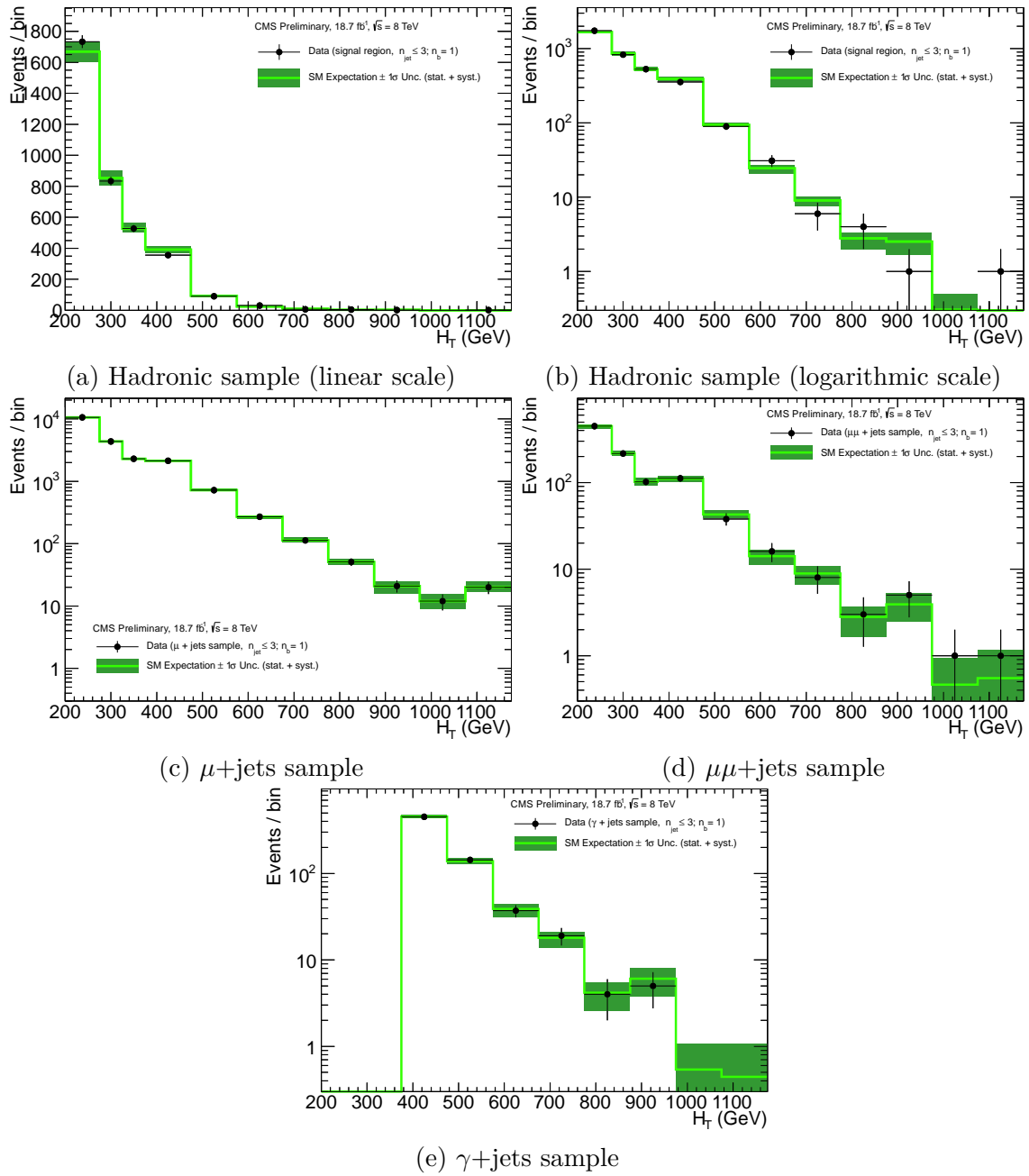


Fig. 8.3 Observations in data for the various signal and control regions in the analysis, compared to the result of the full likelihood model simultaneous fit, when the hadronic data observations are not considered. The plots are for the $2 \leq n_{\text{jet}} \leq 3, n_b = 1$ analysis category.

8.2 Fit Results

103

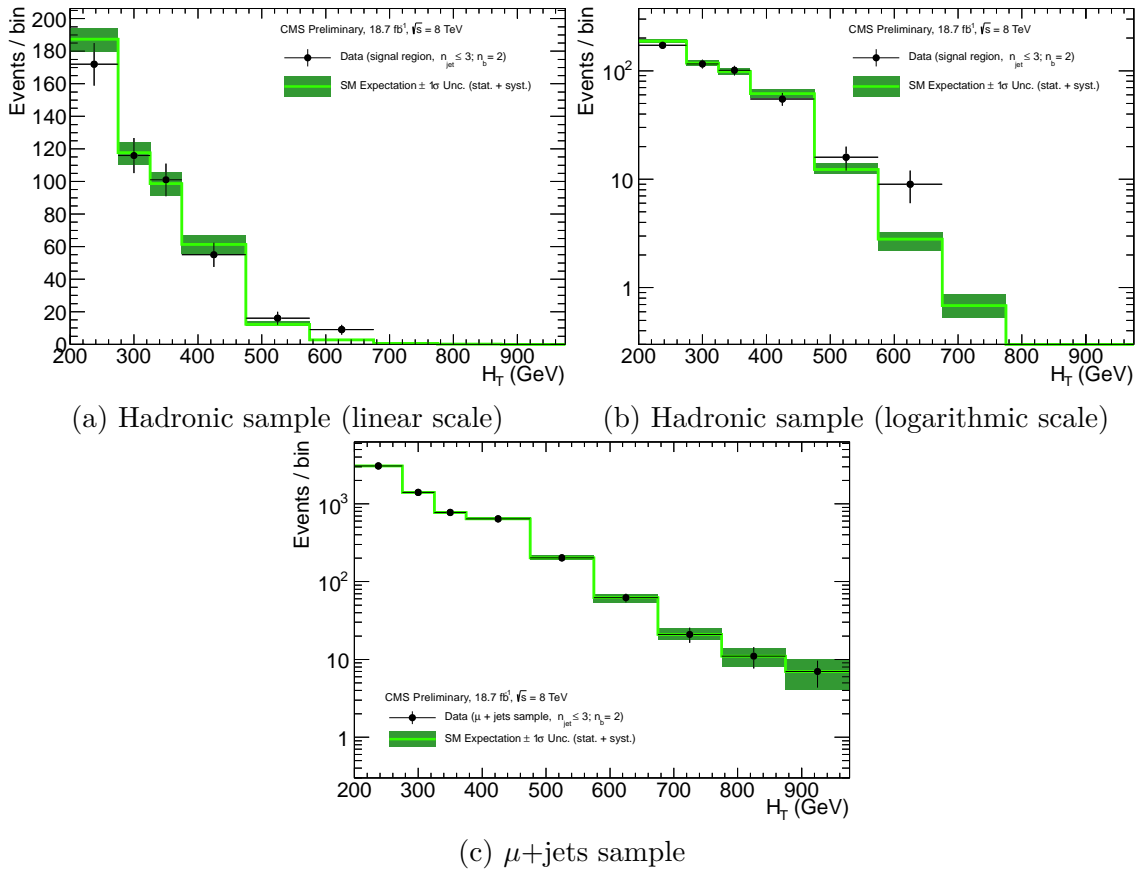


Fig. 8.4 Observations in data for the various signal and control regions in the analysis, compared to the result of the full likelihood model simultaneous fit, when the hadronic data observations are not considered. The plots are for the $2 \leq n_{\text{jet}} \leq 3, n_b = 2$ analysis category.

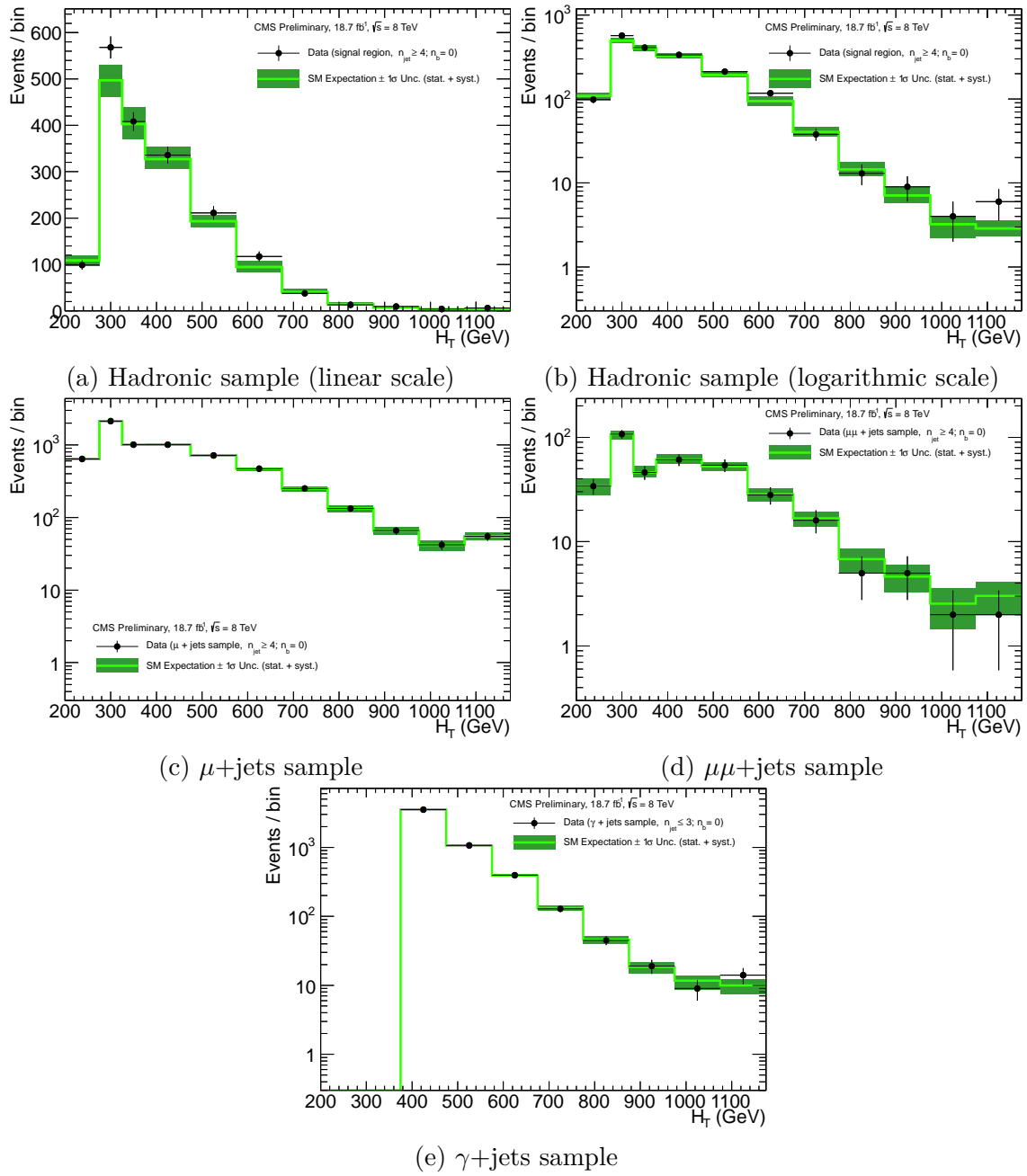


Fig. 8.5 Observations in data for the various signal and control regions in the analysis, compared to the result of the full likelihood model simultaneous fit, when the hadronic data observations are not considered. The plots are for the $n_{\text{jet}} \geq 4$, $n_b = 0$ analysis category.

8.2 Fit Results

105

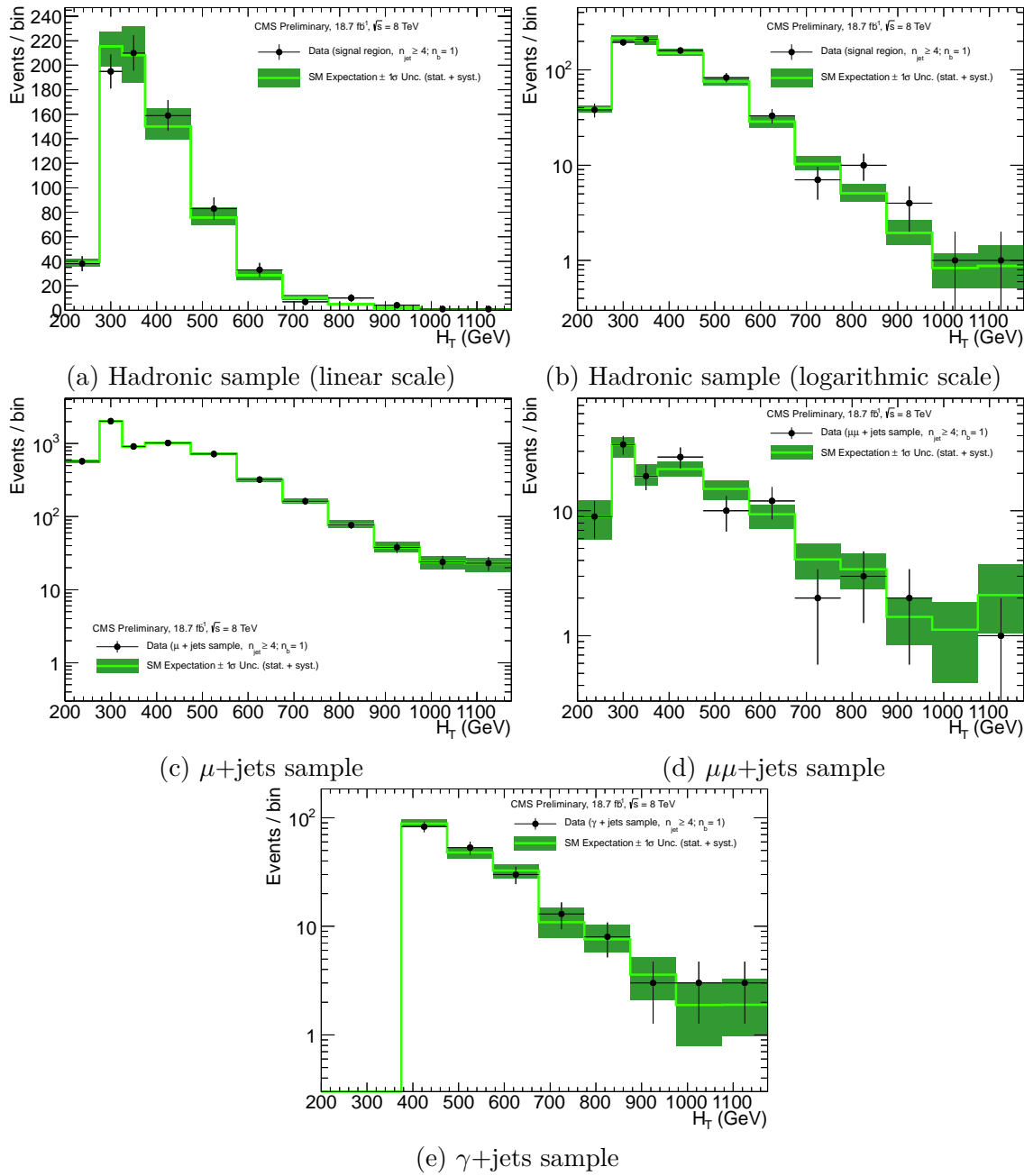


Fig. 8.6 Observations in data for the various signal and control regions in the analysis, compared to the result of the full likelihood model simultaneous fit, when the hadronic data observations are not considered. The plots are for the $n_{\text{jet}} \geq 4, n_b = 1$ analysis category.

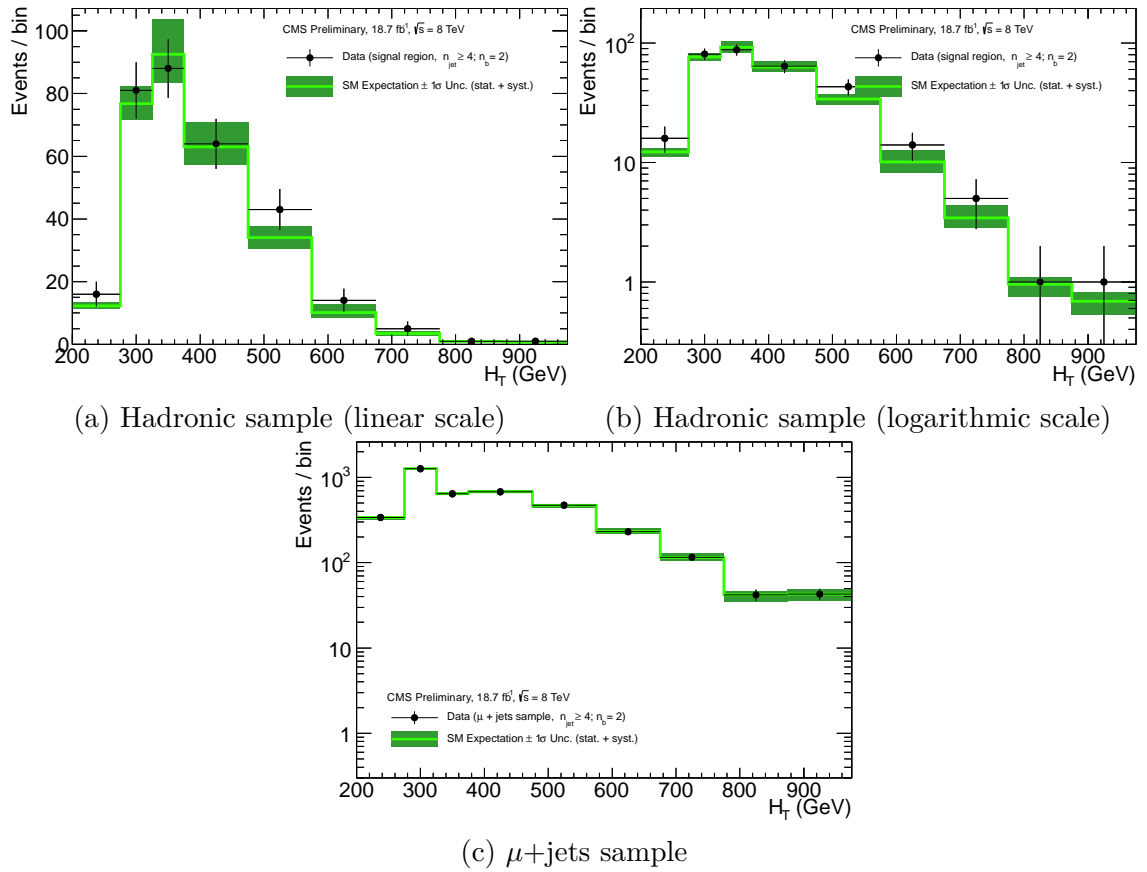


Fig. 8.7 Observations in data for the various signal and control regions in the analysis, compared to the result of the full likelihood model simultaneous fit, when the hadronic data observations are not considered. The plots are for the $n_{\text{jet}} \geq 4$, $n_b = 2$ analysis category.

8.2 Fit Results

107

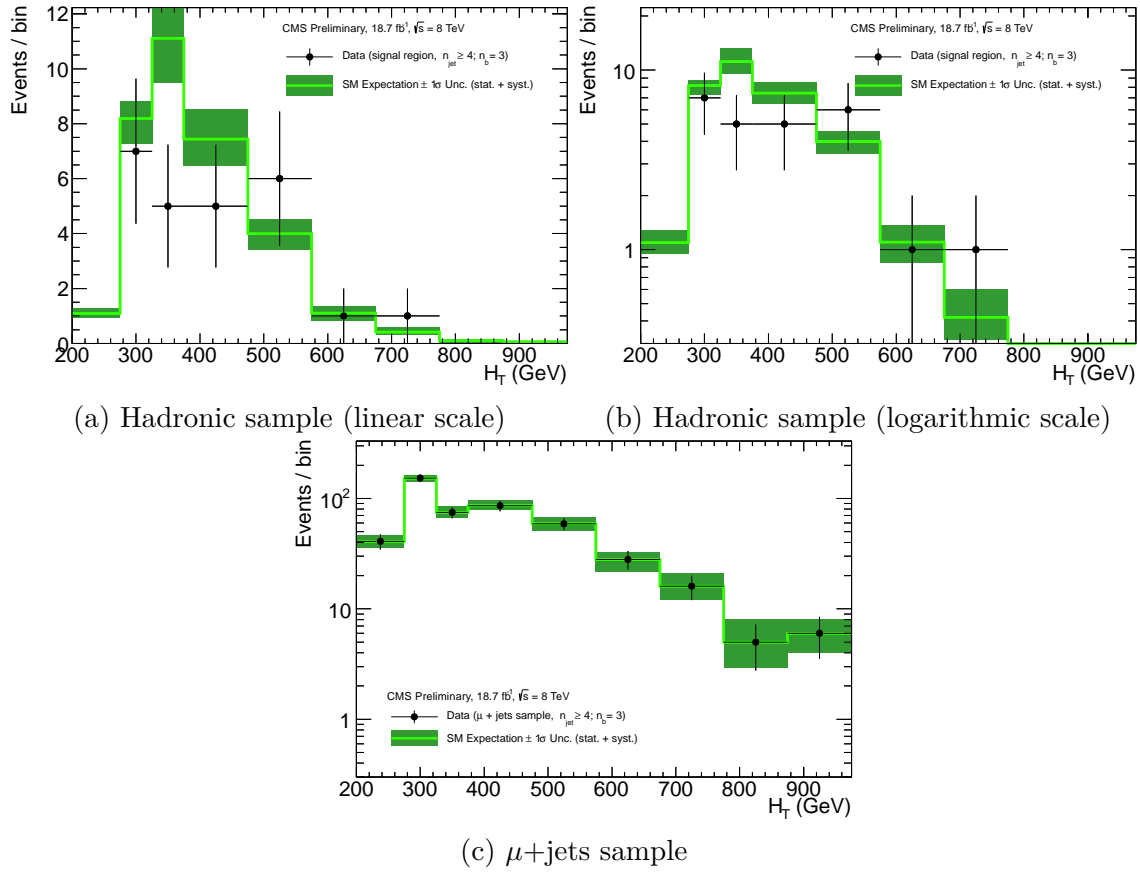


Fig. 8.8 Observations in data for the various signal and control regions in the analysis, compared to the result of the full likelihood model simultaneous fit, when the hadronic data observations are not considered. The plots are for the $n_{\text{jet}} \geq 4$, $n_b = 3$ analysis category.

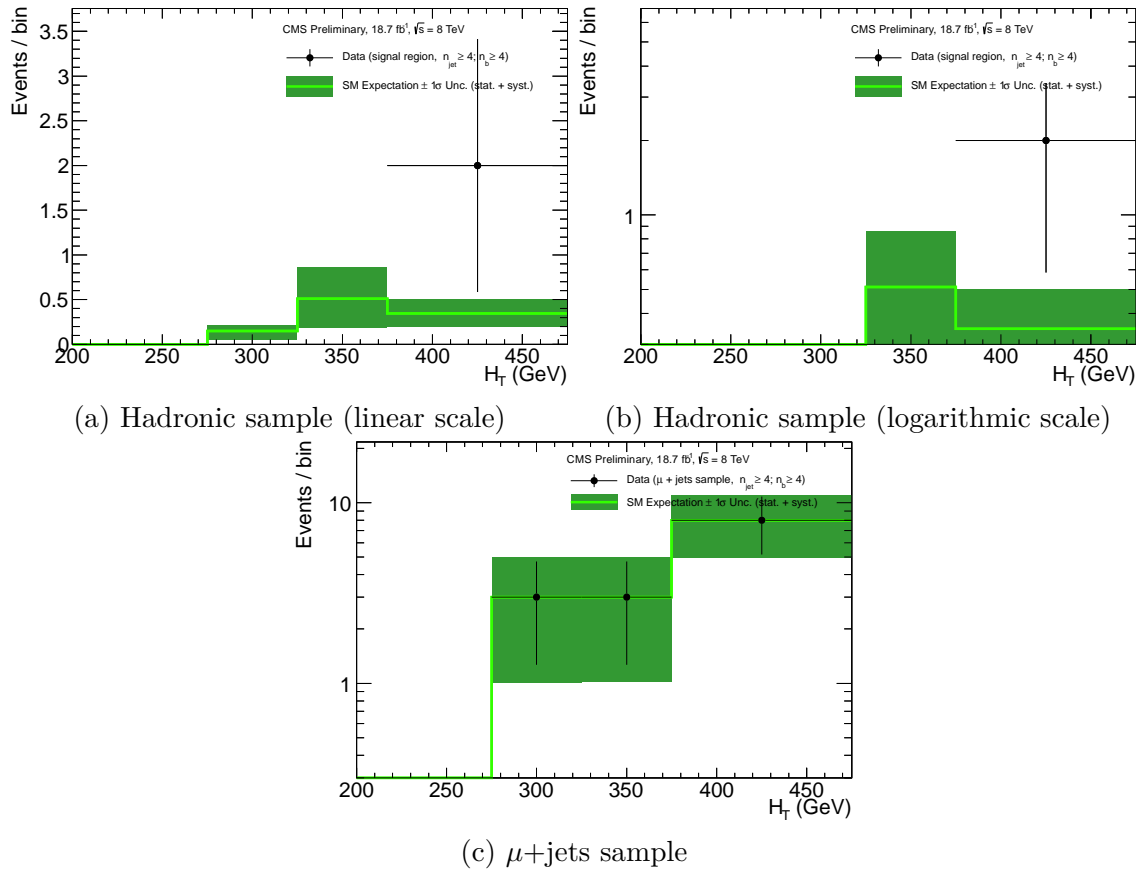


Fig. 8.9 Observations in data for the various signal and control regions in the analysis, compared to the result of the full likelihood model simultaneous fit, when the hadronic data observations are not considered. The plots are for the $n_{jet} \geq 4, n_b \geq 4$ analysis category.

8.2 Fit Results

109

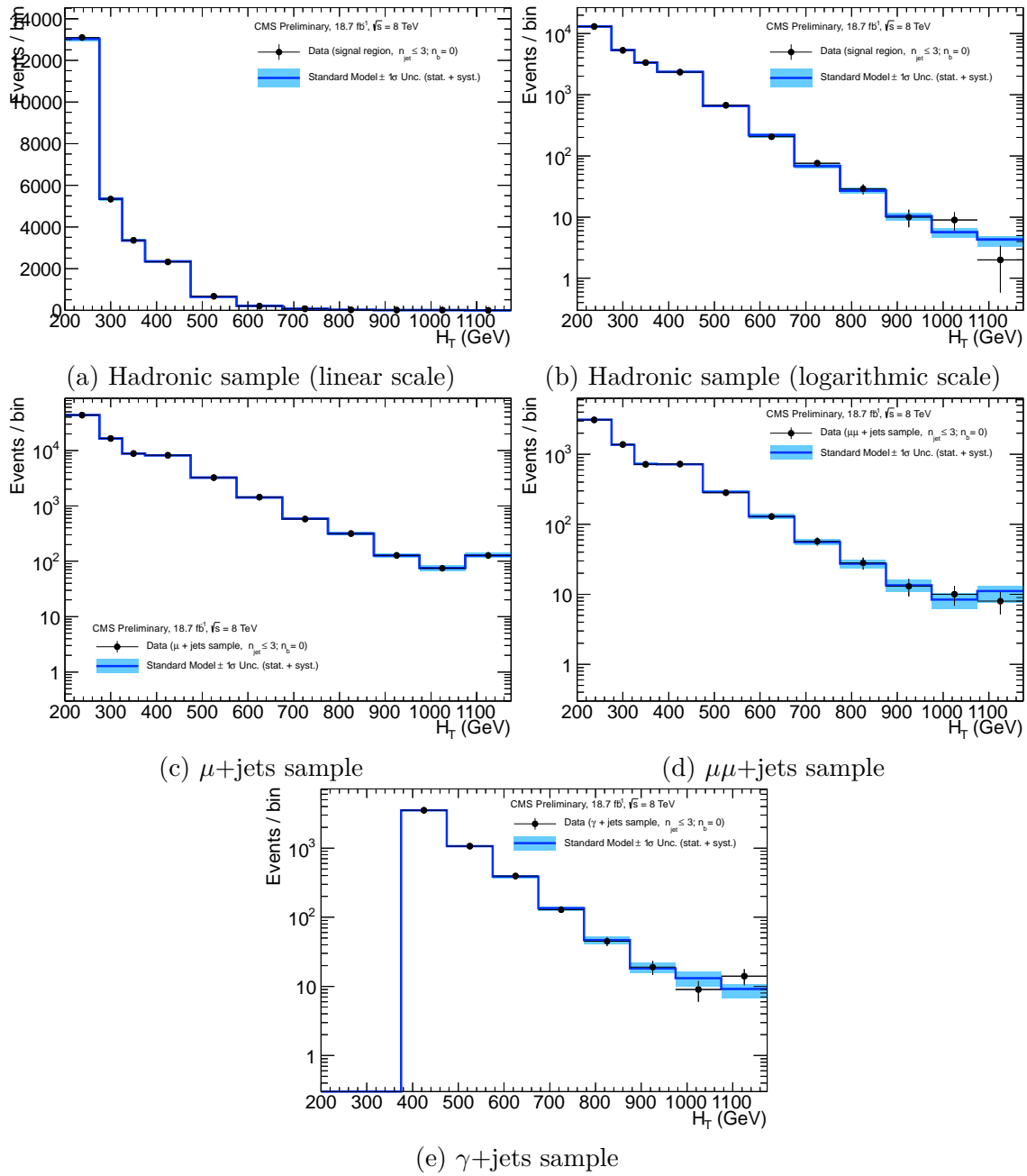


Fig. 8.10 Observations in data for the various signal and control regions in the analysis, compared to the result of the full likelihood model simultaneous fit. The plots are for the $2 \leq n_{\text{jet}} \leq 3, n_b = 0$ analysis category.

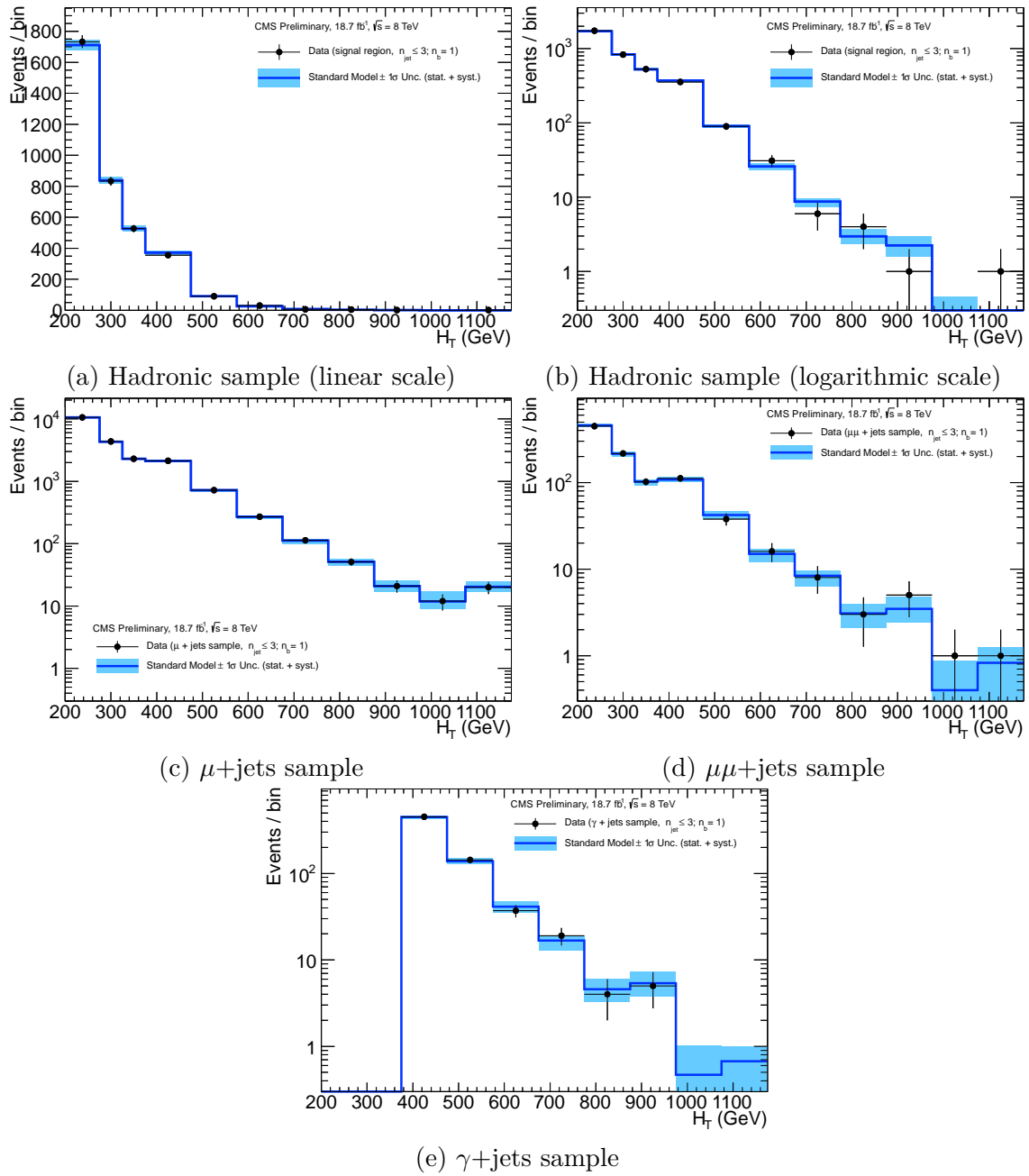


Fig. 8.11 Observations in data for the various signal and control regions in the analysis, compared to the result of the full likelihood model simultaneous fit. The plots are for the $2 \leq n_{jet} \leq 3, n_b = 1$ analysis category.

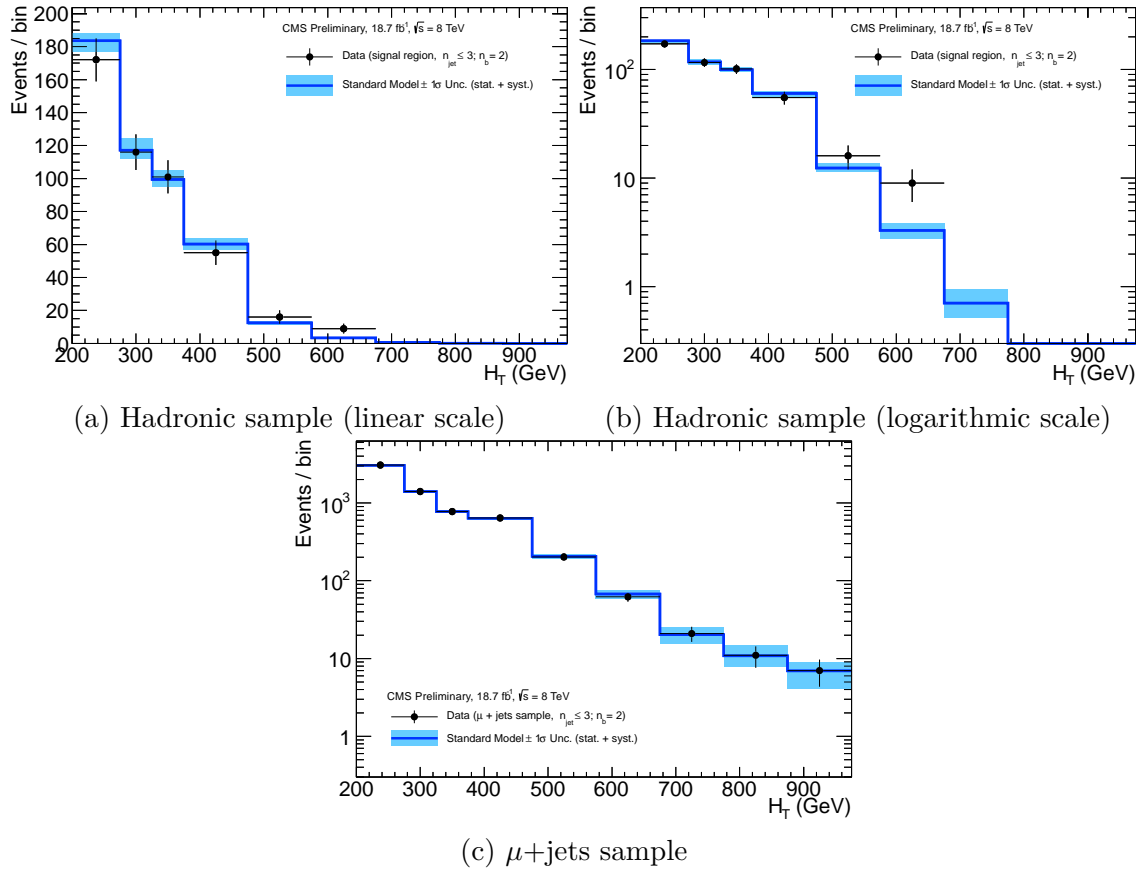


Fig. 8.12 Observations in data for the various signal and control regions in the analysis, compared to the result of the full likelihood model simultaneous fit. The plots are for the $2 \leq n_{\text{jet}} \leq 3$, $n_b = 2$ analysis category.

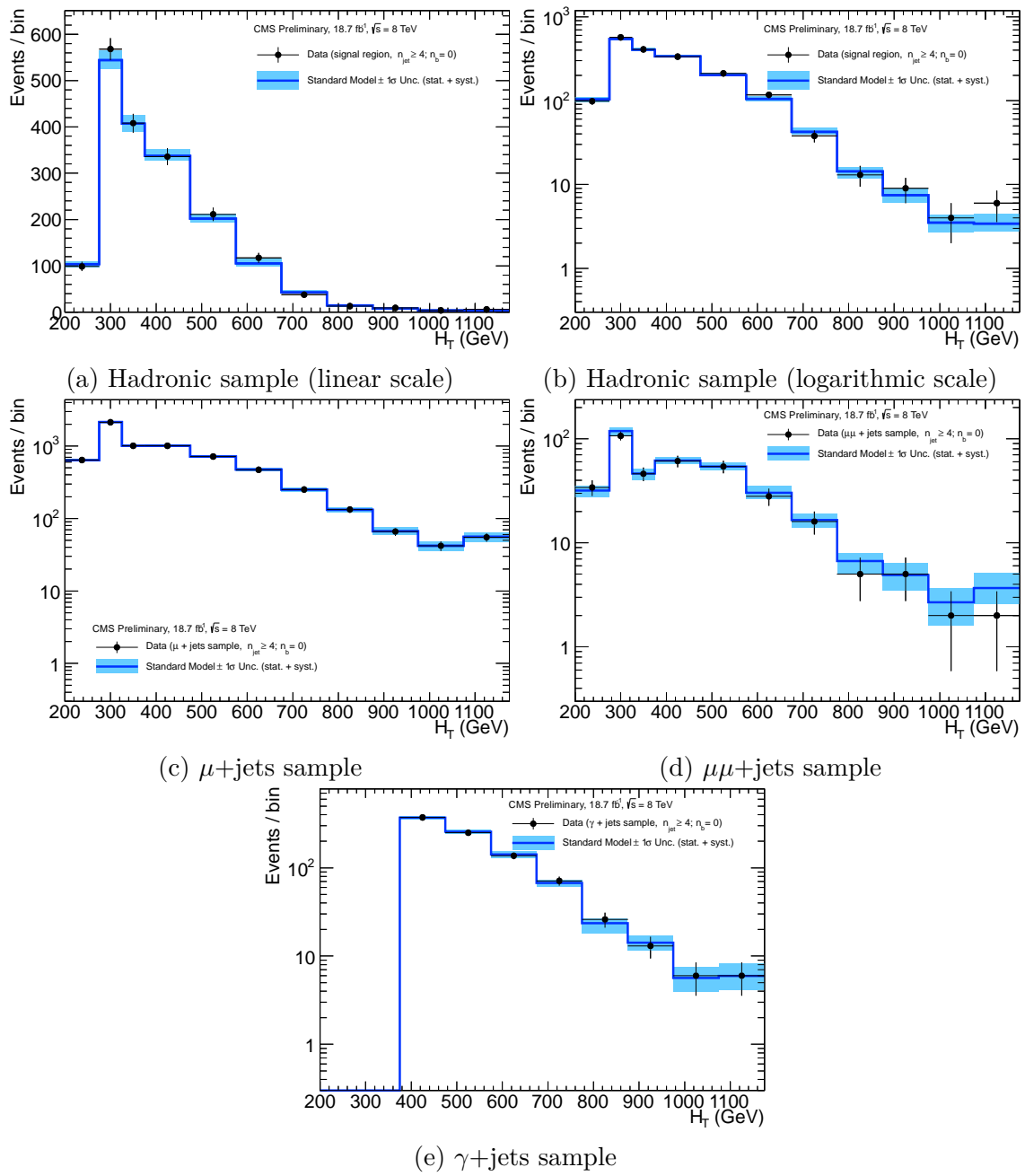


Fig. 8.13 Observations in data for the various signal and control regions in the analysis, compared to the result of the full likelihood model simultaneous fit. The plots are for the $n_{\text{jet}} \geq 4, n_b = 0$ analysis category.

8.2 Fit Results

113

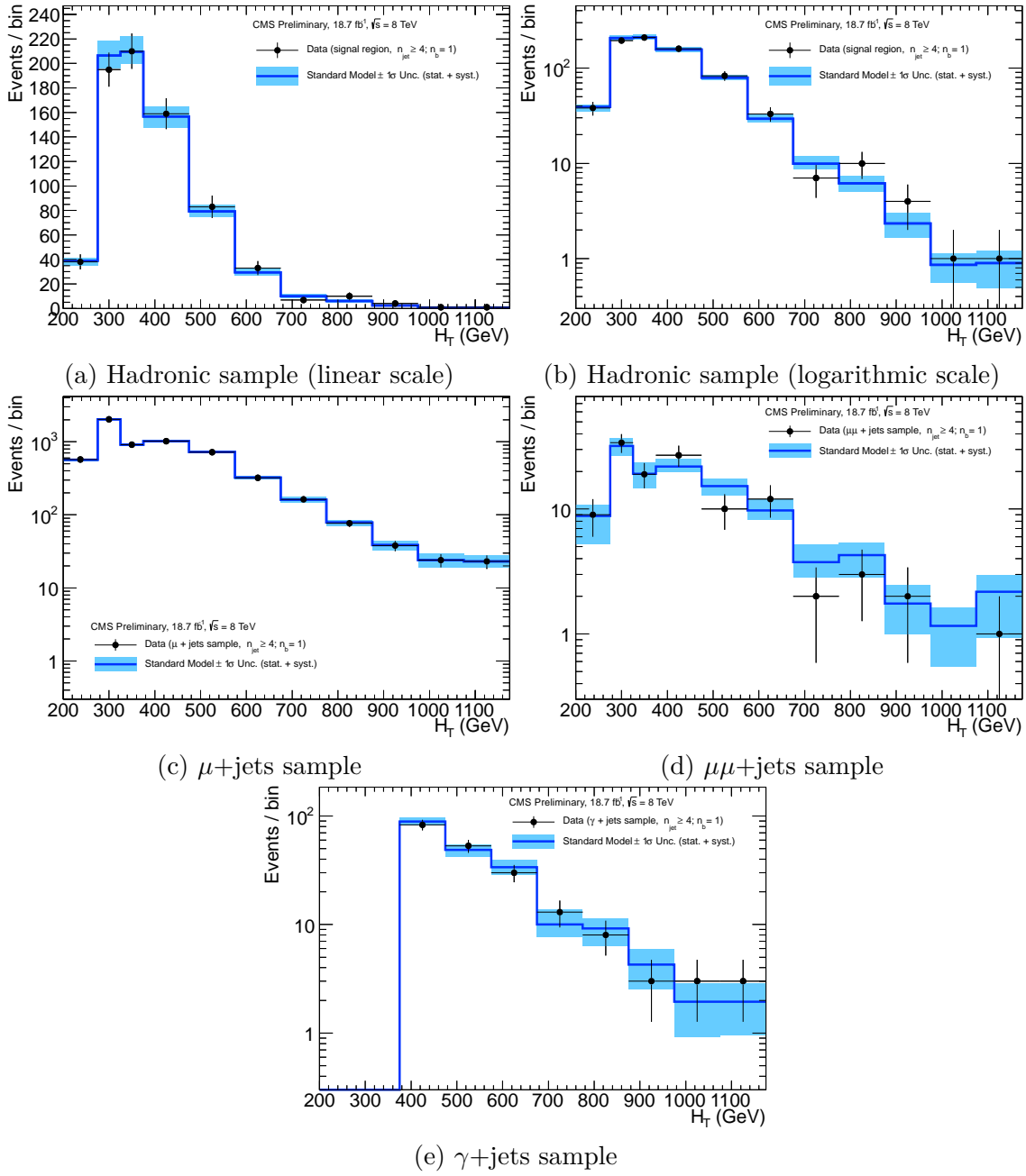


Fig. 8.14 Observations in data for the various signal and control regions in the analysis, compared to the result of the full likelihood model simultaneous fit. The plots are for the $n_{\text{jet}} \geq 4$, $n_b = 1$ analysis category.

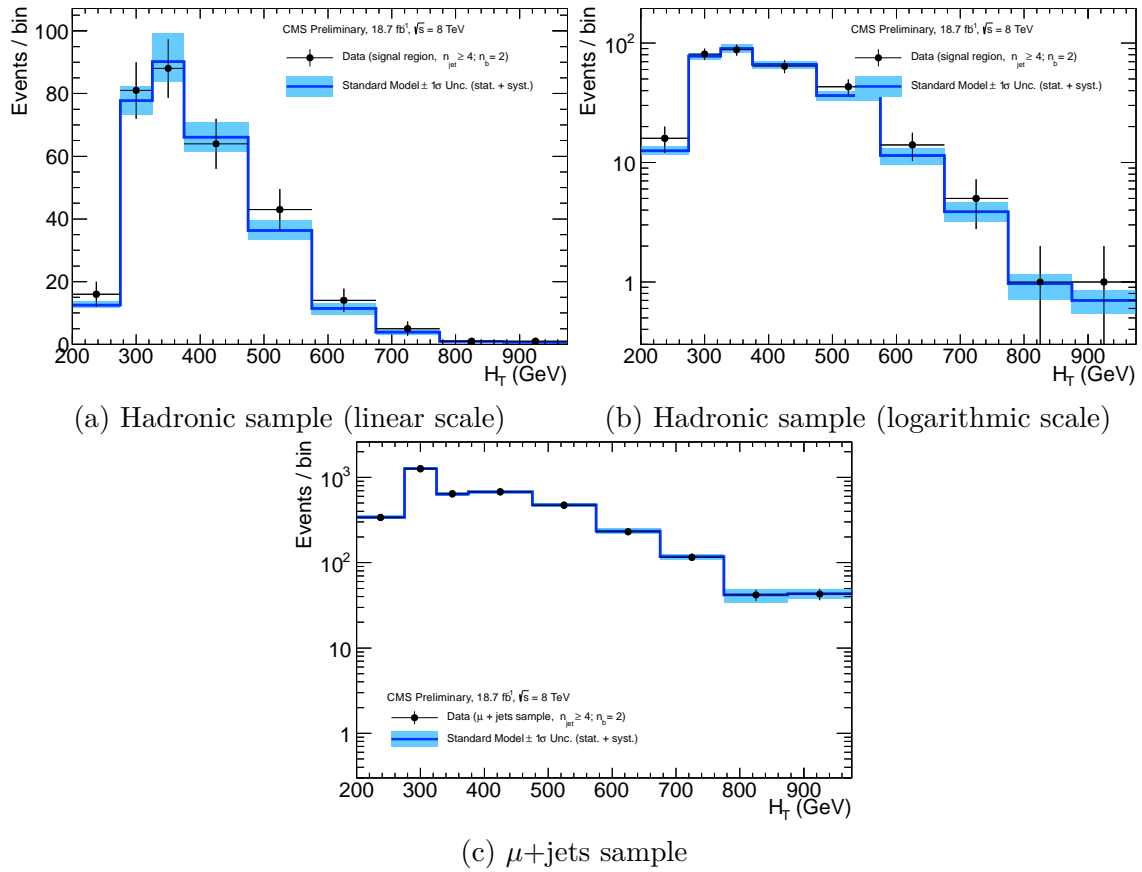


Fig. 8.15 Observations in data for the various signal and control regions in the analysis, compared to the result of the full likelihood model simultaneous fit. The plots are for the $n_{\text{jet}} \geq 4, n_b = 2$ analysis category.

8.2 Fit Results

115

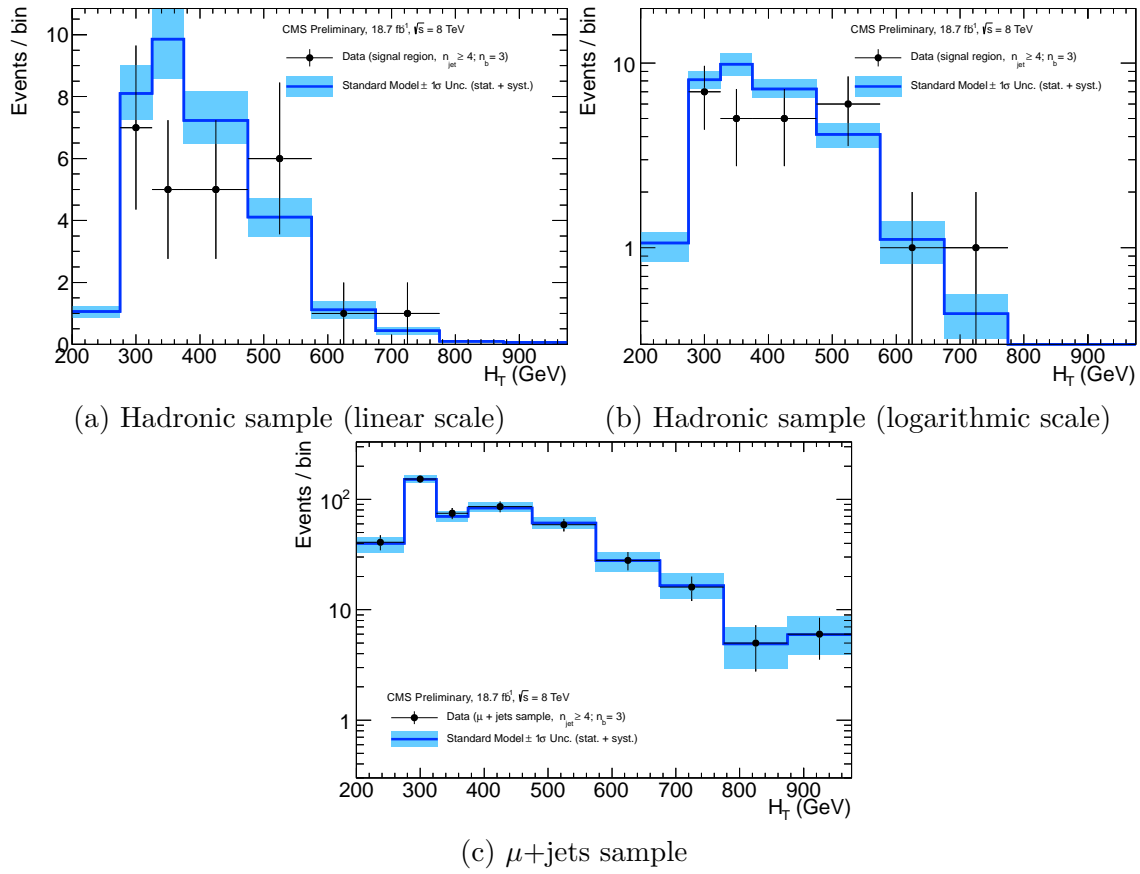


Fig. 8.16 Observations in data for the various signal and control regions in the analysis, compared to the result of the full likelihood model simultaneous fit. The plots are for the $n_{jet} \geq 4, n_b = 3$ analysis category.

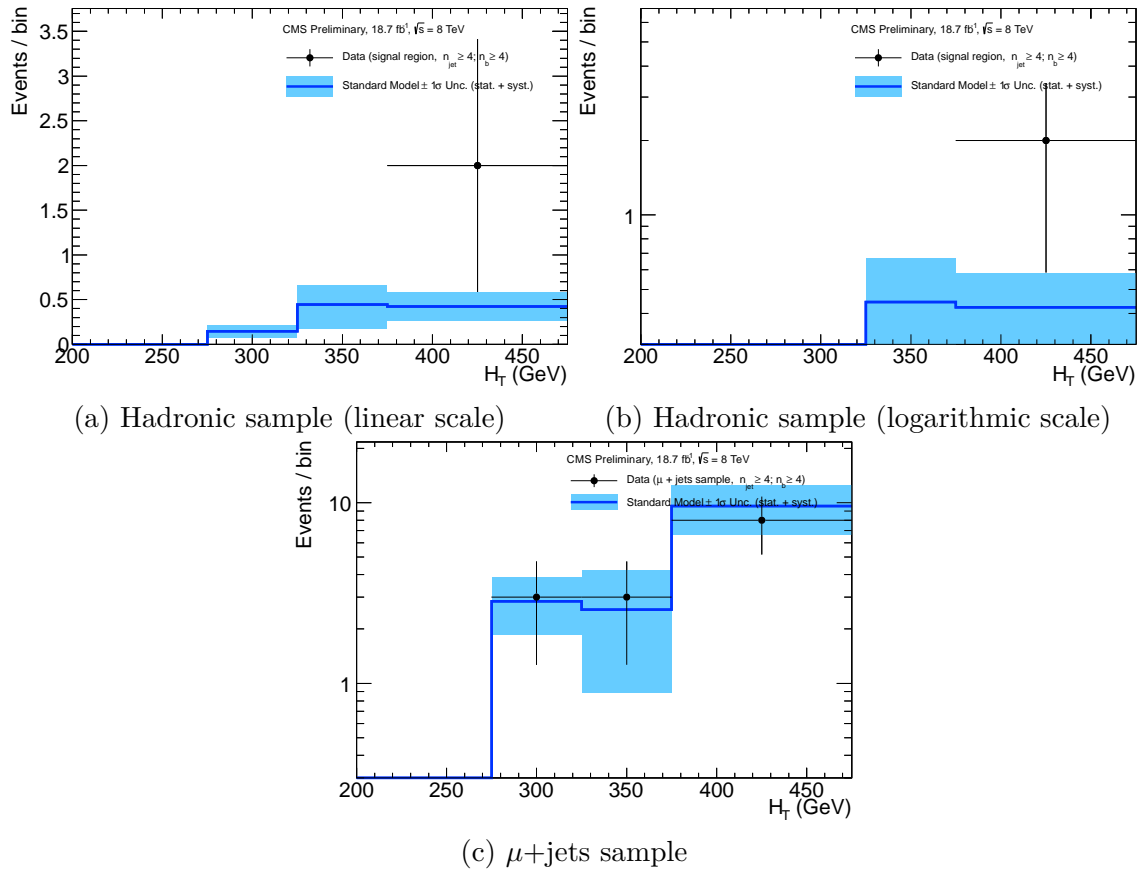


Fig. 8.17 Observations in data for the various signal and control regions in the analysis, compared to the result of the full likelihood model simultaneous fit. The plots are for the $n_{\text{jet}} \geq 4$, $n_b \geq 4$ analysis category.

¹ Chapter 9

Interpretation ¹

9.1 Signal Acceptance ²

Model acceptance is determined as a function of analysis category (n_b , n_{jet}) and H_T bin. This calculation is performed individually for each mass point in the scan plane for both the hadronic and muon selections (to determine signal contamination in the control region). Interpretations are made using a selected subset of the most sensitive analysis categories, but an inclusive H_T selection. The analysis categories used are selected after an inspection of each for their significance given signal injection from specific mass points. ³ ⁴ ⁵ ⁶ ⁷ ⁸ ⁹

9.1.1 T2cc ¹⁰

Signal efficiency times acceptance for the T2cc model, $pp \rightarrow \tilde{t}\tilde{t}^* \rightarrow c\tilde{\chi}^0 \bar{c}\tilde{\chi}^0$, is shown in figure 9.1 for the four categories with the greatest sensitivity. The largest acceptance is seen in the $2 \leq n_{jet} \leq 3$, $n_b = 0$ analysis category (figure 9.1a), where efficiencies are around the percent level. At small mass splittings, nearest the kinematically inaccessible diagonal region, acceptance is due to hard initial state radiation (ISR) jets balancing a soft SUSY decay system. Small mass splittings imply little energy is available for decay products to gain sufficient momentum to be within acceptance, and therefore become invisible to the analysis. In order for such an event to pass the selection criteria of the signal sample, hard ISR jets are required to be within kinematic acceptance and boosting this decay system. ¹¹ ¹² ¹³ ¹⁴ ¹⁵ ¹⁶ ¹⁷ ¹⁸ ¹⁹ ²⁰

Moving away from the diagonal to increasing values of Δm indicates a drop in acceptance, eventually leading to an increase due to a competing effect from the increase ²¹ ²²

in available kinematic phase space. Far from the diagonal, decay products are able to gain sufficient momentum to enter acceptance, becoming visible. There is still a dependence on ISR jets boosting this system, however crucially jets originating from charm quarks can now be observed. Contributions to acceptance therefore increase not only for this $n_b = 0$ category, but similarly for $n_b = 1$ categories, due to mistagging of the visible charm jets, where lower acceptance is observed at small Δm .

Finally, increased acceptance is observed in the $n_{\text{jet}} \geq 4$ categories, predominantly away from the diagonal. Again, given the increased kinematic phase space of the larger mass splitting scenarios, more jets can be in acceptance.

Signal contamination in the $\mu + \text{jets}$ selection is shown to be negligible, given the lack of leptons in the final state.

Example cutflows are shown in table 9.1 for mass points with the two extremal Δm values of the scan, both at values of $m_{\tilde{t}}$ near the limits of sensitivity.

Table 9.1 Cutflow table for two mass points ($m_{\tilde{t}} = 250$ GeV, $m_{\tilde{\chi}^0} = 240$ GeV and $m_{\tilde{t}} = 250$ GeV, $m_{\tilde{\chi}^0} = 170$ GeV) of the T2cc signal model. The selection represents the hadronic signal region for the $H_T > 375$ GeV region.

Cut Name ($m_{\tilde{t}}, m_{\tilde{\chi}^0}$)	Cumulative Eff. (%)	
	(250, 240)	(250, 170)
Event Counter	100.00	100.00
$n_{\text{jet}} \geq 2$	12.99	59.52
MET Filters	12.99	59.52
Vertex Noise Filter	12.99	59.52
HBHE Noise Filter	12.99	59.52
DeadECAL Filter	10.77	43.88
$n_e = 0$	10.77	43.88
$n_\gamma = 0$	10.77	43.7
$n_\mu = 0$	10.77	43.7
EMF_{\max} for all jets > 0.1	10.77	43.7
Leading jet $p_T > 100$ GeV	7.37	24.79
Leading jet $\eta < 2.5$	7.04	24.21
Sub-Leading jet $p_T > 100$ GeV	2.31	8.92
$n_{j,\text{fail}} = 0$	2.26	8.66
$\Delta R(\mu_{\text{fail}}^i, \text{jet}^j) < 0.5$	2.26	8.65
$(\sum n_{\text{vertices}} p_T) / H_T$	2.26	8.65
recHitCut	2.26	8.65
$n_{SIT} = 0$	2.09	8.03
$\Delta\phi_{\min}^* > 0.3$	1.84	5.42
$H_T/\mathbb{E}_T < 1.25$	1.68	4.46
$H_T > 375$ GeV	0.90	2.05
$\alpha_T > 0.55$	0.45	0.40
$H_T/\mathbb{E}_T < 1.25$	0.45	0.40

9.1 Signal Acceptance

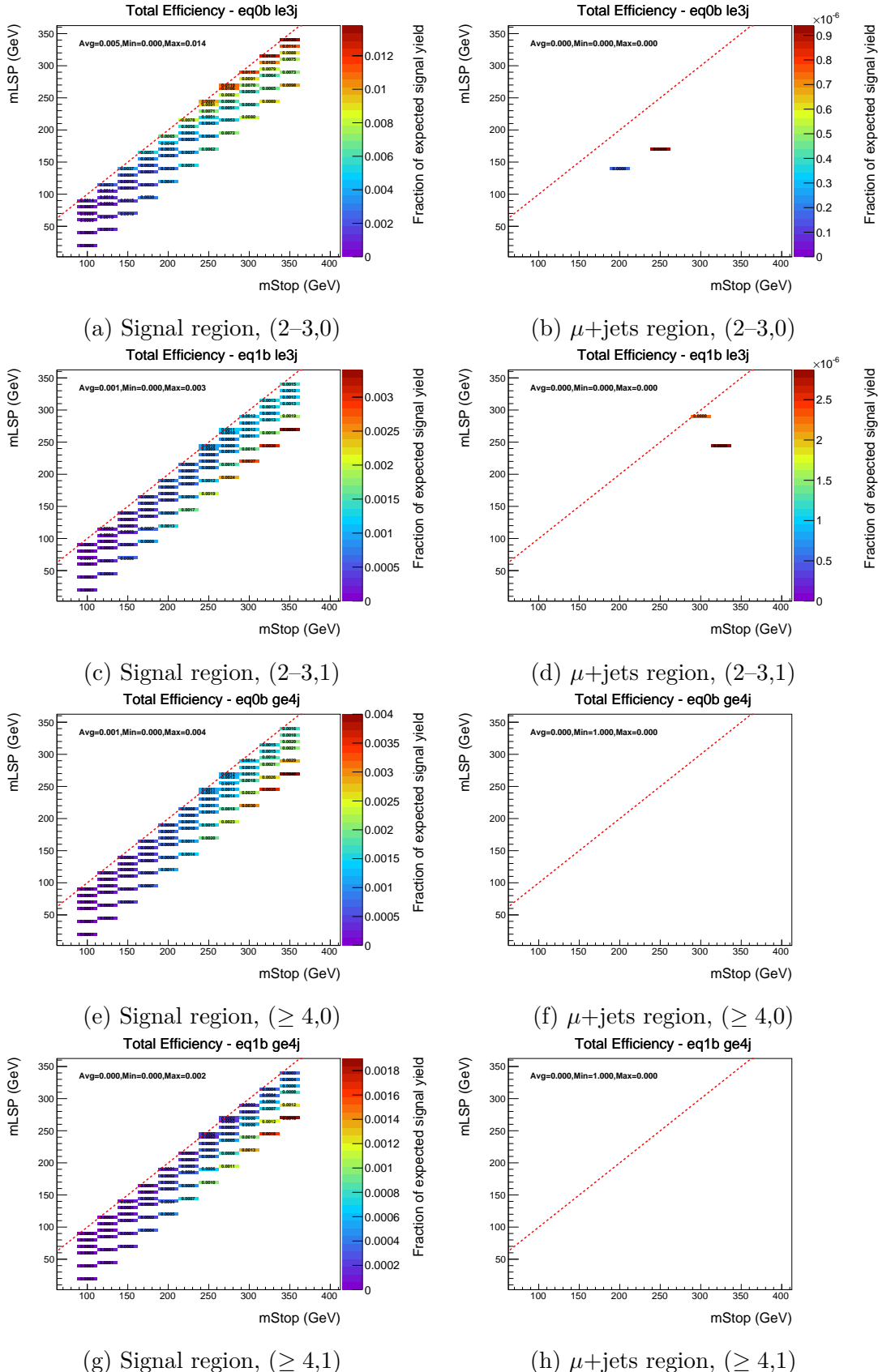


Fig. 9.1 Signal efficiency times acceptance of the $pp \rightarrow \tilde{t}\tilde{t}^* \rightarrow c\tilde{\chi}^0 \bar{c}\tilde{\chi}^0$ simplified model, for the hadronic selection (left) and the μ +jets selection (right), shown for the four most sensitive analysis categories with an inclusive selection on H_T .

¹³ 9.1.2 T2_4body

¹ The signal efficiency times acceptance distributions for the **T2degen** model, $\text{pp} \rightarrow$
² $\tilde{t}\tilde{t}^* \rightarrow bff'\tilde{\chi}^0 bff'\tilde{\chi}^0$, are shown in figure 9.3 in the four most sensitive analysis
³ categories, with an inclusive H_T selection, both for the hadronic and $\mu+\text{jets}$ selections.
⁴ There are strong similarities with those shown earlier for the **T2cc** model, both in
⁵ magnitude and distribution about the plane. At small values of Δm , given that
⁶ the entire SUSY decay system becomes invisible due to a lack of kinematic phase
⁷ space, both models show very similar efficiencies, where acceptance is almost entirely
⁸ due to hard ISR jets within acceptance. There is a significant difference however,
⁹ when a b-tagged jet is required, for example in the $2 \leq n_{\text{jet}} \leq 3$, $n_b = 1$ category
¹⁰ (figure 9.3c), where the presence of a jet originating from a real b quark improves
¹¹ acceptance, particularly away from the diagonal where this jet would be more likely
¹² to pass analysis thresholds. Less significant are the efficiencies seen in the $n_{\text{jet}} \geq 4$
¹³ categories, given the larger number of final state objects, each requiring a share of the
¹⁴ energy originating from the mass splitting of the mother and daughter sparticles.

¹⁵ Also of note is the increase in signal contamination observed in the $\mu+\text{jets}$ selection,
¹⁶ due to the presence of $f\bar{f}$ in the decay chain, potentially providing leptons in the final
¹⁷ state.

¹⁸ Example cutflows are shown in table 9.2 for a mass point with the smallest mass
¹⁹ splitting, at an $m_{\tilde{t}}$ value near the limit of sensitivity.

²⁰ 9.1.3 ISR Corrections to compressed spectra MC signal samples

²² Given the reliance of such compressed spectra models on ISR jets for acceptance, a
²³ dedicated study was performed within the SUSY Physics Analysis Group (*PAG*) into
²⁴ the accuracy of it's modelling and relevant systematic uncertainties [5].

²⁵ A comparison of data to MC was performed for a pure, high-statistics selection of Z
²⁶ boson production with associated jets, where the Z decays to an opposite-sign, same-
²⁷ flavour (OSSF) lepton pair, $Z \rightarrow l\bar{l}$. By tagging the leptons in the event, remaining
²⁸ jets can be considered as an ISR jet based “recoil system” against that of the Z boson
²⁹ decay. Comparisons of data to MC for both the vectorial sum of the lepton \vec{p}_T 's
³⁰ and the recoil jet system's \vec{p}_T indicate an over-prediction in MC as a function of the
³¹ system's p_T , of up to 20% in high p_T scenarios, shown in figure 9.2.

³² Correction factors for MADGRAPH based samples, dependent on the p_T of the jet

9.1 Signal Acceptance

121

Table 9.2 Cutflow table for two mass points ($m_{\tilde{t}} = 250$ GeV, $m_{\tilde{\chi}^0} = 240$ GeV and $m_{\tilde{t}} = 250$ GeV, $m_{\tilde{\chi}^0} = 170$ GeV) of the T2Degen signal model. The selection represents the hadronic signal region for the $H_T > 375$ GeV region.

Cut Name	Cumulative Eff. (%)	
$(m_{\tilde{t}}, m_{\tilde{\chi}^0})$	(250, 240)	(250, 170)
Event Counter	100.00	100.00
$n_{\text{jet}} \geq 2$	10.80	32.33
MET Filters	10.80	32.33
Vertex Noise Filter	10.80	32.33
HBHE Noise Filter	10.80	32.33
DeadECAL Filter	9.13	21.30
$n_e = 0$	9.13	19.70
$n_\gamma = 0$	9.13	19.55
$n_\mu = 0$	9.13	17.41
EMF_{\max} for all jets > 0.1	9.13	17.41
Leading jet $p_T > 100$ GeV	6.01	8.70
Leading jet $\eta < 2.5$	5.70	8.37
Sub-Leading jet $p_T > 100$ GeV	1.64	2.23
$n_{j,\text{fail}} = 0$	1.61	2.17
$\Delta R(\mu_{\text{fail}}^i, \text{jet}^j) < 0.5$	1.61	2.11
$(\sum n_{\text{vertices}} p_T) / H_T$	1.61	2.11
recHitCut	1.61	2.11
$n_{SIT} = 0$	1.50	1.67
$\Delta\phi_{\min}^* > 0.3$	1.35	0.93
$H_T/\cancel{E}_T < 1.25$	1.24	0.68
$H_T > 375$ GeV	0.55	0.37
$\alpha_T > 0.55$	0.26	0.08
$H_T/\cancel{E}_T < 1.25$	0.26	0.08

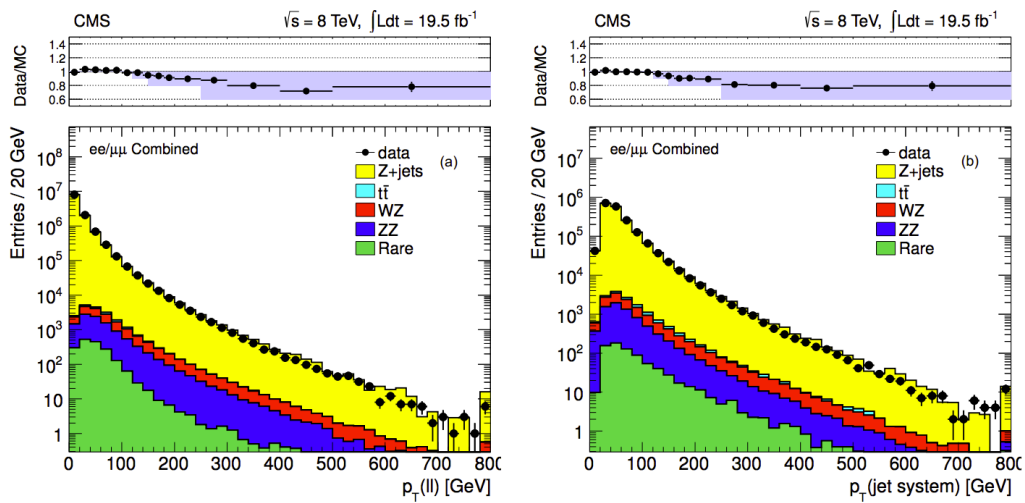


Fig. 9.2 Data to MC comparisons for an enriched $Z \rightarrow l\bar{l}$ selection, with the vectorial sum of lepton p_T 's (left) and of the recoil jets (right) [5].

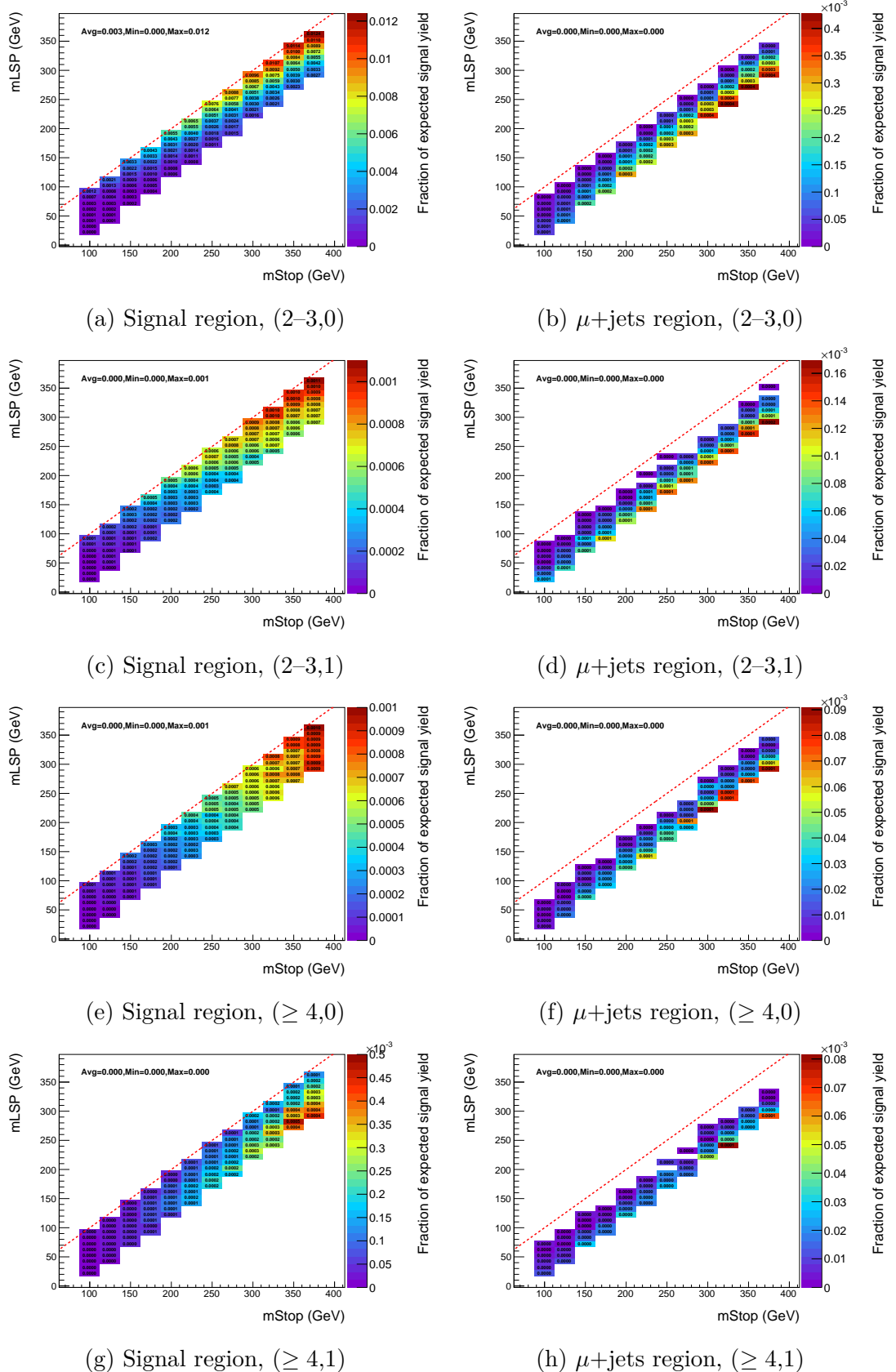


Fig. 9.3 Signal efficiency times acceptance of the $\text{pp} \rightarrow \tilde{t}\tilde{t}^* \rightarrow bff'\tilde{\chi}^0 bff'\tilde{\chi}^0$ simplified model, for the hadronic selection (left) and the $\mu + \text{jets}$ selection (right), shown for the four most sensitive analysis categories with an inclusive selection on H_T .

 9.2 Systematic Uncertainties on Signal Acceptance
 123

³³ system, can therefore be derived by extracting the ratio of data to MC. These values are summarised in table 9.3. Weights are applied to both T2cc and T2degen samples at the event level, where the event’s boost p_T is determined by calculating the vectorial sum of the two, pair-produced generator level \tilde{t} particles.

Table 9.3 Correction factors for MADGRAPH based signal samples to account for MC over-prediction of ISR.

$p_{T\text{boost}}$ (GeV)	Correction Factor
$0 < p_T \leq 120$	1.00
$120 < p_T \leq 150$	0.95
$150 < p_T \leq 250$	0.90
$250 < p_T$	0.80

9.2 Systematic Uncertainties on Signal Acceptance

4

A range of sources of systematic uncertainty on the acceptance times signal efficiency are considered for each signal model. The main sources, namely jet energy scale (JES), initial state radiation (ISR), b-tag scale factors, parton distribution function (PDF), the H_T/\mathbb{E}_T cut and the dead ECAL filter, have systematic values determined per point in the scan plane, as a function of H_T , n_b and n_{jet} . The remaining systematics are applied as a flat contribution across the entire plane, considered as a conservative approach.

Although systematics are considered as a function of the H_T dimension of the analysis, all plots shown represent an inclusive selection of $H_T > 200$ GeV.

9.2.1 Jet energy scale

14

The acceptance times signal efficiency is tested for sensitivity to jet energies by measuring it’s change to upwards and downwards variations of all jet energies by the p_T and η -dependent jet energy scale (JES) uncertainty, as prescribed by the JetMET POG.

Distributions showing the acceptance changes due to the variations in JES are shown in Appendices A for the T2cc model and A for the T2Degen model.

In both models, the effects of applying JES variations are stronger in the $n_{\text{jet}} \geq 4$ category. An increased number of jets sharing the small kinematic phase space of

the compressed region implies softer jets. Therefore applying variations on the jet energies increases the probability to move jets in and out of acceptance. This effect is also noticeable in the $2 \leq n_{\text{jet}} \leq 3$, $n_b = 1$ category for T2cc (figure A.1f), where changes in efficiencies are larger away from the diagonal, where acceptance gradually increases dependence on jets originating from the soft SUSY decay.²³

The T2Degen model decay contains a real b-quark, and consequently JES uncertainties have a dependence on n_b , as higher variations are observed in the $n_b = 1$ category (figure A.8f).

9.2.2 Initial State Radiation

As described in section 9.1.3, boost p_T dependent event weights are taken from the data to MC comparison study performed within the SUSY PAG. A procedure is also defined to determine related systematics, by applying upwards and downwards variations of weights corresponding to the magnitude of the corrections themselves, and studying the effect on signal efficiency times acceptance. These weights are summarised in table 9.4.

Table 9.4 Systematic factors for MADGRAPH based signal samples to determine ISR modelling related systematics.

$p_{T,\text{boost}}$ (GeV)	Systematic Variation
$0 < p_T \leq 120$	± 0.0
$120 < p_T \leq 150$	± 0.05
$150 < p_T \leq 250$	± 0.10
$250 < p_T$	± 0.20

As discussed previously in sections 9.1.1 and 9.1.2, acceptance for compressed spectra models at the smallest Δm (i.e. nearest the diagonal) is predominantly due to presence of hard ISR jets. Away from the diagonal, ISR jets are still important, instead to boost the soft SUSY decay system. Subsequently, systematics due to ISR variations are observed to be largest nearest the diagonal for all analysis categories, as shown in figure A.3 and A.9 for T2cc and T2Degen respectively. Due to the overall dependence on ISR, the related systematics are the largest contribution to the total systematic value.

²³ **9.2.3 Btag scale factors**

Specifically for FASTSIM signal samples, events are not weighted using the b-tag formula method described in section 6.6, but instead using the recommended method for FULLSIM samples with an additional FULLSIM to FASTSIM correction factor applied. The original correction is dependent on the generator level content of an event, and is defined as:

$$w = \frac{SF_b\epsilon \times (1 - SF_b\epsilon) \times SF_{c,light}m \times (1 - SF_{c,light}m)}{\epsilon \times (1 - \epsilon) \times m \times (1 - m)} \quad (9.1)$$

where $\epsilon(p_T, \eta)$ and $m(p_T, \eta)$ are the b-tagging efficiency and mistagging rate, respectively. These factors are functions of p_T and η , and are measured in SM MC for both the hadronic and μ +jets samples, in each H_T bin.

Applying this event weight provides ‘corrected’ MC yields, which then have further FASTSIM to FULLSIM correction factors applied, as recommended by [67].

Systematic variations equal to the errors of these corrections are applied as upwards and downwards variations, and any effects on signal efficiency times acceptance are studied.

As expected, only small changes in acceptance are found in the T2cc model when b-tag scale factor variations are applied, as shown in figure A.4. While not entirely negligible, it is worth noting that systematics are slightly larger for the $n_b = 1$ category (figure A.4f), however still at a low level with respect to other systematic sources.

The T2Degen model exhibits a similar dependence on the b-tag scale factor variations, indicating large changes in efficiency nearer the diagonal in $n_b = 1$ categories. This increase is visible in figure A.10f at smaller values of Δm , where the final state b-quark is likely out of acceptance, and therefore tags originate from mis-tagged lighter quarks or gluons.

9.2.4 PDF

Montecarlo generation includes a simulation of the Parton Density Function (PDF) of the incoming partons, described by a ‘PDF set’. Signal samples are produced using the CTEQ6L1 PDF set. The acceptance sensitivity to the PDF set is investigated by comparing results using three other commonly used PDF sets, namely CT10, NNPDF2.1 and MSTW2008. Following PDF4LHC recommendations, the output is combined to determine an ‘envelope’ value combining the three alternative PDF

sets, and a related systematic uncertainty [68].

31

1 The effect on selection efficiency was studied for T2cc with the central value and
 2 upwards and downwards fluctuation plots summarised in figure A.2. The largest vari-
 3 ations are taken as the systematic uncertainty for both the T2cc and T2Degen models,
 4 given their identical initial states.

5 9.2.5 $\mathcal{H}_T/\mathcal{E}_T$ cleaning cut

6 The efficiency of the $\mathcal{H}_T/\mathcal{E}_T$ cleaning cut is compared between data and MC with
 7 the aim of revealing any potential issues due to MC mis-modelling of the variable.
 8 Efficiencies are compared in the $\mu+$ jets control sample, using H_T bins ranging from
 9 $200 < H_T < 375$ GeV, in both n_{jet} categories, with no requirement on n_b . Efficiencies
 10 are summarised in table 9.5, where efficiency comparisons between data and MC are
 11 shown to statistically agree with unity.

Table 9.5 Efficiencies of the $\mathcal{H}_T/\mathcal{E}_T$ requirement cut for the $\mu+$ jets selection in data ϵ_{data} and MC ϵ_{MC} , as well as the ratio of both. Efficiencies are shown for the two n_{jet} categories and the four lowest H_T bins, with an inclusive requirements are made of n_b .

n_{jet}	H_T (GeV)	ϵ_{MC}	ϵ_{data}	$\epsilon_{\text{MC}}/\epsilon_{\text{data}}$
2–3	200–275	0.95 ± 0.00	0.95 ± 0.01	1.00 ± 0.01
2–3	275–325	0.97 ± 0.01	0.97 ± 0.02	1.00 ± 0.02
2–3	325–375	0.97 ± 0.01	0.97 ± 0.02	1.00 ± 0.02
2–3	375–475	0.98 ± 0.01	0.98 ± 0.03	1.00 ± 0.03
≥ 4	200–275	0.90 ± 0.02	0.92 ± 0.04	0.98 ± 0.04
≥ 4	275–325	0.92 ± 0.01	0.93 ± 0.02	0.99 ± 0.02
≥ 4	325–375	0.92 ± 0.01	0.93 ± 0.04	0.99 ± 0.04
≥ 4	375–475	0.95 ± 0.02	0.95 ± 0.04	1.00 ± 0.04

12 While the relevant systematic for the $\mathcal{H}_T/\mathcal{E}_T$ requirement is taken from the above
 13 method, it is also interesting to study the acceptance of this cut as a function of the
 14 mass plane for each decay. Model acceptance to the $\mathcal{H}_T/\mathcal{E}_T$ cut is typically lower in
 15 the 4-body decay. This is attributed to the softer jet spectrum produced due to the
 16 increased number of final state particles sharing the finite energy of the decay system.

17 9.2.6 Dead ECAL Filter

18 To assess any potential MC mis-modelling issues with the dead ECAL filter, a similar
 19 analysis is made as described for the $\mathcal{H}_T/\mathcal{E}_T$ cut in section 9.2.5. Efficiencies between

9.2 Systematic Uncertainties on Signal Acceptance

127

²⁰ data and MC are compared for the μ +jets selection, with an inclusive requirement on both n_b and H_T . As shown in table 9.6, the ratio of efficiencies between data and MC for each n_{jet} category agree within statistical errors.

Table 9.6 Efficiencies of the dead ECAL cut for the μ +jets selection in data ϵ_{data} and MC ϵ_{MC} , as well as the ratio of both. Efficiencies are shown for the two n_{jet} categories and the four lowest H_T bins, with an inclusive requirements are made of n_b .

n_{jet}	H_T (GeV)	ϵ_{MC}	ϵ_{data}	$\epsilon_{MC}/\epsilon_{data}$
2–3	> 200	0.64 ± 0.01	0.64 ± 0.01	1.00 ± 0.01
≥ 4	> 200	0.58 ± 0.01	0.59 ± 0.01	0.98 ± 0.01

Similarly to the study of the $\cancel{H}_T/\cancel{E}_T$ requirement, an inspection of the acceptance of the dead ECAL filter in each scan plane indicates a greater reduction in acceptance for the 4-body decay with respect to the charm decay. The larger number of particles in the final state of the 4-body decay increases the probability for an energy deposit to be made near a flagged region of the calorimeter system, thereby rejecting more events. Rejection increases away from the diagonal, as more objects move into acceptance.

but the n_{jet} requirements are the same between samples...perhaps the fraction of 3jet/2jet within the le3j category, is greater for 4body?

9.2.7 Generator Level Partons

At the MADGRAPH matrix element stage of the MC simulation production, a number of additional feynman diagrams are simulated to account for associated parton interactions, such as Initial State Radiation (ISR) and Final State Radiation (FSR). Given the dependence on such processes in the compressed spectra regime, an additional sub-sample of the T2cc scan has been produced with up to 3 additional partons, to compare against the up to 2 additional partons of the complete scan. This sample contains two mass points at a stop mass near the region of maximum sensitivity, with mass splittings covering both extremeties of the scan ($\Delta m = 10$ GeV, 80 GeV). The relative change in efficiency times acceptance between the two scans is shown in table 9.7. These values are interpreted as systematic uncertainties on the number of associated partons modelled for such compressed spectra models, and are applied as flat contributions across the scan plan for all models.

Table 9.7 Relative change in efficiency times acceptance for the 2-parton and 3-parton scans in the signal region, with an inclusive selection on n_b and $H_T > 200$ GeV. The scan points are $m_{\tilde{t}} = 200$ GeV and $m_{\tilde{\chi}^0} = (120, 190)$ GeV.

Category	Δm (GeV)	
	10	80
(2–3,0)	0.00	0.04
(2–3,1)	0.02	0.04
($\geq 4,0$)	0.04	0.04
($\geq 4,1$)	0.00	0.00

9.2.8 Luminosity Measurement

24

- ¹ Flat corrections across the scan plane are made to account for the uncertainty of the
² luminosity measurement, as quoted by Lumi *POG* at 2.5% [69].

9.2.9 Summary

- ⁴ For each mass point in the scan plane, the total systematic is the sum in quadrature of
⁵ all individual contributions. Representative values are summarised in tables 9.8 and
⁶ 9.9, with full results shown in figures A.7 and A.13 in the mass plane of T2cc and
⁷ T2Degen respectively. The distribution of total systematic values seen in these plots
⁸ has been corrected to account for statistical fluctuations through the use of an iterative
⁹ smoothing procedure that considers a weighted average of each mass point value of
¹⁰ the surrounding points. This procedure is carefully checked to ensure no loss of total
¹¹ systematic trends in either $m_{\tilde{t}}$ or Δm .

Table 9.8 Representative ranges for each contribution to the total systematic uncertainty on the signal efficiency times acceptance for each relevant event category for the T2cc interpretation.

Category	(2–3,0)		(2–3,1)		($\geq 4,0$)		($\geq 4,1$)		($\geq 2, \geq 0$)	
Range	Min.	Max.	Min.	Max.	Min.	Max.	Min.	Max.	Min.	Max.
PDF									0.04	0.14
JES	0.01	0.12	0.01	0.18	0.10	0.23	0.07	0.23		
ISR	0.09	0.21	0.08	0.21	0.13	0.22	0.13	0.23		
b-tag SF	0.01	0.02	0.03	0.07	0.01	0.02	0.02	0.07		
H_T/\cancel{E}_T	0.02	0.02	0.02	0.02	0.02	0.02	0.02	0.02		
Dead ECAL	0.02	0.02	0.02	0.02	0.02	0.02	0.02	0.02		
Total syst	0.14	0.21	0.16	0.22	0.22	0.26	0.23	0.30		

Table 9.9 Representative ranges for each contribution to the total systematic uncertainty on the signal efficiency times acceptance for each relevant event category for the T2Degen interpretation.

Category	(2–3,0)		(2–3,1)		($\geq 4,0$)		($\geq 4,1$)		($\geq 2,\geq 0$)	
Range	Min.	Max.	Min.	Max.	Min.	Max.	Min.	Max.	Min.	Max.
PDF									0.04	0.14
JES	0.00	0.12	0.00	0.19	0.01	0.32	0.02	0.40		
ISR	0.07	0.20	0.05	0.21	0.10	0.22	0.06	0.22		
b-tag SF	0.01	0.02	0.01	0.07	0.01	0.04	0.00	0.07		
$\cancel{H}_T/\cancel{E}_T$	0.02	0.02	0.02	0.02	0.02	0.02	0.02	0.02		
Dead ECAL	0.02	0.02	0.02	0.02	0.02	0.02	0.02	0.02		
Total syst	0.18	0.21	0.21	0.23	0.25	0.31	0.27	0.45		

¹² 9.3 Limits on models of Supersymmetry

9.3.1 Overview of limit setting procedure

Signal models are tested for compatibility with observations using a modified frequentist method, namely ‘CLs’ [70]. A test statistic, used to rank experiments from least to most signal-like, is defined as:

$$q_\mu = \begin{cases} -2\log\lambda(\mu), & \text{if } \mu \geq \hat{\mu} \\ 0., & \text{otherwise} \end{cases}, \quad (9.2) \quad 5$$

where:

$$\lambda(\mu) = \frac{L(\mu, \theta_\mu)}{L(\hat{\mu}, \hat{\theta}_\mu)}, \quad (9.3) \quad 6$$

μ is the signal strength parameter (equivalent to the variable f defined in section 8.1, where $\mu = 1$ represents a given signal at its nominal cross-section), θ_μ is a set of nuisance parameters for a given μ , $\hat{\mu}$ is the Maximum Likelihood (ML) value of μ , and $\hat{\theta}$ is the corresponding ML set of nuisance parameters.

Distributions of q_μ are populated from pseudo-experiments under signal + background and background only hypotheses. For a given observation, 1 minus the quantiles of each distribution are used to determine CL_{s+b} and CL_b , which are used to define:

$$CL_s = \frac{CL_{s+b}}{CL_b}. \quad (9.4) \quad 15$$

A model is considered to be excluded at 95% confidence level if $CL_s \leq 0.05$.

maybe include razor example distribution from SUS12005

18

¹ 9.3.2 Limits

² Limits are calculated using 1000 pseudo-experiments per model mass point. Expected
³ limits are determined by considering a scenario where data observations are assumed
⁴ to be equal to the result of the green-band fits (section 8.2.1), and observed limits
⁵ by considering that actual data observations. A point is considered excluded if the
⁶ calculated upper limit cross section is less than the nominal cross-section (NLO+NLL).

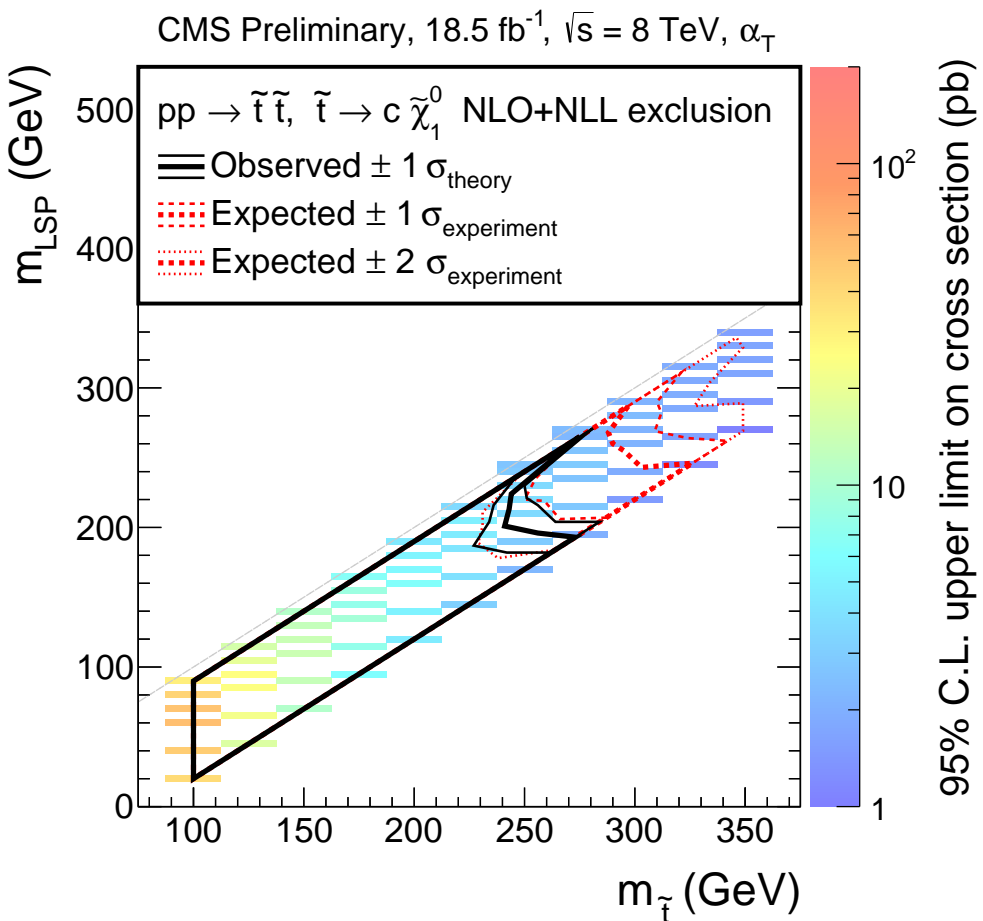


Fig. 9.4 The expected limit (red dashed line) with central band (thick red) and $\pm 1\sigma$ and $\pm 2\sigma$ uncertainty bands (thin red), and the observed limit (thick black) for the T2cc model. The limit is calculated with an include $H_T > 200$ GeV selection, and the analysis categories ($n_b = 0, 2 \leq n_{\text{jet}} \leq 3$), ($n_b = 1, 2 \leq n_{\text{jet}} \leq 3$), ($n_b = 0, n_{\text{jet}} \geq 4$), ($n_b = 1, n_{\text{jet}} \geq 4$)

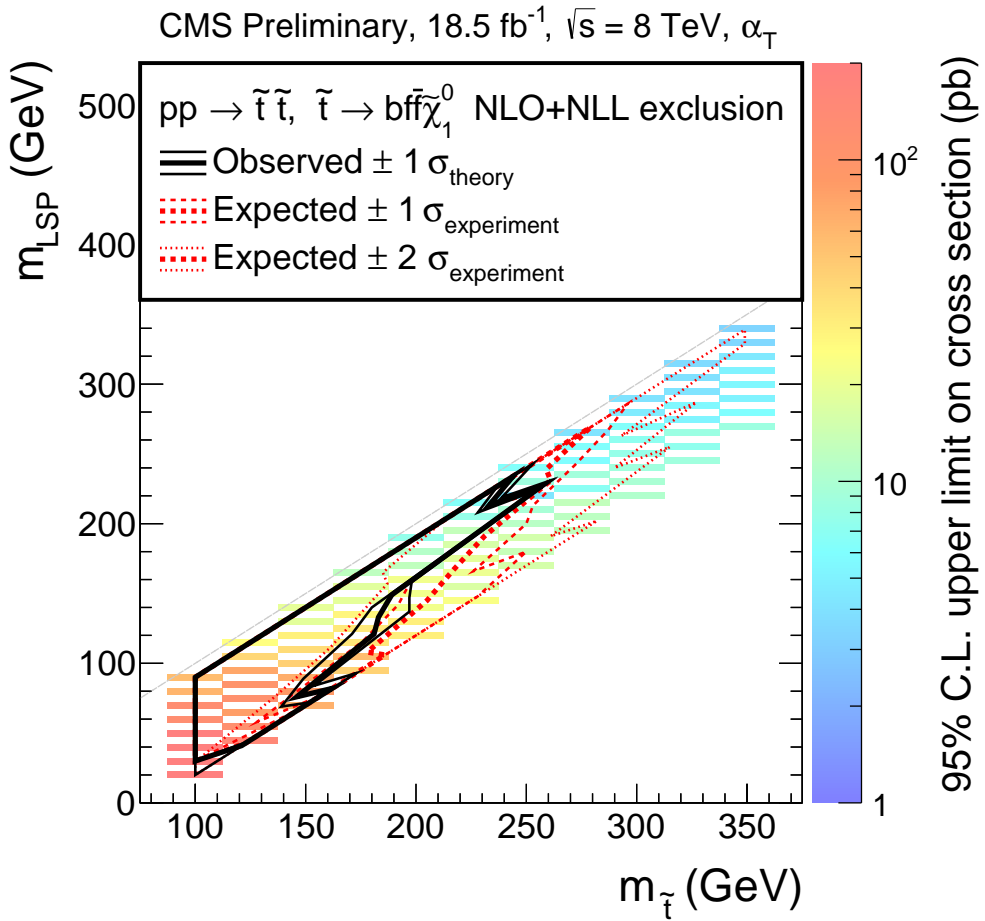


Fig. 9.5 The expected limit (red dashed line) with central band (thick red) and $\pm 1\sigma$ and $\pm 2\sigma$ uncertainty bands (thin red), and the observed limit (thick black) for the T2degen model. The limit is calculated with an include $H_T > 200$ GeV selection, and the analysis categories ($n_b = 0, 2 \leq n_{jet} \leq 3$), ($n_b = 1, 2 \leq n_{jet} \leq 3$), ($n_b = 0, n_{jet} \geq 4$), ($n_b = 1, n_{jet} \geq 4$)

9.4 Interpretation of excesses

best fit points in T2cc

1

Chapter 10

Conclusion

10.1 Conclusion

When I do actually write this, it's going to be really, really great.

A search for Supersymmetry in the jets and missing energy final state has been presented.

supersymmetry recap

how we searched for it

analysis - alphat, qcd reduction. correlates various variables, allowing for a sliding mht threshold...?

three dimensions

signal triggers populate the signal region

detailed study of any remaining residual QCD backgrounds

ewk predicted from sidebands. how this method works. adjoint control regions and transfer factors.

relevant systematics are determined from a statistically powerful suite of closure tests, each probing different facets of the analysis.

results are determined via a simultaneous fit using an extensive likelihood model no statistically significant excesses were observed - everything compatible with fluctuations

interpretations made in terms of two different decay channels of the stop particle, relevant at low mass splittings (mass degenerate scenarios)

strong, competitive limits produced

References

23

- [1] <https://twiki.cern.ch/twiki/bin/view/CMSPublic/PhysicsResultsSUS>. 1
- [2] <https://twiki.cern.ch/twiki/bin/view/AtlasPublic/SupersymmetryPublicResults>. 2
- [3] CMS Collaboration, “CMS Luminosity - Public Results,” 3
- [4] T. Sakuma and T. McCauley, “Detector and Event Visualization with SketchUp at the CMS Experiment,” *J.Phys.Conf.Ser.*, vol. 513, p. 022032, 2014. 4
5
- [5] D. Olivito, F. Wurthwein, *et al.*, “Hadronic recoil studies of heavy boosted systems, AN-2013/059,” 6
7
- [6] LEP Electroweak Working Group, “Precision Electroweak Measurements and Constraints on the Standard Model,” 2010. 8
9
- [7] S. L. Glashow, “Partial-symmetries of weak interactions,” *Nuclear Physics*, 10
11 vol. 22, no. 4, pp. 579 – 588, 1961.
- [8] S. Weinberg, “A Model of Leptons,” *Phys. Rev. Lett.*, vol. 19, pp. 1264–1266, Nov 1967. 12
13
- [9] A. Salam, “Weak and Electromagnetic Interactions,” *Conf.Proc.*, vol. C680519, 14
15 pp. 367–377, 1968.
- [10] H. D. Politzer, “Reliable perturbative results for strong interactions?,” *Phys. Rev. Lett.*, vol. 30, pp. 1346–1349, Jun 1973. 16
17
- [11] D. J. Gross and F. Wilczek, “Ultraviolet Behavior of Non-Abelian Gauge Theories,” *Phys. Rev. Lett.*, vol. 30, pp. 1343–1346, Jun 1973. 18
19
- [12] B. Martin and G. Shaw, *Particle Physics*. John Wiley and Sons, Ltd., third ed., 20
21 2009.
- [13] F. Englert and R. Brout, “Broken Symmetry and the Mass of Gauge Vector Mesons,” *Phys. Rev. Lett.*, vol. 13, pp. 321–323, Aug 1964. 22
23
- [14] P. W. Higgs, “Broken Symmetries and the Masses of Gauge Bosons,” *Phys. Rev. Lett.*, vol. 13, pp. 508–509, Oct 1964. 24
25
- [15] G. S. Guralnik, C. R. Hagen, and T. W. B. Kibble, “Global Conservation Laws and Massless Particles,” *Phys. Rev. Lett.*, vol. 13, pp. 585–587, Nov 1964. 26
27

- [16] Y. Fukuda *et al.*, “Evidence for oscillation of atmospheric neutrinos,” *Phys. Rev. Lett.*, vol. 81, pp. 1562–1567, Aug 1998. 28
- [17] Q. R. Ahmad *et al.*, “Measurement of day and night neutrino energy spectra at sno and constraints on neutrino mixing parameters,” *Phys. Rev. Lett.*, vol. 89, p. 011302, Jun 2002. 2
- [18] G. Altarelli and F. Feruglio, “Theoretical models of neutrino masses and mixings,” *Springer Tracts Mod.Phys.*, vol. 190, pp. 169–207, 2003. 5
- [19] S. Chatrchyan *et al.*, “Observation of a new boson at a mass of 125 GeV with the CMS experiment at the LHC,” *Phys.Lett.*, vol. B716, pp. 30–61, 2012. 7
- [20] G. Aad *et al.*, “Observation of a new particle in the search for the Standard Model Higgs boson with the ATLAS detector at the LHC,” *Phys.Lett.*, vol. B716, pp. 1–29, 2012. 9
- [21] E. Corbelli and P. Salucci, “The extended rotation curve and the dark matter halo of m33,” *Monthly Notices of the Royal Astronomical Society*, vol. 311, no. 2, pp. 441–447, 2000. 12
- [22] A. Leauthaud *et al.*, “New constraints on the evolution of the stellar-to-dark matter connection: A combined analysis of galaxy-galaxy lensing, clustering, and stellar mass functions from $z = 0.2$ to $z = 1$,” *The Astrophysical Journal*, vol. 744, no. 2, p. 159, 2012. 15
- [23] Y. A. Gol’fand and E. P. Likhtman, “Extension of the algebra of Poincaré group generators and violation of p invariance,” *JETP Lett.*, vol. 13, p. 323, 1971. 19
- [24] J. Wess and B. Zumino, “Supergauge transformations in four dimensions,” *Nucl. Phys. B*, vol. 70, p. 39, 1974. 21
- [25] H. P. Nilles, “Supersymmetry, supergravity and particle physics,” *Phys. Reports*, vol. 110, p. 1, 1984. 23
- [26] H. Haber and G. Kane, “The search for supersymmetry: Probing physics beyond the standard model,” *Phys. Reports*, vol. 117, p. 75, 1987. 25
- [27] R. Barbieri, S. Ferrara, and C. A. Savoy, “Gauge models with spontaneously broken local supersymmetry,” *Phys. Lett. B*, vol. 119, p. 343, 1982. 27
- [28] S. Dawson, E. Eichten, and C. Quigg, “Search for supersymmetric particles in hadron - hadron collisions,” *Phys. Rev. D*, vol. 31, p. 1581, 1985. 29
- [29] S. P. Martin, “A Supersymmetry primer,” *Adv.Ser.Direct.High Energy Phys.*, vol. 21, pp. 1–153, 2010. 31
- [30] S. Dimopoulos and D. W. Sutter, “The Supersymmetric flavor problem,” *Nucl.Phys.*, vol. B452, pp. 496–512, 1995. 33
- [31] E. Witten, “Dynamical breaking of supersymmetry,” *Nucl. Phys. B*, vol. 188, p. 513, 1981. 35

-
- ³⁷ [32] S. Dimopoulos and H. Georgi, “Softly broken supersymmetry and SU(5),” *Nucl. Phys. B*, vol. 193, p. 150, 1981. 1
- [33] G. R. Farrar and P. Fayet, “Phenomenology of the production, decay, and detection of new hadronic states associated with supersymmetry,” *Physics Letters B*, vol. 76, no. 5, pp. 575 – 579, 1978. 2
3
4
- [34] G. Jungman, M. Kamionkowski, and K. Griest, “Supersymmetric dark matter,” *Phys.Rept.*, vol. 267, pp. 195–373, 1996. 5
6
- [35] R. Barbieri and D. Pappadopulo, “S-particles at their naturalness limits,” *JHEP*, vol. 10, p. 061, 2009. 7
8
- [36] M. Carena, G. Nardini, M. Quiros, and C. E. Wagner, “The Effective Theory of the Light Stop Scenario,” *JHEP*, vol. 0810, p. 062, 2008. 9
10
- [37] G. L. Kane, C. F. Kolda, L. Roszkowski, and J. D. Wells, “Study of constrained minimal supersymmetry,” *Phys.Rev.*, vol. D49, pp. 6173–6210, 1994. 11
12
- [38] J. Alwall, P. C. Schuster, and N. Toro, “Simplified models for a first characterization of new physics at the lhc,” *Phys. Rev. D*, vol. 79, p. 075020, Apr 2009. 13
14
- [39] D. Alves, N. Arkani-Hamed, S. Arora, *et al.*, “Simplified Models for LHC New Physics Searches,” *J.Phys.*, vol. G39, p. 105005, 2012. 15
16
- [40] C. Collaboration, “Interpretation of searches for supersymmetry with simplified models,” *Phys. Rev. D*, vol. 88, p. 052017, Sep 2013. 17
18
- [41] C. Boehm, A. Djouadi, and Y. Mambrini, “Decays of the lightest top squark,” *Phys.Rev.*, vol. D61, p. 095006, 2000. 19
20
- [42] D. Spergel *et al.*, “First year Wilkinson Microwave Anisotropy Probe (WMAP) observations: Determination of cosmological parameters,” *Astrophys.J.Suppl.*, vol. 148, pp. 175–194, 2003. 21
22
23
- [43] C. Balazs, M. Carena, and C. Wagner, “Dark matter, light stops and electroweak baryogenesis,” *Phys.Rev.*, vol. D70, p. 015007, 2004. 24
25
- [44] S. P. Martin, “Compressed supersymmetry and natural neutralino dark matter from top squark-mediated annihilation to top quarks,” *Phys.Rev.*, vol. D75, p. 115005, 2007. 26
27
28
- [45] L. Evans and P. Bryant, “LHC Machine,” *JINST*, vol. 3, p. S08001, 2008. 29
- [46] S. Chatrchyan *et al.*, “The CMS experiment at the CERN LHC,” *JINST*, vol. 3, p. S08004, 2008. 30
31
- [47] G. L. Bayatyan *et al.*, *CMS TriDAS project: Technical Design Report, Volume 1: The Trigger Systems*. Technical Design Report CMS, 2002. 32
33

- [48] C. Eck, J. Knobloch, L. Robertson, I. Bird, K. Bos, N. Brook, D. Düllmann, I. Fisk, D. Foster, B. Gibbard, C. Grandi, F. Grey, J. Harvey, A. Heiss, F. Hemmer, S. Jarp, R. Jones, D. Kelsey, M. Lamanna, H. Marten, P. Mato-Vila, F. Ould-Saada, B. Panzer-Steindel, L. Perini, Y. Schutz, U. Schwickerath, J. Shiers, and T. Wenaus, *LHC computing Grid: Technical Design Report. Version 1.06 (20 Jun 2005)*. Technical Design Report LCG, Geneva: CERN, 2005. 34
- [49] M. Cacciari, G. P. Salam, and G. Soyez, “The anti- k_t jet clustering algorithm,” *JHEP*, vol. 04, p. 063, 2008. 6
- [50] M. Cacciari and G. P. Salam, “Pileup subtraction using jet areas,” *Physics Letters B*, vol. 659, pp. 119 – 126, 2008. 8
- [51] M. Cacciari, G. P. Salam, and G. Soyez, “The catchment area of jets,” *Journal of High Energy Physics*, vol. 2008, no. 04, p. 005, 2008. 10
- [52] S. Chatrchyan *et al.*, “Determination of Jet Energy Calibration and Transverse Momentum Resolution in CMS,” *JINST*, vol. 6, p. P11002, 2011. 12
- [53] CMS Collaboration, “Jet ID.” <https://twiki.cern.ch/twiki/bin/viewauth/CMS/JetID>. 14
- [54] CMS Collaboration, “Jet Energy Scale.” <https://twiki.cern.ch/twiki/bin/view/CMS/JetEnergyScale>. 16
- [55] CMS Collaboration, “Determination of jet energy calibration and transverse momentum resolution in CMS,” *Journal of Instrumentation*, vol. 6, p. 11002, Nov. 2011. 18
- [56] S. Chatrchyan *et al.*, “Identification of b-quark jets with the cms experiment,” *JINST*, vol. 8, p. P04013, 2013. 21
- [57] CMS Collaboration, “Baseline Muon ID.” <https://twiki.cern.ch/twiki/bin/view/CMSPublic/SWGuideMuonId>. 23
- [58] CMS Collaboration, “Photon ID.” <https://twiki.cern.ch/twiki/bin/view/CMS/PhotonIDAnalysis>. 25
- [59] CMS Collaboration, “Electron ID.” <https://twiki.cern.ch/twiki/bin/view/CMSPublic/SWGuideCutBasedElectronID>. 27
- [60] http://cms.cern.ch/iCMS/jsp/db_notes/noteInfo.jsp?cmsnoteid=CMSAN-2013/089. Search for Direct Top Squark Pair Production in the Single Lepton Channel with Transverse Mass at 8 TeV, CMS AN-2013/089. 29
- [61] L. Randall and D. Tucker-Smith, “Dijet Searches for Supersymmetry at the LHC,” *Phys. Rev. Lett.*, vol. 101, p. 221803, 2008. 32
- [62] CMS Collaboration, “SUSY searches with dijet events,” 2008. 34
- [63] CMS Collaboration, “Search strategy for exclusive multi-jet events from supersymmetry at CMS,” Tech. Rep. CMS-PAS-SUS-09-001, CERN, 2009. Geneva, Jul 2009. 35

-
- ³⁸ [64] R. Cousins, “Probability Density Functions for Positive Nuisance Parameters.” http://www.physics.ucla.edu/~cousins/stats/cousins_lognormal_prior.pdf. ¹
- [65] W. Verkerke and D. Kirkby, “RooFit.” <http://root.cern.ch/drupal/content/roofit>. ²
- [66] F. James and M. Roos, “Minuit: A System for Function Minimization and Analysis of the Parameter Errors and Correlations,” *Comput.Phys.Commun.*, vol. 10, pp. 343–367, 1975. ³
 ⁴
 ⁵
- [67] <https://twiki.cern.ch/twiki/bin/viewauth/CMS/BtagPOG>. ⁶
- [68] M. Botje, J. Butterworth, A. Cooper-Sarkar, *et al.*, “The pdf4lhc working group interim recommendations.” 2011. ⁷
 ⁸
- [69] CMS Collaboration, “CMS Luminosity Based on Pixel Cluster Counting - Summer 2013 Update,” 2013. ⁹
 ¹⁰
- [70] A. L. Read, “Presentation of search results: the cl s technique,” *Journal of Physics G: Nuclear and Particle Physics*, vol. 28, no. 10, p. 2693, 2002. ¹¹
 ¹²

Appendix A

13

Signal Model Systematics Plots

1

T2cc

2

Jet Energy Scale

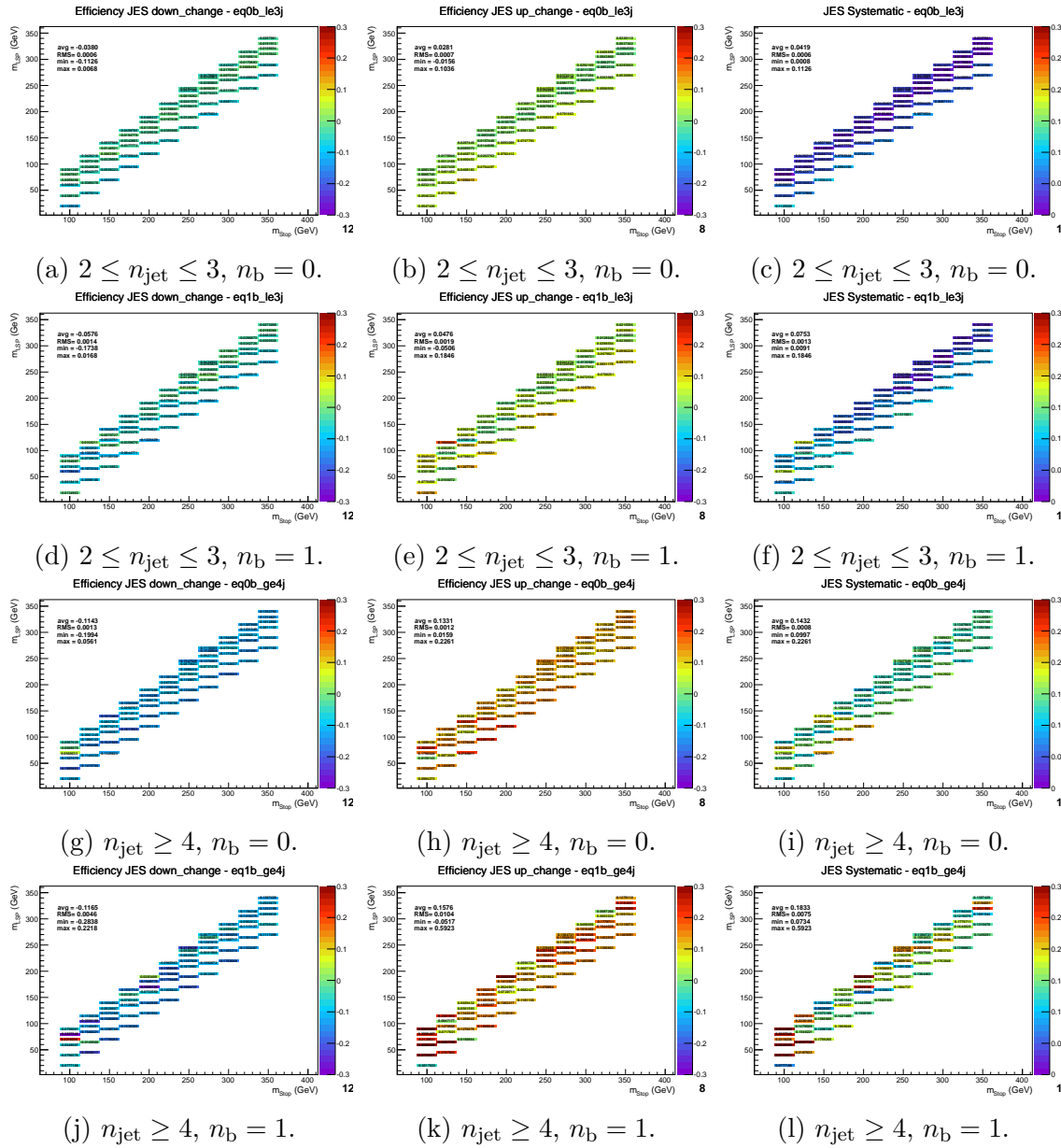


Fig. A.1 The relative change in acceptance times signal efficiency for the T2cc model for downwards (left) and upwards (middle) fluctuations of all jet energies by the uncertainty of the jet energy scale, and the derived systematic values (right). Each set of plots corresponds to one of the four most sensitive analysis categories (n_b, n_{jet}), with the inclusive requirement $H_T > 200$ GeV.

1 PDF

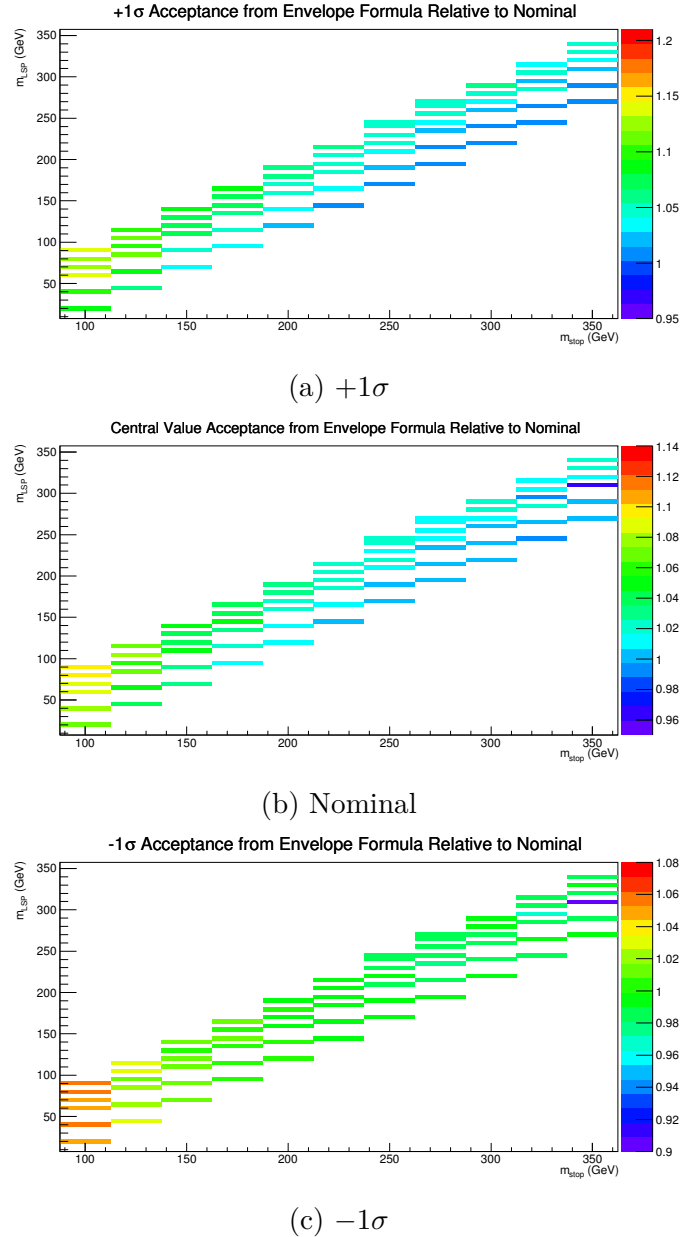


Fig. A.2 PDF uncertainties as a function of the T2cc scan plane, calculated using a PDF4LHC ‘envelope’ calculation to determine a central band (A.2b), and $\pm 1\sigma$ variations (A.2a and A.2c). Plots are for a fully inclusive selection on H_T , n_{jet} and n_b .

Initial State Radiation

1

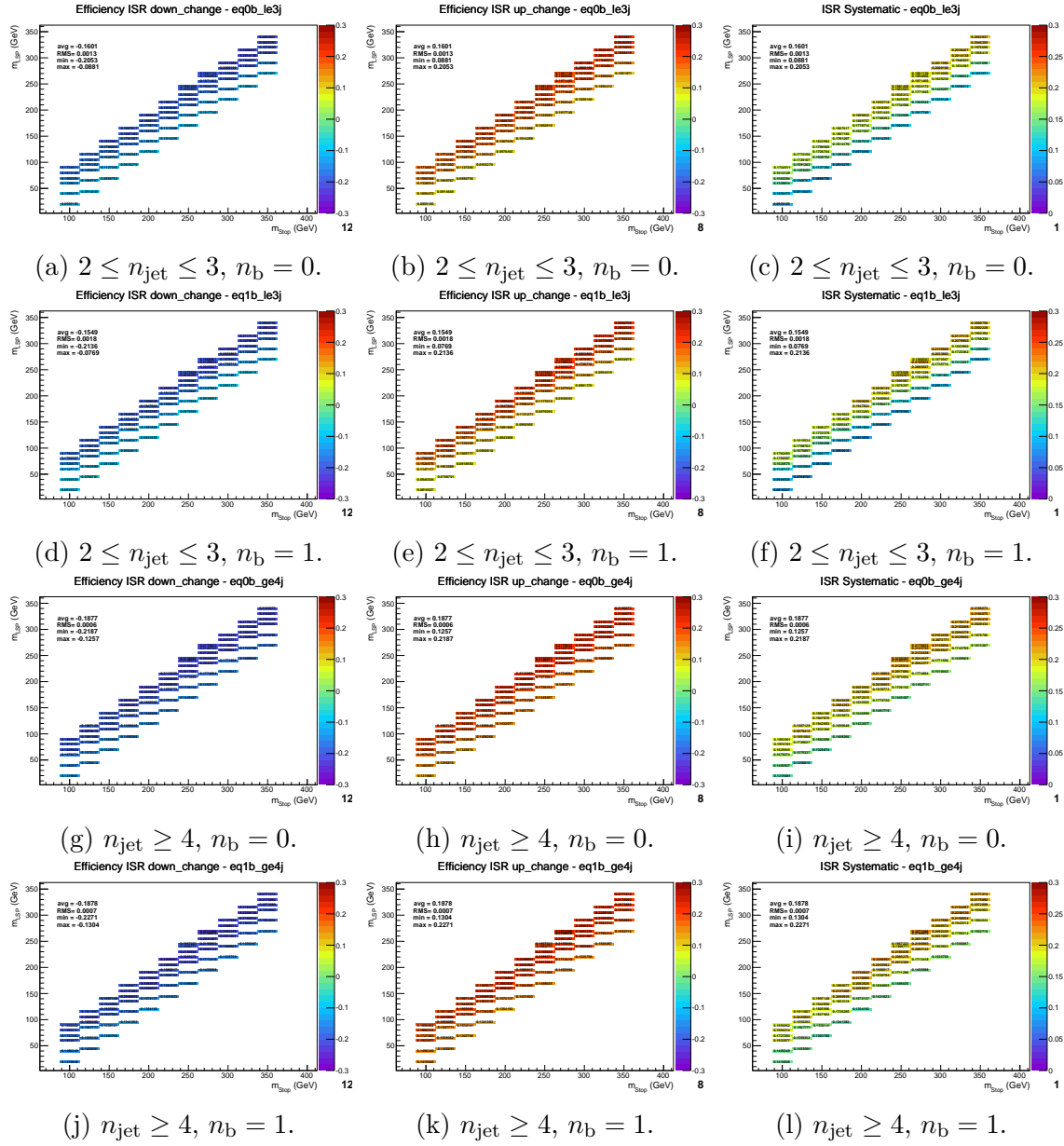


Fig. A.3 The relative change in acceptance times signal efficiency for the T2cc model for downwards (left) and upwards (middle) fluctuations of the global event weight equal to the magnitude of the ISR corrections, and the derived systematic values (right). Each set of plots corresponds to one of the four most sensitive analysis categories (n_b, n_{jet}), with the inclusive requirement $H_T > 200$ GeV.

1 B-tag Scale Factor

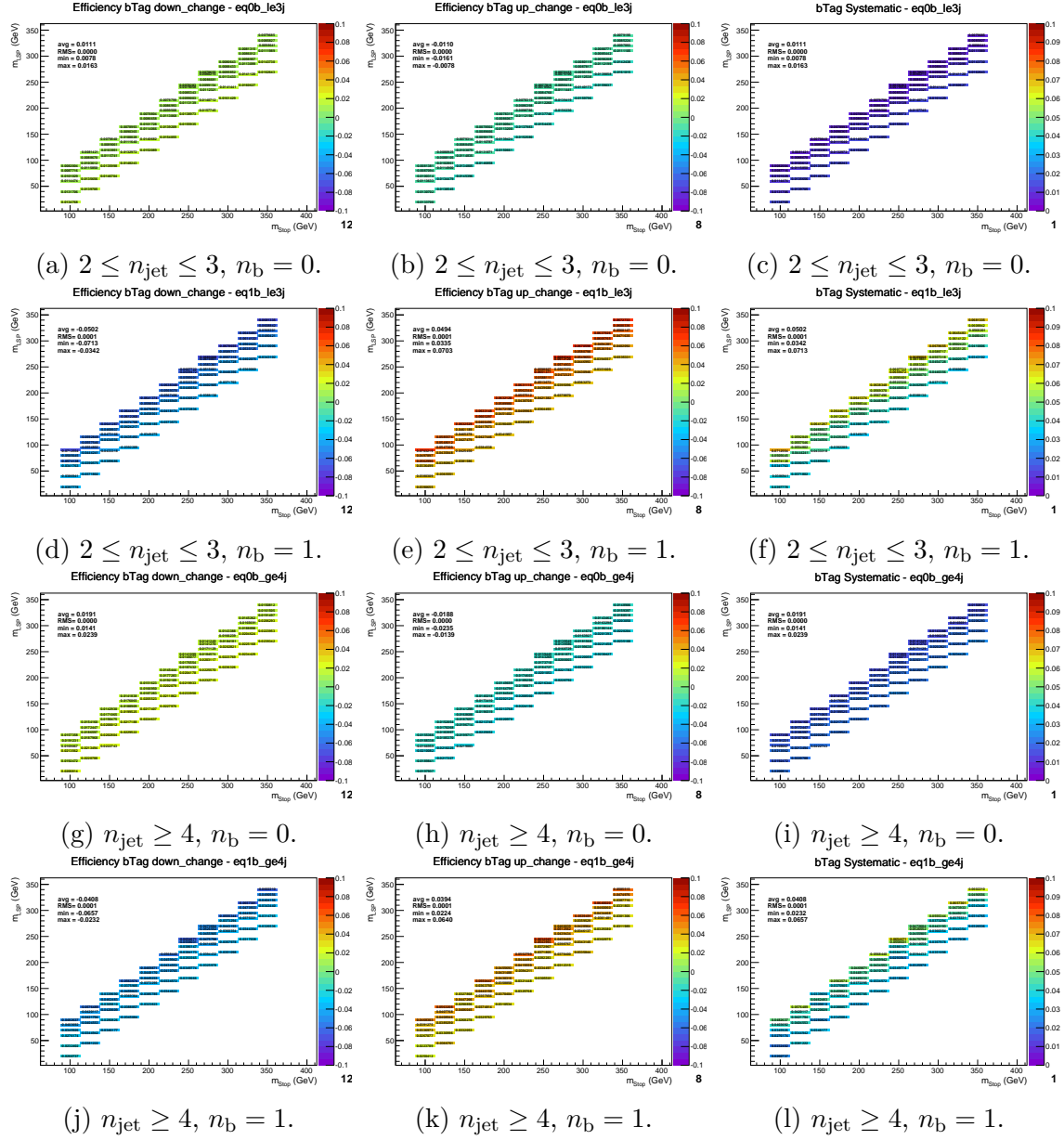


Fig. A.4 The relative change in acceptance times signal efficiency for the T2cc model for downwards (left) and upwards (middle) fluctuations of global event weight according to the uncertainties of the Btag scale factors, and the derived systematic values (right). Each set of plots corresponds to one of the four most sensitive analysis categories (n_b , n_{jet}), with the inclusive requirement $H_T > 200$ GeV.

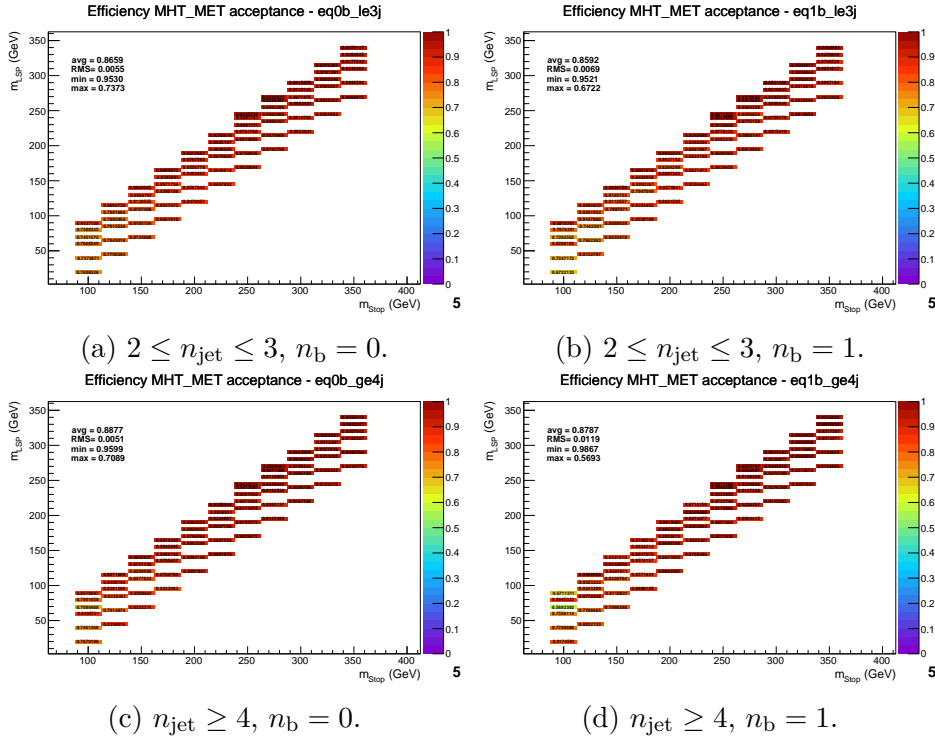
$\cancel{H}_T/\cancel{E}_T$ cut

Fig. A.5 The acceptance of the $\cancel{H}_T/\cancel{E}_T$ cut as a function of the T2cc mass plane. Each plot represents one of the four most sensitive analysis categories (n_b, n_{jet}), with the inclusive requirement $H_T > 200$ GeV.

1 Dead ECAL cut

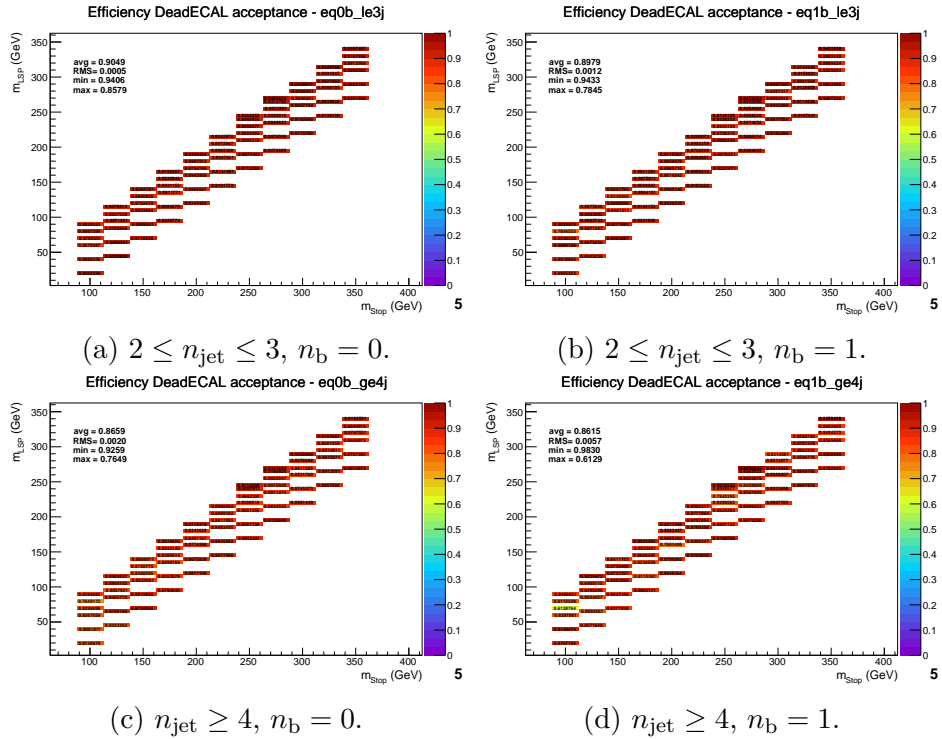


Fig. A.6 The acceptance of the DeadECAL cut as a function of the T2cc mass plane. Each plot represents one of the four most sensitive analysis categories (n_b, n_{jet}), with the inclusive requirement $H_T > 200$ GeV.

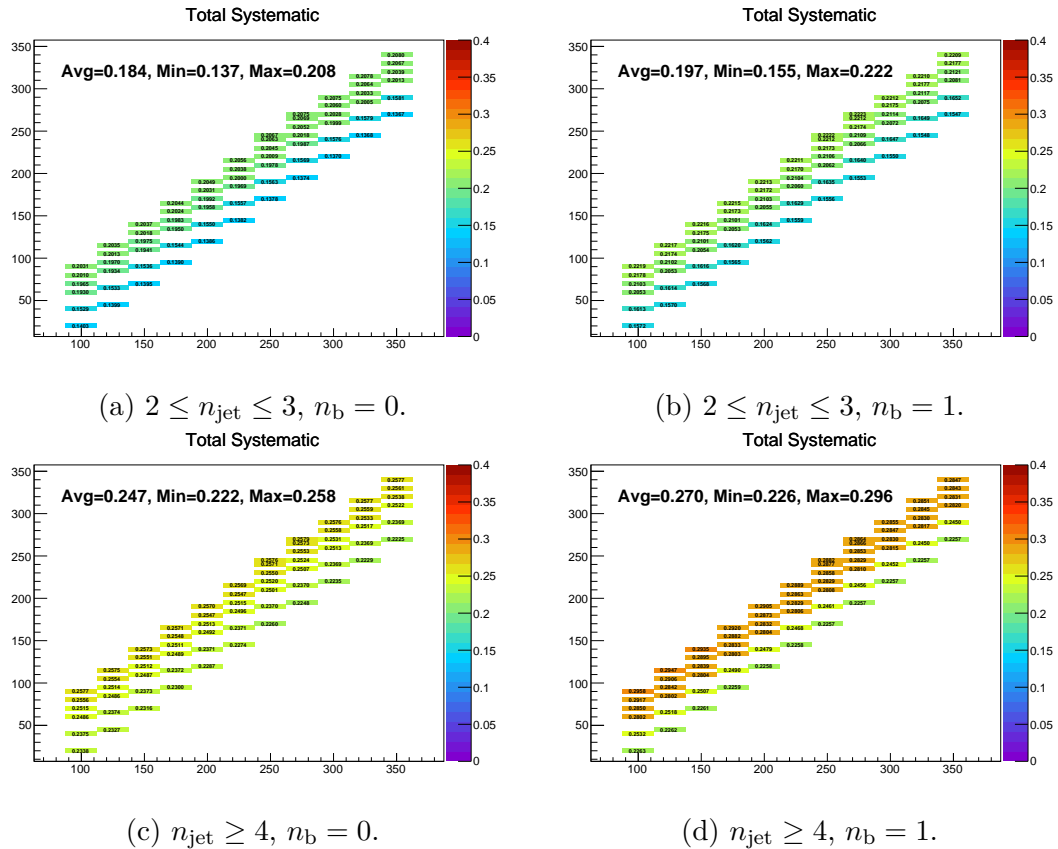


Fig. A.7 The total systematic uncertainty as a function of the T2cc scan plane, where all individual systematic contributions are summed in quadrature. Each plot represents one of the four most sensitive analysis categories (n_b, n_{jet}), with the inclusive requirement $H_T > 200$ GeV.

T2degen

1

Jet Energy Scale

1

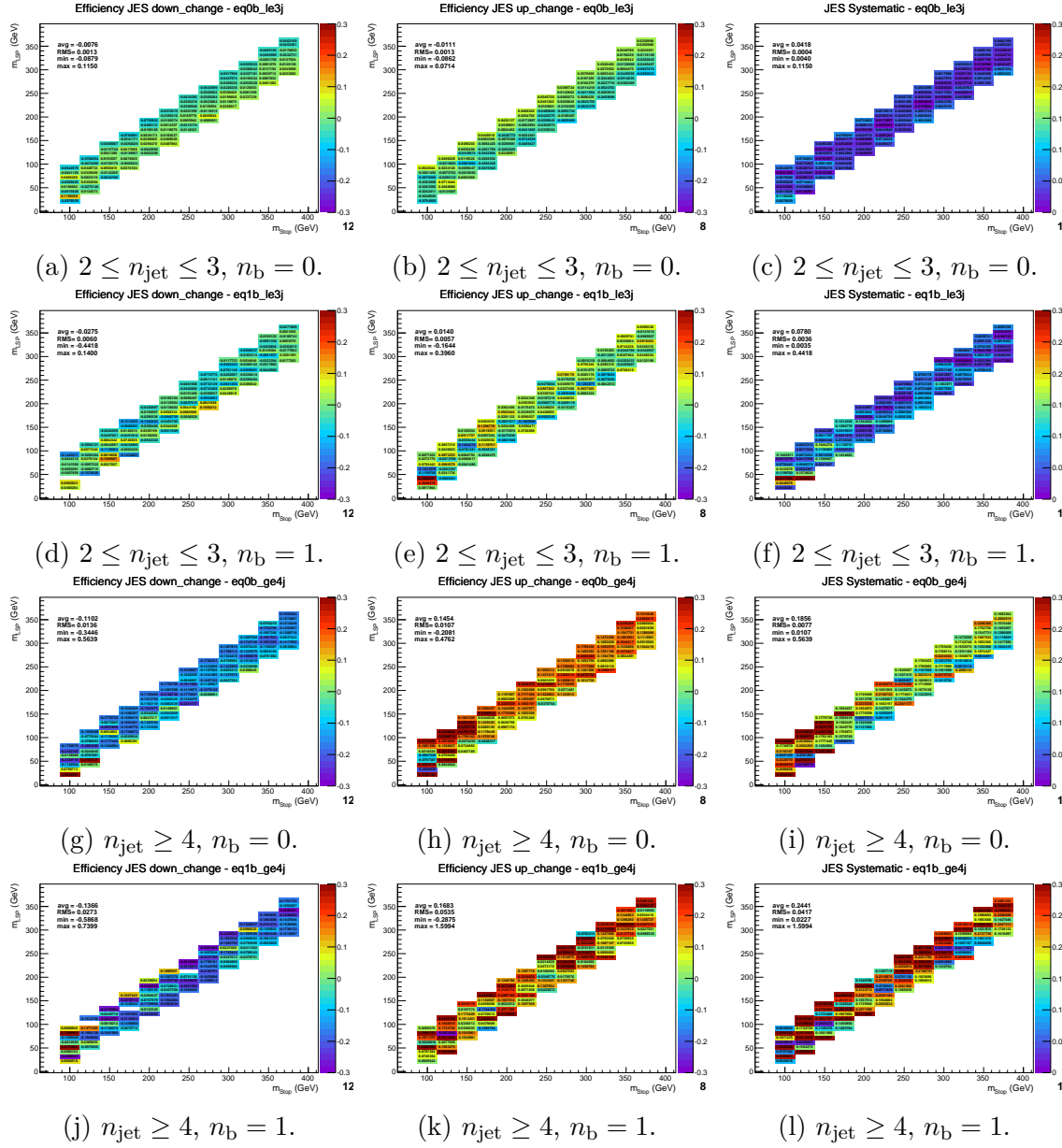


Fig. A.8 The relative change in acceptance times signal efficiency for the T2Degen model for downwards (left) and upwards (middle) fluctuations of all jet energies by the uncertainty of the jet energy scale, and the derived systematic values (right). Each set of plots corresponds to one of the four most sensitive analysis categories (n_b, n_{jet}), with the inclusive requirement $H_T > 200$ GeV.

1 Initial State Radiation

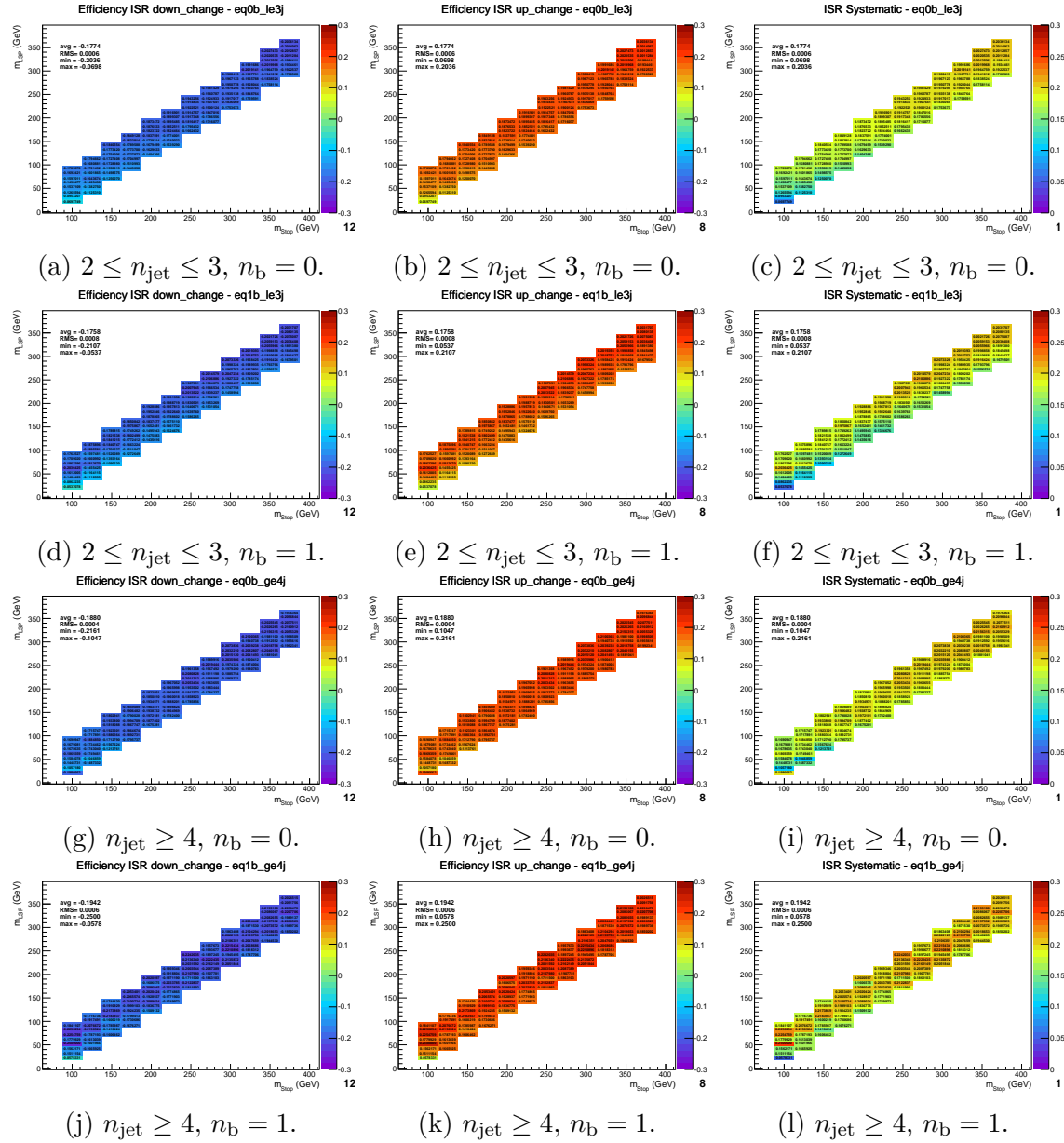


Fig. A.9 The relative change in acceptance times signal efficiency for the T2Degen model for downwards (left) and upwards (middle) fluctuations of the global event weight equal to the magnitude of the ISR corrections, and the derived systematic values (right). Each set of plots corresponds to one of the four most sensitive analysis categories (n_b, n_{jet}), with the inclusive requirement $H_T > 200 \text{ GeV}$.

B-tag Scale Factor

1

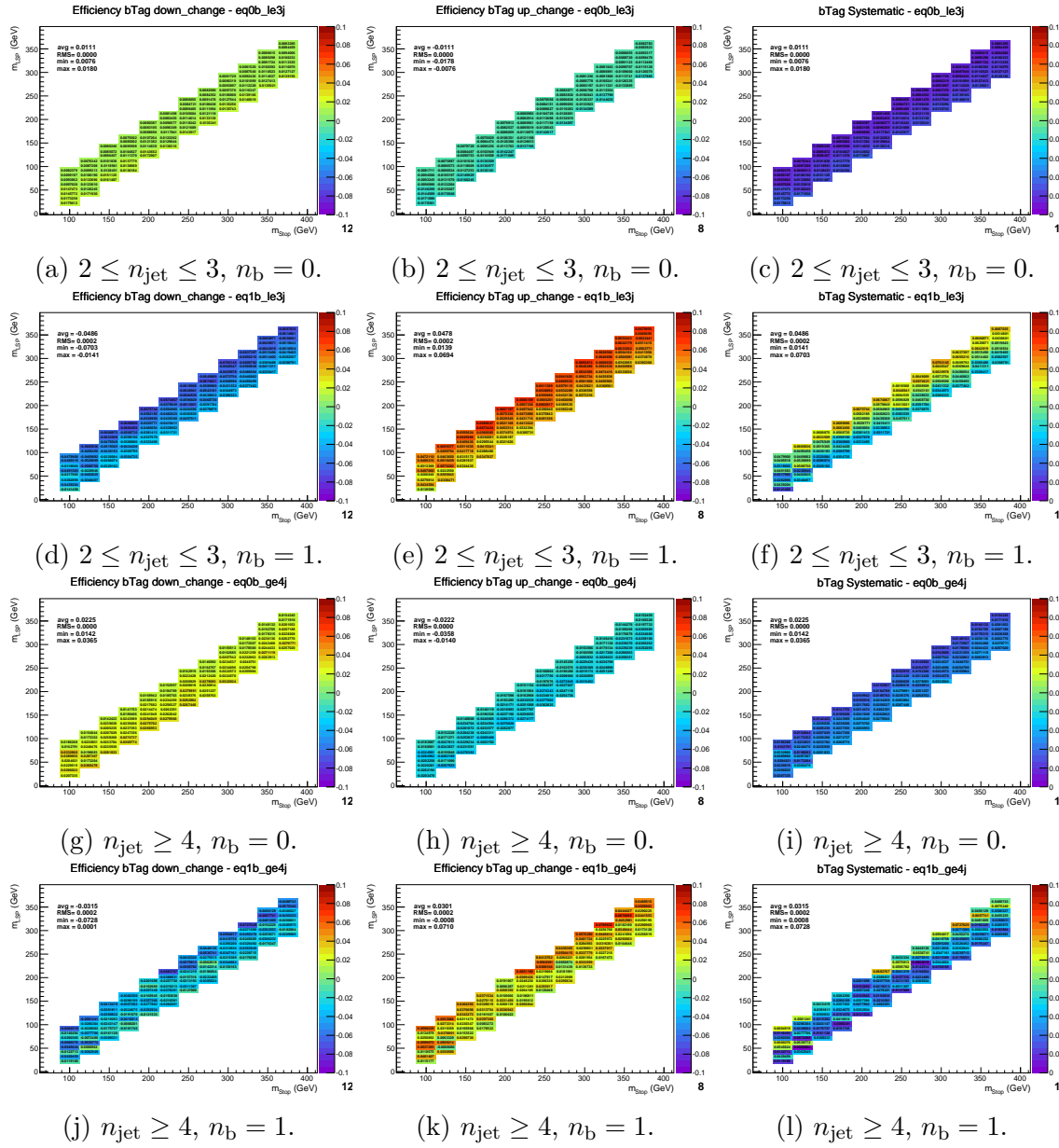


Fig. A.10 The relative change in acceptance times signal efficiency for the T2Degen model for downwards (left) and upwards (middle) fluctuations of global event weight according to the uncertainties of the Btag scale factors, and the derived systematic values (right). Each set of plots corresponds to one of the four most sensitive analysis categories (n_b, n_{jet}), with the inclusive requirement $H_T > 200$ GeV.

₁ H_T/\cancel{E}_T cut

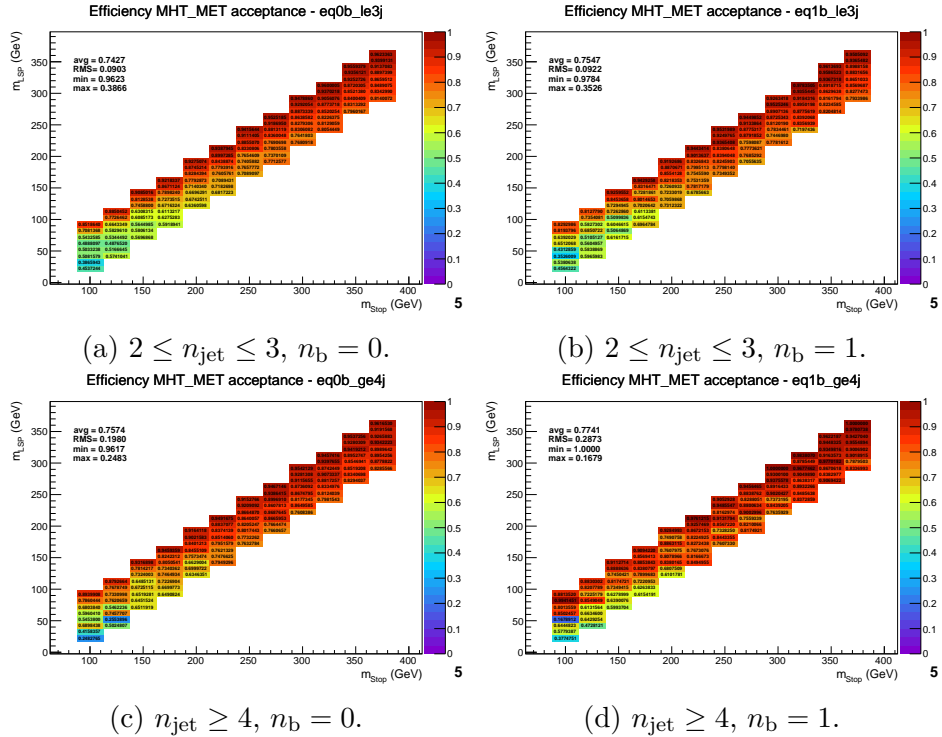


Fig. A.11 The acceptance of the H_T/\cancel{E}_T cut as a function of the T2degen mass plane. Each plot represents one of the four most sensitive analysis categories (n_b, n_{jet}), with the inclusive requirement $H_T > 200$ GeV.

Dead ECAL cut

1

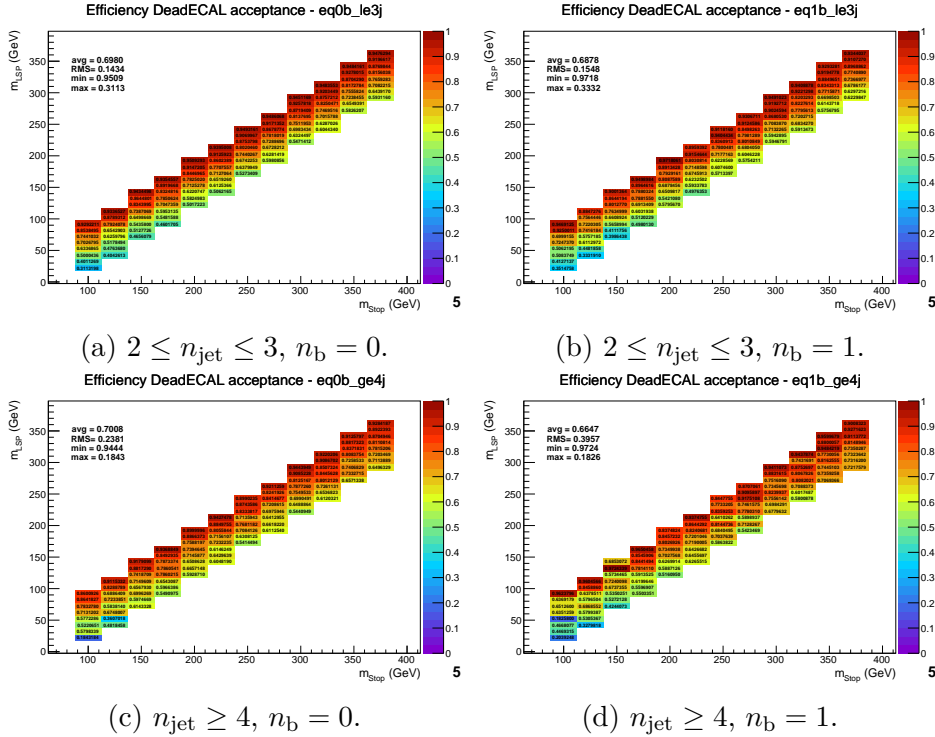


Fig. A.12 The acceptance of the DeadECAL cut as a function of the T2Degen mass plane. Each plot represents one of the four most sensitive analysis categories (n_b, n_{jet}), with the inclusive requirement $H_T > 200$ GeV.

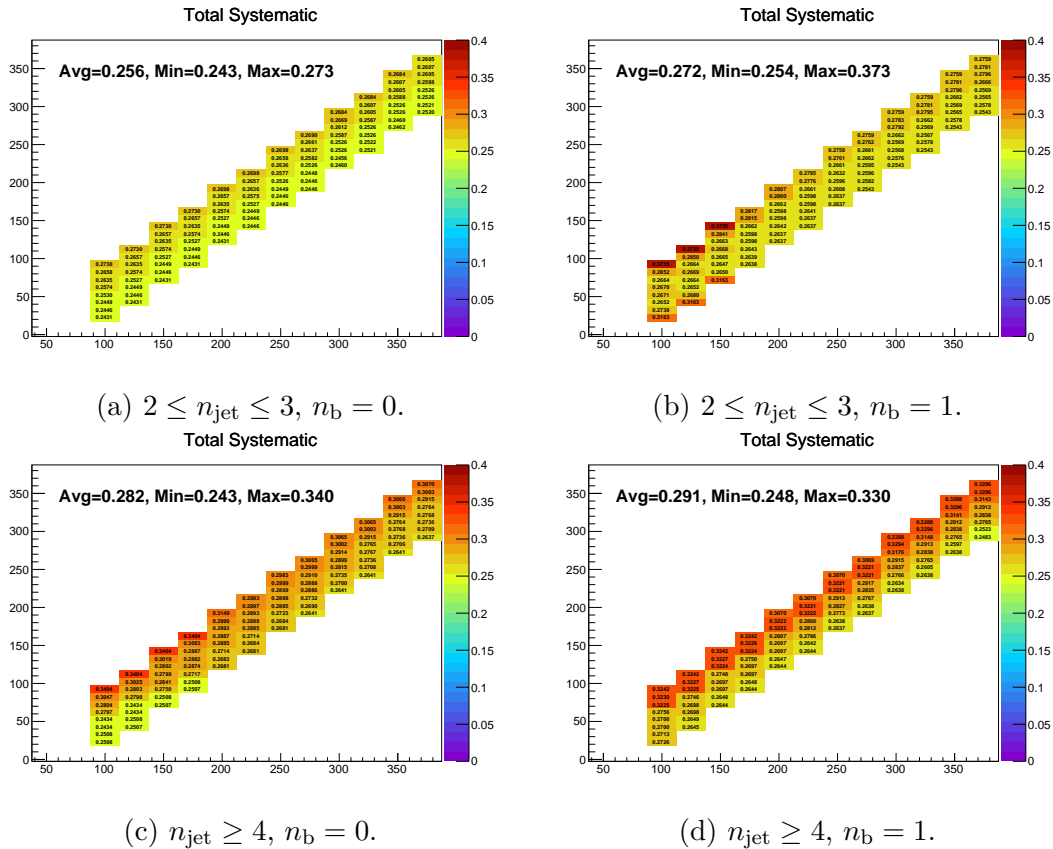


Fig. A.13 The total systematic uncertainty as a function of the T2Degen scan plane, where all individual systematic contributions are summed in quadrature. Each plot represents one of the four most sensitive analysis categories (n_b, n_{jet}), with the inclusive requirement $H_T > 200$ GeV.

¹ Appendix B

$\Delta\phi_{min}^*$ requirement in the signal region

As described in chapter 6, an event level requirement is made in the signal region such that all events have $\Delta\phi_{min}^* > 0.3$, in order to remove any remaining QCD MJ contamination.

B.1 Simulation

An event display of a typical event is shown in figure B.3. It is important to note the high amount, 185 GeV, of generator level \cancel{E}_T ('genmetP4True', thin pink arrow) pointing along the axis of a reconstructed jet with $p_T = 119 GeV$ (bold blue arrow) - a configuration which, coupled with multiple additional jets, can conspire to give large values of α_T . The sum of the generator level \cancel{E}_T and the p_T of the jet sum to the p_T of the generator level jet (bold black arrow), indicating that the missing energy of the event comes almost entirely from the neutrinos from the decay of the jet. Furthermore, this implies the ratio $\cancel{H}_T/\cancel{E}_T$ to be near unity, therefore allowing events to also evade the $\cancel{H}_T/\cancel{E}_T < 1.25$ requirement of the signal region.

B.2 Effect on signal models

The effect of the $\Delta\phi_{min}^* > 0.3$ requirement on the T2cc and T2degen signal models is shown in figures B.1 and B.2 respectively.

Model acceptance change due to the requirement appears to be intrinsically linked

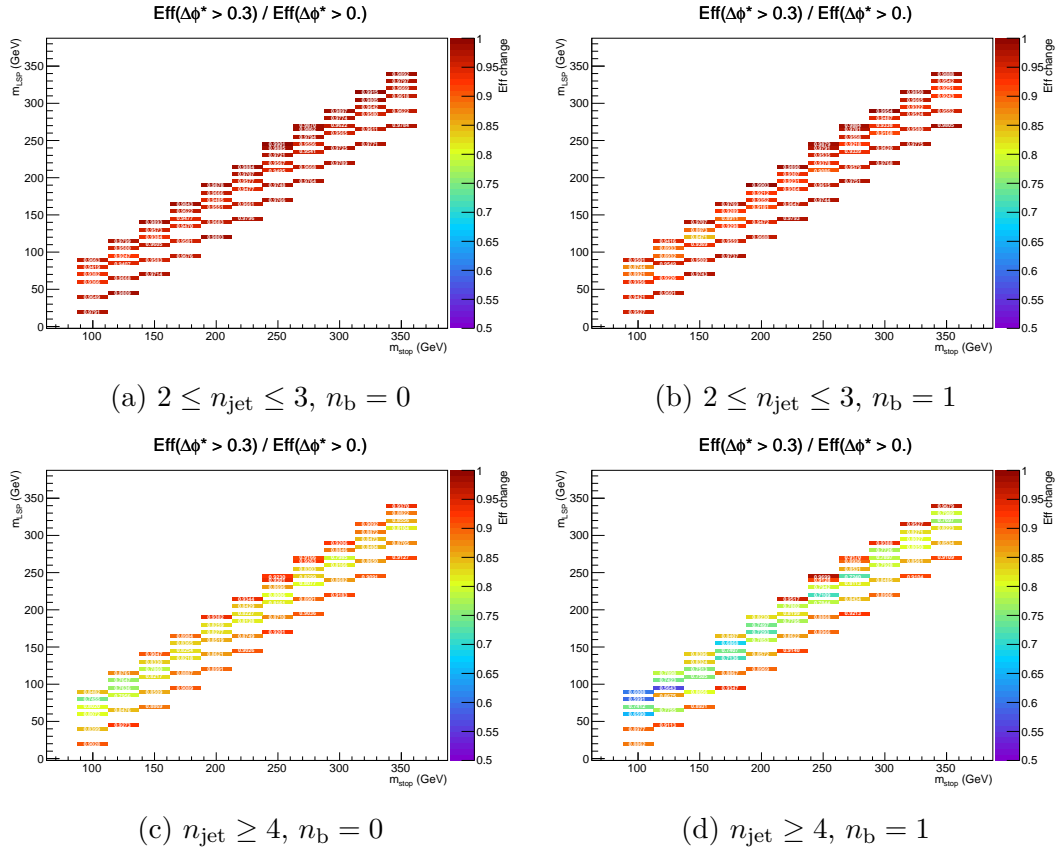


Fig. B.1 The change in acceptance of the T2cc model when applying the $\Delta\phi_{min}^* > 0.3$ requirement. Plots are shown for the four relevant categories used for interpretation, with an inclusive selection of $H_T > 200$ GeV

to the mutliplicity of objects, in this case jets, in the event. The $n_{jet} \geq 4$ categories appear to reduce acceptance the most. A similar trend is seen when going from $n_b = 0$ to $n_b = 1$, most noticeably in T2degen, where the b-tagged jet will predominantly come from the real b-quark in the decay. The configuration of a boosted SUSY decay system containing both jets and invisible $\tilde{\chi}^0$ particles could have appear like the heavy flavour QCD events this cut is targetted at removing.

Additionally an increased number of jets in the event, as seen in the higher n_{jet} category, increases the probability of a jet mis-measurement which could lead to low values of $\Delta\phi_{min}^*$, thus causing an event to be removed.

20

B.2 Effect on signal models

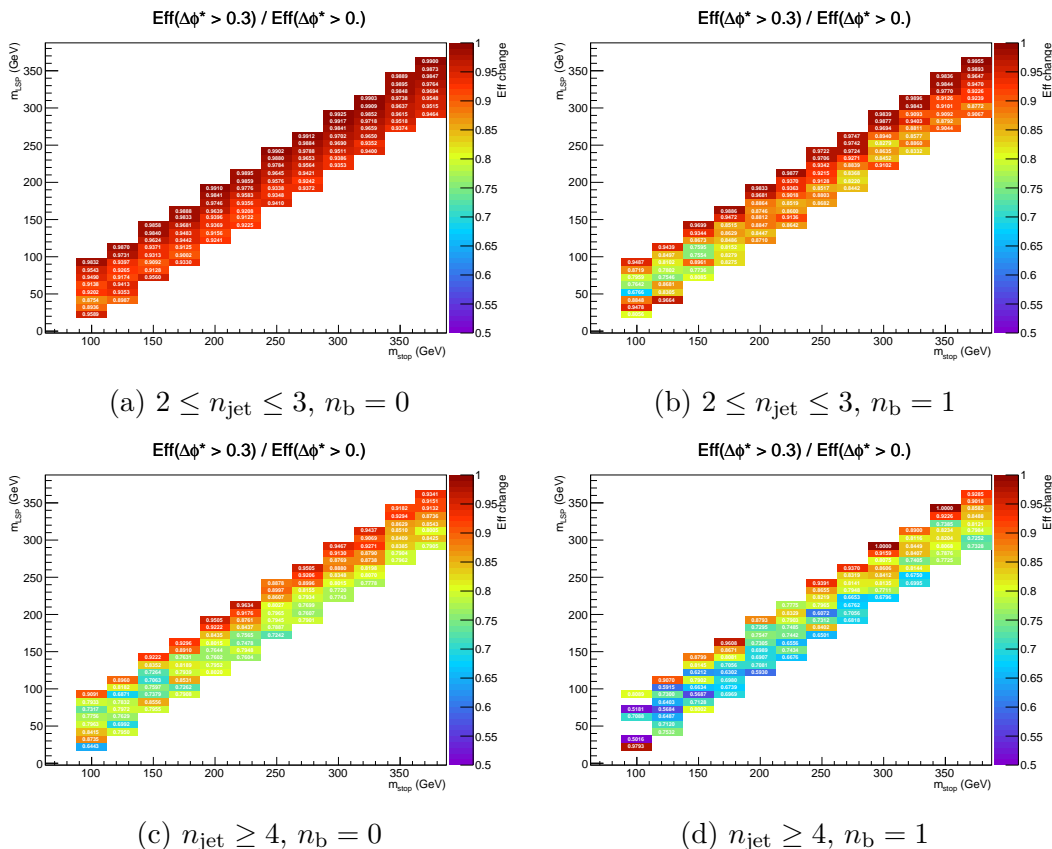


Fig. B.2 The change in acceptance of the T2degen model when applying the $\Delta\phi_{min}^* > 0.3$ requirement. Plots are shown for the four relevant categories used for interpretation, with an inclusive selection of $H_T > 200$ GeV

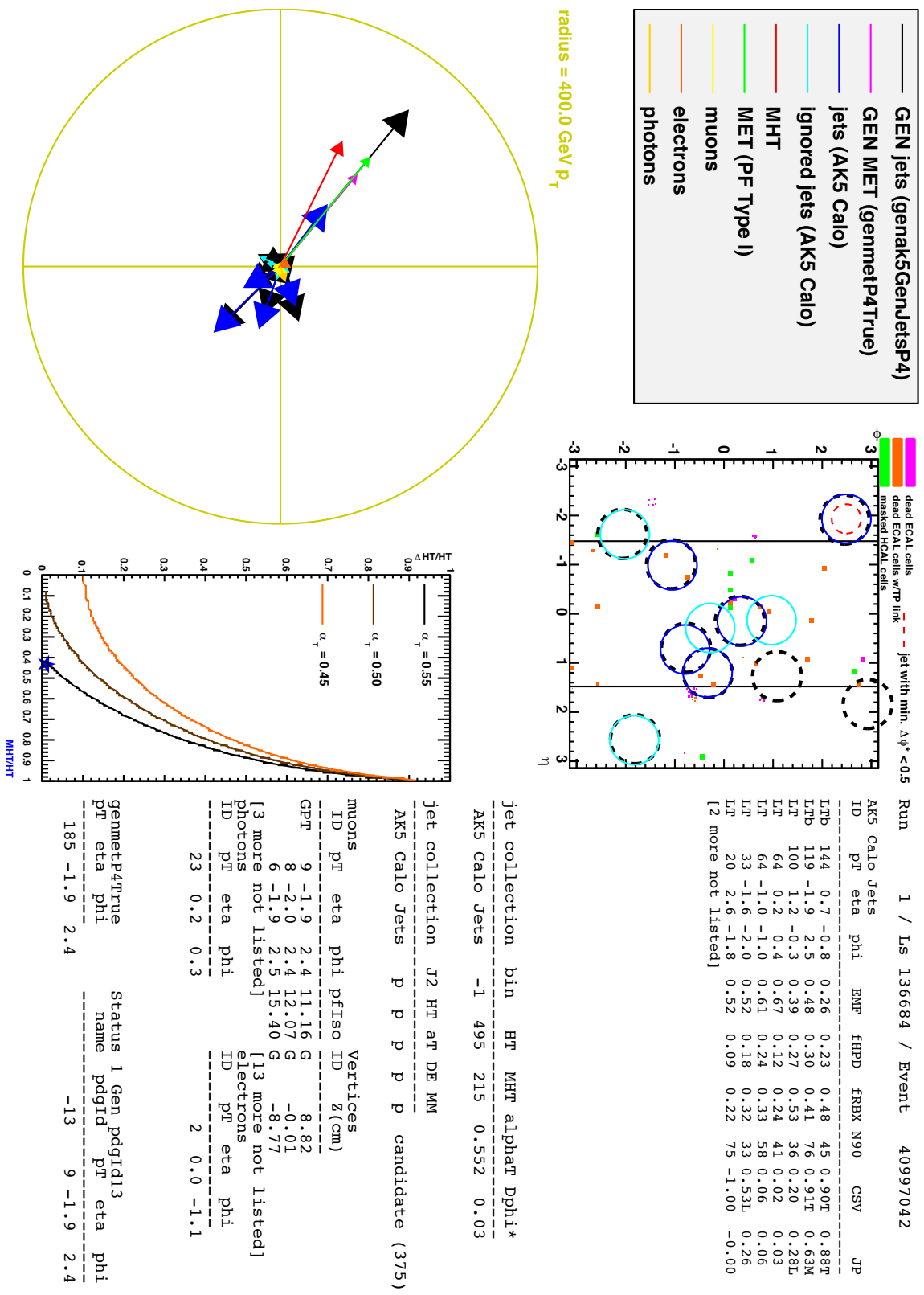


Fig. B.3 An event display of a typical heavy flavour QCD event, with a jet decaying leptonically with high- p_T neutrinos and therefore considerable generator-level \cancel{E}_T .